CRANFIELD UNIVERSITY

KONSTANTINOS VASILOPOULOS

ACCIDENTS CAUSED BY HAZARDOUS MATERIALS RELEASED IN AN URBAN ENVIRONMENT:A NUMERICAL AND EXPERIMENTAL APPROACH

SCHOOL OF AEROSPACE, TRANSPORT AND MANUFACTURING

PhD
Academic Year: 2019

Supervisor: Dr P. Tsoutsanis
April 2019

CRANFIELD UNIVERSITY

SCHOOL OF AEROSPACE, TRANSPORT AND MANUFACTURING

PhD

Academic Year 2019

KONSTANTINOS VASILOPOULOS

ACCIDENTS CAUSED BY HAZARDOUS MATERIALS RELEASED IN AN URBAN ENVIRONMENT:A NUMERICAL AND EXPERIMENTAL APPROACH

Supervisor: Dr P. Tsoutsanis
April 2019

This thesis is submitted in partial fulfilment of the requirements for the degree of PhD

ABSTRACT

This research studies the transport and dispersion of hazardous materials after a fire accident in an urban setting and the unpredictable threats provoked for the population and the environment. A fire accident may result, inter alia, from industrial activity or during the transportation of hazardous materials, such as diesel, petrol or kerosene liquids. In the current research, mineral oil pool fire accidents are examined in order to define the toxic smoke zones at different urban scale geometries. Three different urban scale geometries are examined: a) an isolated building, b) a street canyon and c) a staggered array of urban blocks. The fluid flow, the hazardous dispersion and the safety limits are studied using the Computational Fluid Dynamics (CFD) techniques and wind tunnel experiments.

The Computational simulations were conducted using the CFD solver of Fluent and the Fire Dynamic Simulator (FDS). Both Reynolds-average Navier-Stokes (RANS) modes and Large Eddy Simulations (LES) methods were applied. Wind tunnel experiments were conducted in order to better understand the flow around these geometries and evaluate them with LES models. The numerical models were validated with wind tunnel experiments and with additional experimental data selected from the bibliography. The numerical results defined the toxic smoke limits and allowed the creation of simplified risk maps. The latter can define the mitigation measures after a fire accident.

ACKNOWLEDGEMENTS

Firstly, I would like to express my sincere gratitude to my PhD advisor Dr. Panagiotis Tsoutsanis for his continuous support during the course of my research. He has been a true mentor and advisor throughout the course of my study, guiding me and providing me with useful insights and in-depth feedback that contributed to the completion of my thesis.

Besides my advisor, I would like to thank the rest of my thesis committee: Prof. Ioannis Lekakis and Dr. Ioannis Sarris for their insightful comments and encouragement, who helped me enrich my research from various perspectives.

Last but not the least, I would like to thank my family for supporting me throughout this unique journey.

TABLE OF CONTENTS

LIST OF FIGURES

GLOSSARY

CBRN   Chemical, Biological, Radiological Nuclear

CFD   Computational Fluid Dynamics

DNS   Direct Numerical Simulations

FEMA   Federal Emergency Management Agency

FDS   Fire Dynamic Simulator

ILES   Implicit Large Eddy Simulation

LES   Large Eddy Simulation

LNG   Liquefied Natural Gas

PDE   Partial Differential Equations

RANS   Reynolds Average Navier Stokes

rms   root-mean-square

RSTM   Reynolds Stress Transport Model

SGS   Sub-grid Stress

URA   The Urban risk assessment

URANS   Unsteady Reynolds Averaged Navier Stokes

Nomenclature

Roman symbols

A_F	Frontal area of each building	$[m^2]$
A_{ftotal}	Total front area of all buildings	$[m^2]$
A_p	Plan area of each building	$[m^2]$
A_{Ptotal}	Total plan area of all buildings	$[m^2]$
A_T	Total area per roughness element	$[m^2]$
A_{Ttotal}	Total surface area of all roughness elements	$[m^2]$
C_p	Specific heat capacity	$[J/K\ kg]$
f_μ	Damping function	-
h_S	Enthalpy	$[kJ/kg]$
L_s	Mixing length for sub-grid scales	$[m]$
p_∞	Static pressure in the freestream	$[Pa]$
Pr_t	Subgrid Prandtl number	-
$q_{convective}$	Convective mass flux	$[kg/\mathrm{m}^2\ \mathrm{sec}]$
$q_{molecular}$	Molecular mass flux	$[kg/\mathrm{m}^2\ \mathrm{sec}]$
Q_{source}	Contaminant release rate	$[kg/sec]$
$q_{turbulent}$	Turbulent mass flux	$[kg/\mathrm{m}^2\ \mathrm{sec}]$
Re_y	Turbulent Reynolds number	-
Sc_t	Turbulent Schmidt number,	-
u', v', w'	RMS of the fluctuating velocities	$[m/sec]$
U_∞	Freestream velocity	$[m/sec]$

U_{ref}	Velocity at the reference height	$[m/sec]$
z_{ref}	Reference height	$[m]$
$\lambda_f.$	Frontal area density	$[m^2]$
λ_p	Plan area density	$[m^2]$
σ_K, $C_{1\varepsilon}$,$C_{2\varepsilon}$,f_1,f_2	Constants	-
T_∞	Air temperature	$[K]$
Ω_{ij}	Vorticity tensor	-
C_p	Pressure coefficient	-
D^*	Characteristic grid size	$[m]$
G_k	Turbulence kinetic energy production	$[m^2/sec^2]$
J_i	Species diffuse due to turbulence	$[m^2/sec]$
S_h	Heat Source	$[W/m^2]$
U_i	Mean velocity	$[m/sec]$
X_b	Down-stream reattachment	$[m]$
X_f	Upstream separation	$[m]$
X_r	Roof reattachment	$[m]$
g_i	Gravitational vector in i_{th} direction	$[m/sec^2]$
u_*	Friction velocity	$[m/sec]$
u_i	Velocity vector	$[m/sec]$
u_i'	Fluctuation velocity	$[m/sec]$
z_0	Aerodynamic Roughness height	$[m]$
d	Distance to the closest wall	$[m]$
E	Total energy	$[kJ]$

E(k)	Energy spectrum function	$[m^3/sec^2]$
g	Gravity acceleration	$[m/sec^2]$
H	Building's height	$[m]$
K	Non-dimensional concentration coefficient	-
L	Length of the canyon	$[m]$
p	Static pressure	$[Pa]$
Q	Heat rate release	$[W]$
S	Rate-of-strain tensor	-
T	Temperature	$[K]$
t	Time	$[sec]$
V	Volume of the computational cell	$[m^3]$
W	Width between the building	$[m]$
ΔT	Temperature difference between the fire plume and the air temperature	$[K]$
κ	Von Karman constant	-
G(x)	Filter function	-
Ri	Richardson number	-
k	Turbulence kinetic energy	$[m^2/sec^2]$
p	Pressure	$[Pa]$
μ_t	Turbulent viscosity	$[kg/\text{m sec}]$
τ_{ij}	Subgrid-scale stress	$[m^2/sec^2]$
u	Streamwise velocity	$[m/sec]$
v	Spanwise velocity	$[m/sec]$

| w | Transverse velocity | $[m/sec]$ |

Notations

| <x> | Time Average value | $[sec]$ |

Greek Symbols

Δ	Filter width	$[m]$
δ_{ij}	Kronecker delta	-
δ	Boundary layer thickness	$[m]$
ε	Energy dissipation	$[W]$
μ	Dynamic viscosity	[kg/m sec]
ν	Kinematic viscosity	$[m^2/sec]$
ρ	Density	$[kg/m^3]$
		-
Φ_i	Mean pressure, energy, species concentration	
φ'	Fluctuations of pressure, energy, species concentration	-

CHAPTER 1. Introduction

1.1 Introduction

A hazardous release accident, such as a smoke release after a fire accident, could be dangerous to the population's health, could damage property and could cause grave environmental pollution. When a hazardous release accident occurs, the transportation of the hazardous materials released in the open air is defined by the airflow and the complex urban geometry. The dispersion of hazardous materials after an accidental release is a complex physical phenomenon, specifically when it concerns a complex turbulent environment, such as an urban environment.

Different parameters should be studied in order to predict the particles' dispersion in the urban environment and its consequences. The identification, evaluation and prioritization of the risks are defined as the risk management process (ISO 31000). A risk manager for urban design should carefully study different parameters such as the topology, the meteorological data, the atmospheric boundary layer, the nature of the released hazard and its impact on the environment and population. Due to these different parameters and to the uniqueness of each case, the risk manager should calculate the risks using useful modelling tools. The Computational Fluid Dynamics (CFD) techniques could help the risk manager to predict the dispersion pattern, to study different scenarios and to obtain several risk plans. Yet, the CFD techniques require a considerable amount of time to export data. For this reason, in the current research CFD techniques were applied in order to produce a parametric pre-accident method, aiming to define the risk zones of the city and the defence measures against the smoke release after a fire accident.

1.2 Definition of the problem and motivation

The complex gaseous system of atmospheric air has undergone significant changes over time due to human activity. The atmosphere is overcharged from various releases such as industrial plants, cars, transportation accidents, planes, trains, volcanic eruptions, all of which define the atmospheric air quality.

The atmosphere is further burdened by hazardous release accidents which discharge considerable quantities of air chemicals, particulates or other hazardous materials causing damages to the ecosystems and leading, eventually, to human deaths.

The air pollutants could be divided into three different categories:

- The criteria pollutants, which are regulated. These are: Carbon monoxide, Lead, Nitrogen dioxide, Ozone, Particles, Sulphur dioxide.
- The Air toxics/hazardous materials, which include smoke fire, motor vehicle emissions, solid fuel combustion, industrial emissions and materials from buildings, incidents or terrorist attacks.
- Biological pollutants, which include sources from microbiological contamination.

A material could be characterized as a hazardous material if it puts at risk human health, safety, and the environment. An accident which involves hazardous materials should be carefully treated in order to prevent a harmful outcome. The difficulty is to identify a hazardous accident and also to act effectively in order to avoid any risks [1].

A hazardous release could have several possible outcomes. The fact that the outcome is unknown and could differ regarding the magnitude, timing and occurrence has an effect to the definition of the risk. The prevention and the mitigation of a harmful outcome due to a hazardous release should be pre-studied. The systematic process which describes and quantifies the accident's risks associated with hazardous materials is called risk assessment [2].

According to Covello, et al. [2], three major conditions define a risk: a) the source, b) the exposure process of people or things and c) the causal process which threatens health, the environment or property. These steps are defined and analysed during the risk assessment procedure, which determines, characterizes, and quantifies the following causes: a) the possibility that the source could release a hazard; b) the intensity, the frequency and the duration

of the source's release; c) the consequences of the exposure to health and the environment.

Nowadays, more than half of the population lives in cities, and the possibility of a disaster in an urban environment is significantly elevated: the increased population in cities also increases the risk of a hazardous event. The Urban Risk Assessment (URA) has been developed in order to study urban environment risks. Local governments are responsible for integrating URA tools in their cities' protection mechanisms. The lack of experience and insufficient legal framework could, among other things, increase the risk. First, authorities should develop simple risk maps. The local government should identify the critical points where hazardous releases could occur according to the city's activity and to the critical infrastructure (e.g., hospitals, administration buildings, schools). Secondly, authorities should develop loss scenarios through simplified impact models. Both the possible location of a hazardous accident and the damage that could be caused by it should be identified. Third, authorities should undertake a modelling disaster. Modelling techniques, which are risk assessment methods, analyse the data in order to simulate a probabilistic event and analyse the hazardous conditions [3].

URA's main challenge is to estimate the consequences and the impact of a hazardous release in a populated complex. Modelling techniques could estimate the evolution of phenomena and define the consequences for the population's security. These modelling techniques include several dispersion models which could deal with different cases and different consequences of various incidents. According to the Federal Emergency Management Agency (FEMA), an accident is defined by a chain of events which could include the hazardous release and the environmental interaction, the exposure consequences to the society and the property, the impact area, the defined by the accident managers risk assessment and the emergency assessment actions.

Another major problem is the community's response to execute an emergency plan. Emergency managers are responsible for controlling and successfully

applying an action plan. They have to identify the risk and ensure that the appropriated pre-planned risk assessment action will be applied.

The pre-planned risk assessment actions require [4]:

- The definition of the plan, which includes the aim, the scope, the stakeholders and the training.
- The project planning, which includes tasks, responsibilities, timetable, resources, performance indicators
- The project implementation, which includes communication, consultation, performance, monitoring, and review.

1.3 Dispersion models

The behaviour of a hazardous dispersion is modelled with different types of dispersion models having different requirements. According to Holmes, et al. [5], the main dispersion modelling categories are:

a) The box models

The model treats the area as a box, and it is based on the mass conservation law. The advantage of this method is that it studies in detail the chemical reaction of the release as well as the particles dynamics. Due to the fact that it models only the box area it does not provide information on the surrounding area.

b) The Gaussian models.

These models are steady-state models which are based on Gaussian distribution. They take into account diffusion, advection and some of them the chemical reaction and deposition. The main disadvantage of the Gaussian models is that they are not designed for low velocities and their predictions are not reliable on close distances.

c) The Lagrangian models

Lagrangian models are quite similar to box models. The difference is that the Lagrangian model box is following a trajectory as it moves.

d) The CFD models.

CFD models provide a complex calculation resolving the Navier-Stokes equations giving detailed information's about the flow. They could also model the appropriate boundary conditions, such as the meteorological conditions.

1.4 CFD and risk assessment

The airflow and the dispersion pattern of a hazardous release scenario in a complex urban area are difficult to be studied because of the existence of several parameters such as the meteorological conditions, the complex atmospheric boundary layer, the nature of the released hazard, etc. On the other hand, the necessity of studying this kind of scenarios is crucial for emergency risk plans. The rapid development of computers has allowed the emergence of new methods and tools for the study of these problems. One of the tools that risk assessment could use in order to compose a complex plan activity should include a computational fluid dynamic (CFD) approach. The CFD models are the most accurate models even though computational time is considerable. The main disadvantage of the CFD models is that they are time costly and their prediction is never 100% reliable, compensated to the fact that they can model partial equations of motion and mass/heat transfer [6].

This method could provide a quantitative and qualitative estimation of the accident. It could be a useful tool for the dispersion study of the hazardous release. It could also give a prediction for the phenomena for different weather conditions. A priori CFD calculations of the dispersion of hazardous releases inside an urban environment could help the community to estimate the risk of harmful accidents.

The study of accidental releases should be approached in different scales in order to mitigate the accidental danger. The study of the dispersion should define the harmful impact on human beings as well as on equipment and property. This means that the accidental impact could harm: people who are situated around the accident, collateral building structures and array of

22

buildings. At the same time, it could have a general effect on an urban district or part of the city.

This means that different scenarios should be studied for different scales, in order to reduce a harmful event from a hazardous release impact. These scenarios study the consequences of hazardous releases and examine the impact of the accident a) on a nearby distance which could correspond to the size of a building, b) on a wider area which could harm an intersection or a street canyon, c) on an extended area which could include massive hazard dispersion into a city.

According to the risk assessment design, different scales should be studied [7]:

- A mesoscale referring to the city scale
- Street canyon/District scale
- Separate building
- Material/Human Scale
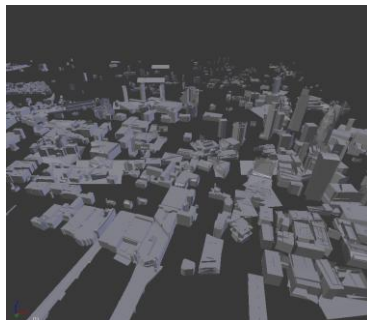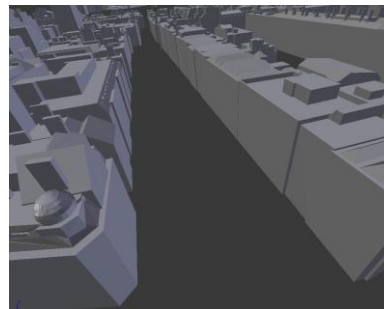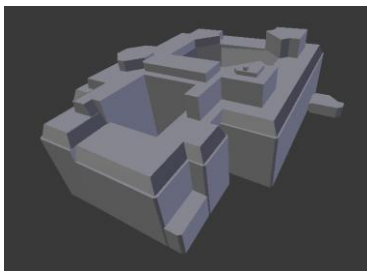
Figure 1-1 Schematic representation of different studies in pollutant dispersion for a) mesoscale, b) Street canyon/District scale, c) Building scale and d) Human scale.

The limited open space inside urban geometries blocks the hazardous materials, increasing, thus, the mass dispersion inside the city's environment. Many of the risk assessments issues are related to the complex flow and turbulent flow which occur in the urban environment [8].

Authorities should have a risk assessment process in order to respond to all kinds of disasters or emergencies, regardless of the cause. A risk assessment process includes an emergency planned process that would allow authorities to be prepared to mitigate any hazardous consequences. The risk assessments are based on quantitative and qualitative criteria of the accident's impact. During the development and implementation of the plan, the steps that should be followed are:

- The identification of the hazard
- The definition of a disaster Scenario for plan development
- The development of a plan

The pre-planned actions provide the advantage of rational decisions in an emergency situation, especially during hazardous release situations. The plan could be applied after the identification of the type and the location of the hazardous release within the community borders.

The hazard assessment methodology defines systematic hazards identification. One of the techniques which should be applied is the application of the checklist technique. The accidental techniques should have recorded the accidental causes and the protection measurements [9].

1.5 Origins of hazardous materials releases

Hazardous materials from incidents could include toxic, flammable, explosive, radioactive, corrosive, oxidizers, biohazards, pathogen or allergen substances and organisms, asphyxiates, which could harm people, all living organisms and the environment. These materials could be liquid, gases or substances [10].

The origins of the hazardous releases could be categorized as [11]:

- Natural emissions (volcanic eruptions, forest fires, etc);

- Anthropogenic emissions which could be classified to planned and unplanned emissions (accidents or terrorist acts);
- Mixed emissions (combination of the above);

The main risk assessment hazardous accidents include the emission of Acetylene, Chemical, Explosives, Biological, Radiation, and Asbestos [10].

The pollution's sources could be categorized by the emission release type, such as a point release, a line release, an area, and volume releases, as well as continuous or volume emission releases.

Another categorization of hazards could be the flammable hazards, the explosives hazards, and the Toxic Gas Dispersion hazards.

A flammable hazard could have as a consequence:

- Jet fires
- Flash fires
- Boiling Liquid expanding Vapour explosions
- Pool fires

An explosive hazard could have as a consequence:

- Confined Vapor Cloud Explosions
- Dust Explosions
- Runaway Reactions
- Unconfined Vapor Cloud Explosions

The term CBRN could be used in order to define the Chemical, Biological, Radiological or Nuclear substances of a material. There are different types of CBRN containing different hazardous consequences. Depending on the type and physical properties of the chemical and biological substances, the main types of hazards are [12]:

- The Contact hazard: Referring to skin contact with the chemical and biological hazards. The hazards could be in vapor liquid or solid phase.

- The Inhalation hazard: Referring to breathing contaminated air which contains vapors, aerosols or dust which could be inhaled into the lungs.
- The Injection hazard: Referring to biological, chemical and radiological hazards which are injected from the site directly to the bloodstream.
- The Ingestion hazard: Referring to biological, chemical and radiological hazards which are ingested into the digestive system.

1.6 Risk Map generation

The study of air flow and smoke dispersion in different urban geometries could help urban planners defining simplified pre-planned strategies in case of a fire accident. The fire position, the urban geometry, the wind direction and the fire intensity are the main parameters that could define the fire fighting measure and the intervention plans. This study offers scientific foundations and suggestions for the generation of a general risk map that could be applied to most city geometries.

A risk map gives information regarding the probability of a hazardous release and the consequences of an accident. The consequences are defined and plotted in a risk area in order to determine the post-accident measures. In this study the toxic zones after a fire accident are defined for different oil fires. A toxic zone is an area which has as a centre the point of the source emission and it extends to the limit where safety is valid. The limits of the zones depend on the toxic material such as smoke, CO and CO_2.
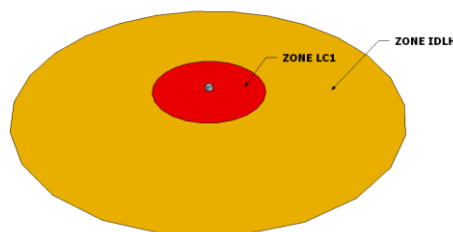
Figure 1-2 A typical risk map of toxic zones

A risk map can be composed after analysing all the different data that characterize the urban environment. The main steps of this data analysis are described by an Urban Risk Assessment methodology [13]. The first pillar of the

Urban Risk Assessment is based on the development of simplified maps of the hazardous impact. In order to define these maps, the following steps should be made:

- Define a base map which shows the major infrastructure (roads, water supply), the land use and the community buildings and finally the environmental area.
- The socioeconomic profile with the population density, the zone's activities (commercial, industrial zones etc.) should be illustrated.
- A hazardous profile with statistics data from past incidents should be collected.
- The areas where the human activity could lead to a hazardous accident should be identified and recorded to a map. The use of GIS systems and satellite images could be used.
- Finally, a map with the identified areas of high risk could be developed.

After the development of a simplified map, impact models could be used in order to estimate the impact after a hazardous incident. The next suggested steps are:

1. To identify the build-up information such as the information of the building's height, the covered area and the use of land.

2. To define the building topology. The urban areas should be classified from the experts to different standard types of buildings and urban block of buildings.

3. To combine hazards and vulnerability data for the development of accidental scenarios.

The final step is to model the disaster scenario. One of the options for this modelling is to simulate the accidental scenario with the use of CFD techniques.

In Figure 1-3 all the steps needed to create a Risk map are described. These are: the topography of the region (terrain of the region), the prevailing wind directions and the atmospheric boundary layer (meteorological data*)*, the building arrangement and their dimensions (GIS data), road networks and

surface materials (Google earth data), the activities related to the region (Zone activities) such as industrial, residential etc., the existing records for accidents that have occur in the past (Statistical records for Accidents).

The wind field, the urban geometry and the position of the fire accidents are inputs for the CFD. The results of the computation consisting from the pollutant dispersion, the flow field and the identification of toxic zones can create a risk map which in combination with pre-planned action leads to firefighting plan.
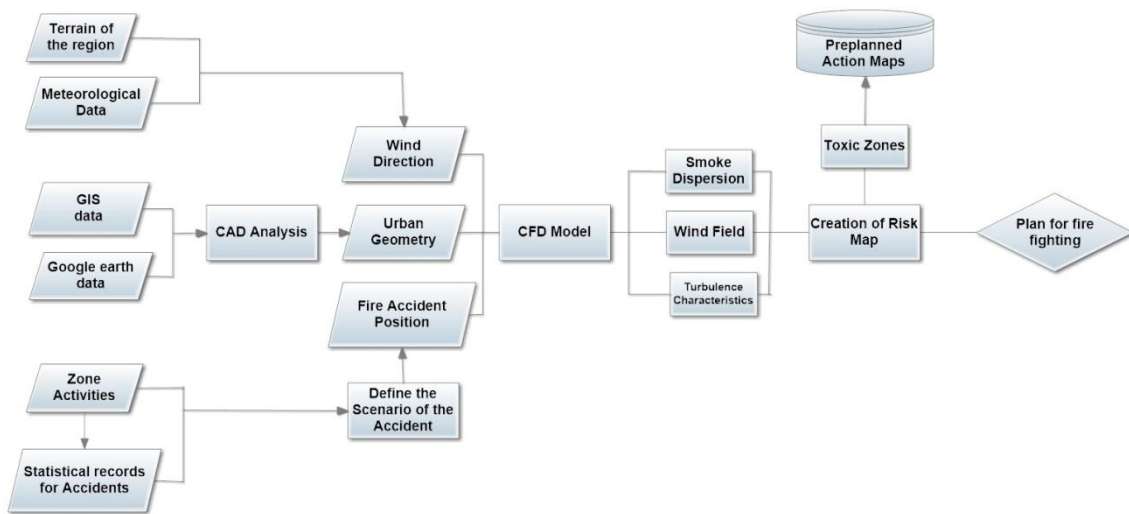
Figure 1-3 A process for the generation of a Risk Map

1.7 Structure of the thesis

The thesis has a paper style format and the chapters have the following structure.

Chapter 1 Introduction

This chapter is an introduction to the basic ideas of the different types of dispersion models, the combination of the CFD models and risk assessment methods, the different origins of hazardous materials releases   and the generation of a risk map.

Chapter 2 Literature Review

This chapter offers a detailed bibliographical review. The general definition and the motivations of the thesis are also described, as well as the general meanings of the CFD and the risk assessment approach. The bibliographical review contains the results from different studies concerning the definition of a hazardous release and the flow behaviour as well as the pollutant dispersion for these selected different urban scale geometries.

Chapter 3 Aims and objectives

This chapter focuses on the aims and objectives of the thesis, defining also that Computer fluid dynamics (CFD) techniques and experimental results are used for the parameterization of the problem. Finally, this chapter mentions the research's originality and the contribution to science, as also its outcomes.

Chapter 4 Theoretical Methodology

This chapter introduces all governing equations used in fluid dynamics such as the conservation of mass, momentum, energy and species. The RANS and LES models that are applied at this research are presented.

Chapter 5 Wind Tunnel experiments coupled with LES simulations

This chapter describes the wind tunnel experiments and the LES models that are conducted during this research in order to define the physical phenomenon of the air flow distribution and the turbulent flux around different urban scales.

The wind tunnel experiments that are conducted are compared with LES simulations using the commercial solver of Fluent. The main parameters that influence the flow distribution around urban geometries inside an atmospheric flow are defined and compared with other numerical and experimental results. Smoke visualization is also conducted in order to define the regions where the smoke concentration is high.

Chapter 6 Assessment of air flow distribution and hazardous release dispersion around a single obstacle using Reynolds-averaged Navier-Stokes equations

This chapter focuses on the study of the flow around a cubical building, with a pollution source at the central point of the top of the cube. The Reynolds-averaged Navier-Stokes and species concentration equations are solved for different numerical schemes and the results are compared against Martinuzzi and Tropea measurements (1993) for the flow field and against Li and Meroney (1983) experiments and Gaussian models for the concentration distribution.

Different kinds of k-epsilon models with different wall functions are examined leading to different numerical results. Each model presents advantages and disadvantages for both the flow representation and the pollutant dispersion.

Chapter 7 LES study of the hazardous release from a fire accident around a cubical building

This chapter focuses on the study of the smoke dispersion from a pool fire in the wake zone of a cubical building. The accidental scenario examined two different scenarios, a crude oil fire and a diesel pool fire. The accidents are studied with the Large-eddy Simulations model for high Reynolds number. The airflow distribution is compared against SILSOE cube experiment data [14, 15]. The buoyancy forces affect the smoke plume distribution inside the wake zone behind the cube. The pollutant concentration around the cube is compared against Tominaga, et al. [16] data from wind tunnel experiments.

Chapter 8 Diesel pool fire incident inside an urban street canyon

This chapter focuses on characteristics of a fire inside a street canyon. A diesel pool fire accident inside a street canyon is studied with a Large-eddy Simulation model. The method is compared fairly well against experimental data. Cases with different inflow wind speeds are studied and the risk zones for the different wind approaching scenarios are defined.

Results show that part of the fire pollutants exits the canyon, while another part is trapped into the canyon due to the local air recirculation. The buoyancy effect due to the fire accident and the inertial effect of the wind flow define the smoke's dispersion. When the wind velocity at the street canyon height exceeds a critical value, the fire's smoke is re-circulated and trapped inside the street canyon. This dispersion is analysed based on the flow characteristics in the street canyon.

Chapter 9 Computational assessment of the hazardous release dispersion from a diesel pool fire in a complex building's area

This chapter focuses on the study of a diesel pool fire accident in a staggered array of cubes studied with a Large-eddy Simulation model. This case is similar to a real urban environment and the determination of the wind distribution and the smoke dispersion is difficult. Three different cases were studied and the toxic zones are defined as well as the risk maps in order to define the measures for a quick fire-fighting response. In a symmetrical geometry of urban blocks, the smoke will symmetrically disperse. Complex geometries without any axis of symmetry could lead to unpredictable flows due to the fact that the wind may prefer to follow a specific path that could not be predicted. Finally, if the fire is placed in a road and the wind is parallel during the accident, the smoke follows the wind direction but it is disturbed from the building's lateral re-circulations.

Chapter 10 Conclusions

This chapter summarizes the conclusions of the each chapter and the main findings of this research and how the aims of this research are achieved. Finally the chapter introduces the future work.

CHAPTER 2. Literature Review

2.1 Introduction

The literature review is focuses on the air flow study around different urban geometries and the dispersion of hazardous materials around these geometries. Three different urban geometries are examined and their literature review is summarised. Additionally, studies with urban air flow distribution and hazardous material dispersion is also reviewed. Finally, studies with fire accidents and smoke dispersion are summarised.

2.2 Flow and dispersion around single obstacles

An isolated building is the smallest urban unit, where the airflow and the dispersion of a hazardous release material should be studied. Different accidental scenarios depending on the point of the accidental source release, the wind oblique angle, the atmospheric boundary profile etc. define a risk. In order to better understand the mechanism of the airflow around isolated buildings, three dimensional studies of the field should be made. As shown in Figure 2-1, vortices are created at the side and top faces of the buildings.
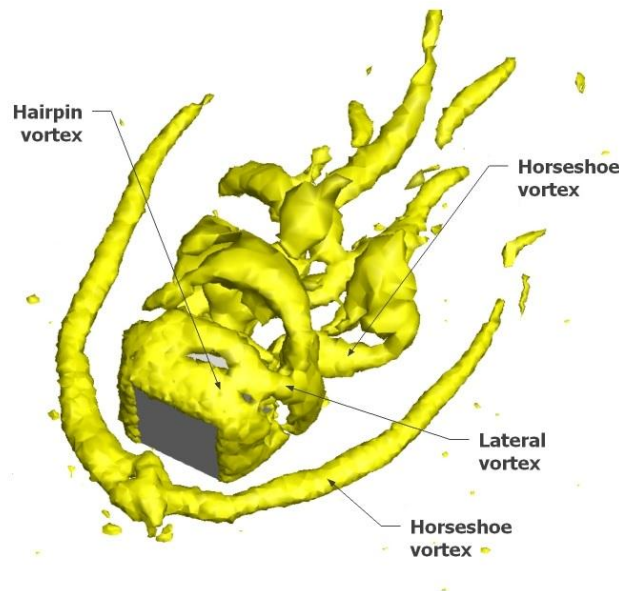
Figure 2-1 Flow structure around a cube

A typical flow around an isolated obstacle: vortical structures are visible in front, at the sides and in the wake of the element.

Several experiments have been conducted so far regarding the flow around cubical geometries. Moreover, a few field experiments exist for the flow around cubical geometries [14, 17]. Castro and Rodin [18] studied the dependence of the wake recirculation and the roof's vortex for uniform and turbulent approaching flows. The Reynolds number is important for the flow characteristics around a cube affecting the mean pressure, the velocity on its surfaces and the fluctuating quantities depending on the wind characteristics [19]. Several experiments for fully turbulent flows examined the flow around a cubical geometry [20-22]. The cost of field experiments and wind tunnel studies has the led researchers to use Computational Fluid Dynamics (CFD) techniques more often in order to study the flow around similar geometrical shapes. Several studies examine the flow around isolated orthogonal geometries with different approaches [23-26] and the pollutant dispersion around them [16].

The usual technique is the numerical solution of the Reynolds-averaged Navier-Stokes equations (RANS or URANS for steady-state or the unsteady formulation, respectively). A promising technique in turbulent calculations is the Large Eddy Simulation (LES). LES approaches to resolve the unsteady motion for the flow around a cube and define complex phenomena such as the vortex shedding, the dynamic loading, turbulence fluctuations [27]. The disadvantage of this method is that it is more expensive than the RANS methods. LES could be an option for the study of flow around isolated bodies such as the flow around a cube [27-30]. LES models, the sub-grid stress (SGS) tensor and the scalar fluxes are defined with a lot of detail, however they have the disadvantage of the computational cost because of the high-resolution requirements. Another much more uncomplicated and computationally more adequate approach is the Implicit Large Simulation (ILES) [31-35]. Direct Numerical Simulations method (DNS) is the most precise numerical approach but so computationally costly that cannot be adapted to geometries such as in an urban environment.

Lakehal, et al. [36] studied the flow around a cube with several k-epsilon models and compared the results with Martinuzzi's experiments. Zhang, et al. [37] studied different types of flows around a building with a k-epsilon model and compare the results with Castro's experiments. This study concluded that the existence of the wind shear influences the location of the upstream stagnation point and the vortex which results from that. The wind shear, as well as the turbulence of the approaching flow, tends to reduce the size of the cavity zone on the leeward side of the building.

Mochida, et al. [38] examined different k-epsilon models for the flow around high-rise buildings with a focus on the basic boundary conditions. Yoshie, et al. [39] studied the differences between a modified k-epsilon model and a standard k-epsilon model to validate the flow characteristics around a cube and found that the modified k-epsilon model is more accurate for areas with high velocities than for regions with lower ones.

A hazardous release around a building could be modeled as pollutant dispersion around a cube. The wind flow and hazard dispersion around a cube are commonly studied with experimental and numerical studies. Due to the fact that wind tunnel experiments are costly, usually numerical studies are conducted and their results are validated against the limited experimental data. In this direction, several wind tunnel experiments can be found that consider the pollutant dispersion from different source positions and different wind-induced angles [40, 41]. Robins, et al. [42] studied the plume dispersion around a cube. Different experiments are realized for different source positions, various speeds of emission release and various wind directions. They clarify experimentally the importance of the turbulent shear stress and how it affects the pressure and the flow distribution. Thompson [43] studied the pollutant dispersion for different height and source locations. Higson, et al. [44] studied the influence of the pollution dispersion around an isolated building. The experiments involved studies both in a field and in a wind tunnel. Upwind of the building, a continuous gas tracer was released, and concentration levels were measured at different

points. The larger plumes and their fluctuations are better simulated in a field than in wind tunnel experiments.

Mavroidis, et al. [45] studied the flow around rectangular and cylindrical obstacles, comparing field experiments with wind tunnel experiments. Their studies focused on plume behaviour originating from sources placed upwind of the obstacles and the centreline concentrations downwind of the obstacles. The study summarizes the mean concentrations for different shapes of obstacles and different wind flow angles and then compares the field and wind tunnel experiments. The concentrations of gas tracer in the wind tunnel are higher than those in the field, and this is mainly due to the large scale turbulence present in the atmosphere.

Due to the additional difficulty of field experiments with pollutants, several numerical studies exist for the pollutant dispersion around cubical geometries [46-49]. Meroney, et al. [50], using the commercial code of Fluent and experimental studies, compared how the gases which were emitted from different sources were dispersed around buildings of various shapes. This study defined that the source concentrations which were released in the area of the bluff bodies were over-predicted when the Reynolds-averaged turbulence models were used. Additionally, the separation and reattachment of the wind flow around a body can be appropriately estimated by an adapted grid without extensive calculation time. Delaunay, et al. [46] compared computational simulations and wind tunnel experiments around a rectangular building containing chimney outlets. In order to reproduce the flow recirculation around the roof-top and the windward and the leeward sides of the buildings, a second-order turbulence model has to be applied. The second-order scheme provides good estimations for the gas concentrations on the sides of buildings.

Tominaga, et al. [48] examined different types of k-epsilon models around a cube and the dispersion of a flush vent which is located on various points at the top of a cube with different air oblique angles. The study exhibited an underestimation of the concentration on the leeward and the lateral sides of the cube due to reduced diffusivity and concluded that the velocity field determines

35

the concentration field. These results were successfully compared against the Li, et al. [40] wind tunnel experiments.

Zhang, et al. [51] have studied the case of pollutant dispersion where the emission is at the near wake of the cube. Some field experiments for the flow around a cube with pollutant dispersion also exist [52-54]. Pollutant dispersion behind a cube with different Froude numbers [51] and fluids with different buoyancy forces are studied [16]. Olvera, et al. [55] also studied numerically the buoyant and the neutral plume dispersion within a cube's recirculation cavity. Similar to the downwind release an upwind release was studied by Olvera, et al. [56].

2.3 Flow in urban canyon

The street canyon is an urban unit that is defined by two buildings on both sides. A road with flanked with buildings on both sides could also be characterised as a street canyon. The dimension of the building's height (H) and width between the building (W) and length of the canyon (L) are the geometrical characteristics of the canyon [57].

As shown in Figure 2-2, Oke [58] characterized the airflow in a street canyon as isolated flow when H/W $\leq$0.3, wake interference flow when H/W $\approx$0.5 and skimming flow when H/W $\approx$ 1, the wind speed is perpendicular to the canyon and the speed is greater of 1.5 m/sec above the canyon.
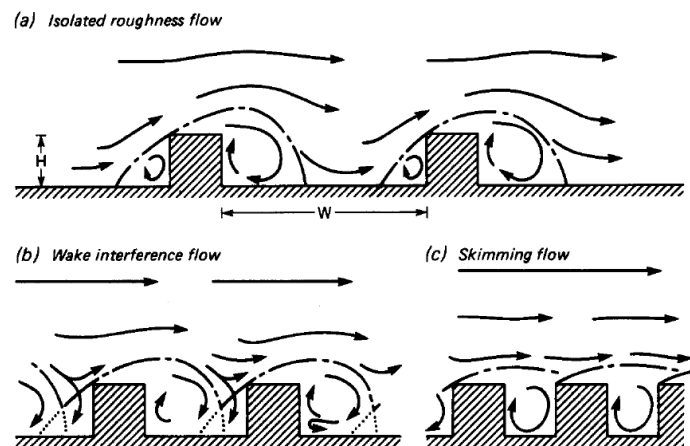
Figure 2-2 Flow regimes and airflow in a street canyon, from Oke [58]

Street canyon flow and dispersion is widely studied in the bibliography. Several analyses have been written regarding the flow inside the street canyon. Wind tunnel studies [59, 60] and water tunnel studies [61, 62] provide data under repeatable and fixed conditions. Several field experiments [63, 64] and outdoor scale models [65] have investigated the spatial flow pattern inside a street canyon. Several studies focus on the field experiment in a regular street canyon (H/W=1) with dispersion [66-68].

Stathopoulos, et al. [69] experimentally studied the wind behaviour in a passage created by two buildings in a wind tunnel. Their work concluded that the conditions of turbulence are more important for winds that are perpendicular to instead of at an angle to the canyon's centre line. In addition, when the width of the passage is greater, lower velocity amplifications and higher turbulence intensities are observed.

Another approach for the study of the flow and the dispersion inside a street canyon is the Computational Fluid Dynamic approach (CFD) with different computational methods. Several numerical 2D simulations for the flow and dispersion inside a street canyon are conducted for a regular street canyon (H/W=1). The Reynolds-averaged Navier-Stokes (RANS) k-epsilon model in a two-dimensional geometry is a common numerical approximation for the definition of the flow [70] and the dispersion [71, 72] inside a street canyon. Three-dimensional studies with k-epsilon model [73] could describe more complex phenomena such as the helical vortex inside the canyon [67, 74]. Several LES studied the flow inside a street canyon, in a two dimensional [75] or a three dimensional mode [76].

Chu, et al. [77] studied the dispersion characteristics in city geometries for different wind speeds and for different directions using computational fluid dynamics software. The perpendicular small wind speeds block the dispersion inside the canyons. As the wind velocity increases, the pollution distribution decreases closer to ground level. On higher levels using buildings that are of different heights, the pollution concentrations are lower. This is due to the fact

that pollution dispersion needs time to reach higher levels and that turbulence is created from the buildings, resulting in the pollution's spread.

Blocken, et al. [78] examined the behaviour of wind inside a building passage with computational methods and evaluated the results obtained with Stathopoulos's wind tunnel experiments [79]. They categorized the flow through a building passage into three types. The first type, the resistance, refers to a flow in a narrow passage with no flow separation and high flow resistance. The second type, the interaction flow, refers to a passage jet that originates from the building entrance corners. Finally, the isolated flow refers to two separate corner flows which do not interact inside the passage.

Baik, et al. [71] applied a k-epsilon turbulent model in order to study a two-dimensional flow inside a street canyon. With their simulations, they have defined that the main characteristics of flow inside a canyon are the number and the intensity of produced vortices. As the ratio of the building height to the width canyon is increasing, the number of vortices increases also. Turbulent kinetic energy is higher in the downwind building compared to the upwind building area. It was also found that the vortex movement inside the canyon has a significant role in the pollution dispersion

Kim, et al. [72] numerically studied the influence of the inflow turbulence intensity on the flow inside a street canyon and the pollutant dispersion. They found that the increase of the inflow turbulence causes the increase of the turbulence diffusion inside the street canyon. They also concluded that this increase causes the rise of the horizontal wind velocity at the roof level, which results in (a) the vortex's enhancement within the street-canyon and (b) the increase of incoming turbulent eddies inside the canyon. Finally, the rise in the inflow turbulence causes high pollutant concentrations, which decrease over time.

Chang, et al. [80] illustrated the flow and transport from a steady point source of pollution around a bluff body and inside a street canyon. They found that inside the street canyon, there are two circulation flows, the upper and the lower. The lower circulation flow in the low area, which is anti-clockwise, carries the

emission gases to the wall areas which are both upwind and downwind. These two areas constitute the upper circulation flow, which moves clockwise. This circulation flow results in higher concentrations of emissions which are more important in the upwind wall areas and less important in the downwind wall areas.

Chan, et al. [81] studied the pollutant dispersion characteristics for different types of street canyons. They used the k-epsilon model to predict the flow characteristics for different geometries of the street canyon. The complexity of the problem led the researchers to conclude that a formula which calculates the pollution concentration was not feasible. Guidelines for pollution dispersion were proposed, which claimed that better canyon ventilation could be achieved when the height of the leeward building is equal or slightly higher (a ratio of 1 and 1.25) than the height of the windward building. In addition, they found that broad canyons led to adequate pollution diffusion. Finally, they concluded that the position of the source pollution did not play an important role for the pollution dispersion

Galani A. [82] simulated the pollution levels of carbon monoxide in urban areas and compared the results with experimental studies. The study concluded that wind speed, wind direction, and the height of the buildings influence the dispersion process. They concluded that computer simulation over-predicts the pollution levels compared to those of the experimental studies. For similar emissions, pollution concentration is higher inside the street canyons than where two street cross due to the street-canyon vortex. Although velocities are higher inside the street canyons than the street junctions, the dispersion is lower.

Garcia Sagrado, et al. [83] numerically and experimentally studied the flow behaviour and pollutant dispersion inside a street canyon, focusing on street canyons situated in open country and non-isolated canyons. The main parameter examined is the influence of the downward building height to the flow. Increasing the height of the downstream building, the pollution concentration diminishes because fresh air enters the canyon. They observed

also that an open country street canyon concentrates fewer pollutants than the non-isolated canyon.

Nazridoust, et al. [84] based their research on different street canyon geometries which were studied using different numerical methods and the results were compared to experimental data. The results of the Reynolds Stress Transport Model (RSTM) method were similar to the experimental data. These indicated that in the case where the pollution source was outside the street canyon, the pollution concentration was considerably greater on the lee side of the building compared to the windward side. Additionally, they discovered that when the wind speed increased, this resulted in the amplification of this phenomenon. On the contrary, when the source pollution was in the street canyon, the concentration of pollution particles was higher on the windward wall than the leeward wall. As the wind speed increased, this difference also increased.

Ayata [85] examined the air velocity and pressure distribution around buildings with different roof shapes using the commercial CFD code of ANSYS Fluent. He noticed that isolated buildings were more exposed to cold winter winds than buildings in urban areas. The k-ε turbulent model was used to examine the wind distribution around detached buildings of different heights with pitched roofs or without roofs. The study concluded that the existence of a roof increased the wind protection of the house, decreased the wind magnitude at the top and also decreased the air velocity in the front area. Finally, they compared the flow characteristics of a pitched-roof house with the flow behaviour around a rectangular and a pyramidal body.

Vardoulakis, et al. [57] reviewed the model techniques and available software for calculating the air quality inside a street canyon. They observed that researchers are obliged to use different monitor and model techniques in order to analyse the pollution concentration inside a street canyon. The most representative studies for the street canyon research are full-scale experiments, reduced-scale experiments, parametric modelling using field and/or wind tunnel measurements, CFD modelling using field and/or wind tunnel measurements,

and finally theoretical CFD modelling. They also indicated that there is an increased concentration in the leeward side which decreases with height.

An accident with a fire inside a street canyon could be characterized as a bottom heated case. The resulting flow patterns are complicated. Several RANS k-epsilon model studies examine the flow inside a street canyon with a bottom heating [86, 87]. But few researches report a fire inside a street canyon [88-90]. LES models also examine the flow characteristics of a flow in a street canyon for with different aspect ratio, pollutant dispersion and heating at the bottom [91]. A small number of analyses focus on the fire study inside a street canyon using the FDS code [89, 92-94]. Other studies focus on codes comparisons inside a street canyon [80]. Different studies for a pool fire accident in an open space exist [6, 9, 95-99].

2.4 Flow in a Building Array

Some field experiments have investigated the pollutant dispersion in a city [100-102]. Yet, field experiments for pollutant dispersion in a real urban environment are very difficult and costly. Different CFD techniques could be applied in order to study complex urban dispersion problems [103-105]. The air flow within the urban atmospheric boundary layer is also experimentally studied with wind tunnel experiments [106].

In order to define the complex phenomena of an urban geometry, simplified cases for the urban building blocks are studied. The urban building blocks areas can be simplified into arrays with rectangular buildings. Urban building blocks are characterized by the buildings' height and the space between them [107, 108]. Different studies exist for the study of the flow into elementary urban units such as the street intersections [109-111], the influence of the tall buildings in the urban environment [112, 113] and in open spaces [114]. Moreover, the flow and pollution dispersion around staggered and aligned groups of cube arrays is examined [115].

The simplified geometries that are created by blocks are called arrays. There are different types of arrays such as the aligned and staggered arrays. Figure

2-3a shows a geometry with uniform aligned arrays of cubes and Figure 2-3b shows a uniform geometry of staggered arrays of cubes. Comparing these two geometries for the same inlet conditions, the staggered arrays shows a greater drag force that the aligned geometry [116].

a)   b)
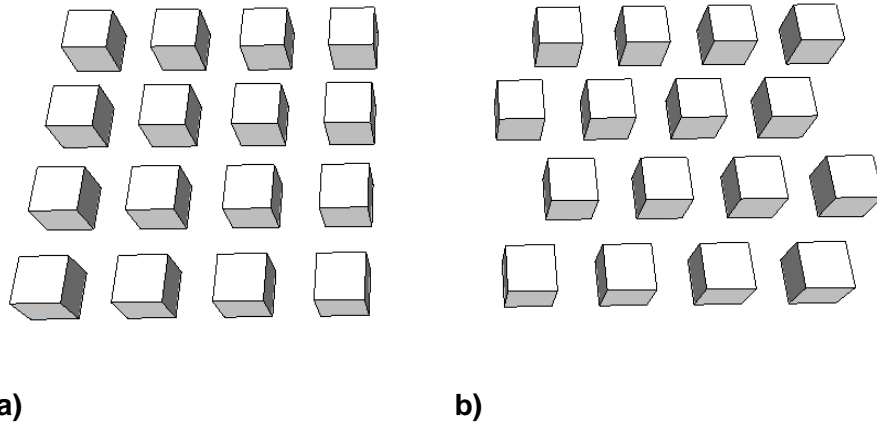
Figure 2-3 Geometry of a) an aligned array and b) a staggered array of cubes

The main characteristics of the building's dimensions of an urban area are defined by Grimmond, et al. [117] which are the distance between the buildings, and the area covered by them. As shown on Figure 2-4, A_p is the plan area of each building, A_T is the total area per roughness element and A_F is the frontal area of each building. They also defined the plan area density λ_p and the frontal area density λ_f.

As plan area density, λ_p, is defined as:

$$\lambda_p = \frac{A_{Ptotal}}{A_{Ttotal}}$$

(2-1)

where A_{Ptotal} is the total plan area of all buildings and A_{Ttotal} is the total surface area of all roughness elements.

As frontal area density, λ_f, is defined as:

$$\lambda_f = \frac{A_{ftotal}}{A_{Ttotal}}$$

(2-2)

where A_{ftotal} is the total front area of all buildings.
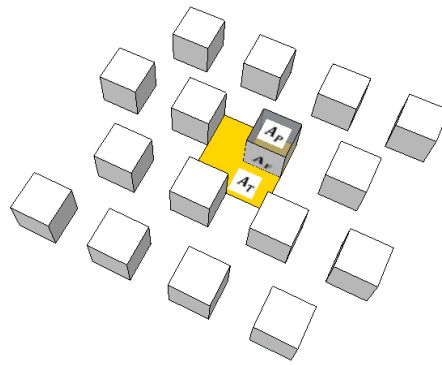
Figure 2-4 Definition of the surfaces dimension of arrays of cubes

Cheng, et al. [118] experimentally studied the aerodynamic characteristics of uniform array of cubes for different roughness elements to the total surface area, λ_p, (25% and 6.25%). Their research defined that the friction velocity should be calculated from the shear stress that is derived from the roughness elements and not the Reynolds shear stress in the log-law region.

Mavroidis, et al. [119] experimentally examined the pollutants dispersion within a building array. Arrays with small spacing between each building behave as a continued solid step reducing the lateral dispersion and vertical spread of the plume. Arrays with large spacing cause large pollutant dispersion between gaps. Another important study was that a taller building embedded in the building array entrained the pollution dispersion into the recirculation region which it creates. Finally, higher mean concentration was observed in building arrays than in isolated buildings

Davidson, et al. [115] experimentally studied the wind flow behaviour and pollution dispersion around staggered and aligned groups of arrays. Mean velocity was significantly decreased inside the staggered and aligned arrays. This reduction was around 45% of the upstream mean velocity. They concluded that the plume's characteristics were affected by the ways that the streamlines and turbulence diverged and converged. Another conclusion was that when the array increased in height, this caused the vertical height of the plume to increase and also created a small change in the way that the mean pollution concentration spread laterally. Lateral and vertical eddy diffusivities indicated a

little difference between the staggered arrays case and no-array case. Plume dispersion inside the staggered arrays was similar to results where no arrays existed. Aligned arrays reduced the lateral eddy diffusivity and impeded the lateral plume dispersion.

A pool fire accident may occur in the open space between urban building blocks. The pollutant dispersion into an array of cubes is experimentally and computationally studied [65, 107, 120], but there is a lack of documentation for a fire incident inside an array of cubes [121].

2.5 Urban areas and CFD

The modern risk assessment design has new tools in order to develop an extended action plan during an accidental release. New virtual geographical information programs, such as Google Earth, give the possibility to the risk assessment designers to collect more accurate data about the urban geometry in order to display and analyse the damages and the risk of a hazardous scenario.
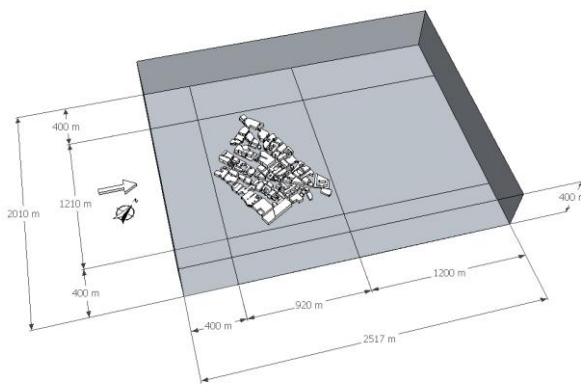
a)   b)

Figure 2-5 The geometry of a)a model area of area in the centre of London and b) the map from (source: Bing maps)

An essential problem of the urban aerodynamics is the need for large computational domains and thus the increase of mesh requirements. The flow characteristics define the grid resolution to achieve accurate and computationally efficient solutions. Different grid types could be applied to

discretize an urban domain: Cartesian grids and unstructured grids. Generating an unstructured grid for complicated geometries is a significantly faster automated process compared to a structured one. On the other hand, all the numerical methods exhibit dependency on the quality of the grid employed, and since unstructured grids are mainly used for complicated geometrical definitions, they can consist of various element types and significant variations of grid quality can be noticed. This, in turn, can pose several challenges for the numerical methods and their formulations when employed in the RANS framework as identified by Antoniadis, et al. [122] using unstructured meshes. However, it is not realistic to apply structured grids into a complicated geometry [123]. Non-orthogonal cells should be avoided near wall treatment cells and boundary conditions. Prismatic or hexagonal cells are preferred for the near wall turbulence models [124]. Blocken, et al. [78] have studied the grid resolution for a passage between two equal height buildings. A hybrid mesh which is the combination of a structural hexahedral grid and an unstructured tetrahedral grid is tested. The structured grid is applied at the building's roof, the building's sides and the passage. The unstructured grid is used for the connection of the building's roof and the domain's centre. Hooff, et al. [125] studied a combination of the urban wind flow to a building's natural ventilation approach. They described a body-fitted grid generation process for the complex internal and external environments. This study defined the steps of the grid generation and the required resolution to control the quality of the results. This process is in contrast to a semi-automatic unstructured grid generation procedure which can lead to insufficient control of the grid resolution, the volume skewness, the grid stretching and the aspect ratio. Gargallo-Peiró, et al. [126] presented a method which can introduce the methodology of meshing the geometry and the landscape of a city. They used 3D unstructured tetrahedral meshes for non-viscous urban simulations for flows around blocks of a city.
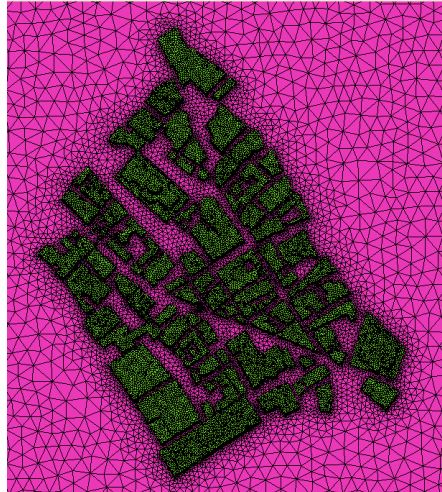
Figure 2-6 Unstructured mesh geometry of an area in the centre of London

Pontiggia, et al. [127] simulated an accidental release scenario of industrial hazardous material. This kind of accidents could be related to accidental events or terrorist attacks. The accidental scenario, which is based on a real event, describes the derailment of a train which was carrying LNG wagons. The accident produced cloud ignitions, which were followed by a flash-fire and had as consequence a near house affection. The study investigates the real effects of the accidental event with the predictions of a CFD model. The simulation of this heavy flammable gas in a complex urban environment with the standard k-ε model was in accordance with the real resulted from damages

Schatzmann, et al. [128] referred to the difficulties of urban CFD models validation form experimental and wind tunnel experiments. Their work has as motivation the COST Action 732 methodology which is a reliable standard for Urban CFD studies. Considering the fact that all measured data have a certain degree of uncertainty, this study presents the field and wind tunnel experiments data variability. Due to the large atmospheric turbulence, field measurements lack representativeness and introduce considerable variability. On the other hand, wind tunnel measurements could represent only neutral atmospheric flows, and the quality of the experiment depends on the approaching flow conditions. The ideal CFD model validation process combines wind tunnel and field experiment data.

Pontiggia, et al. [129] studied a CFD model for hazardous releases in an urban environment. They described with details all the necessary steps to model an urban environment in order to be studied with a CFD code. The hazardous release was modelled with a user-defined function which defines the dose concentration of the hazardous material, as well as the unsteady time interval. The CFD hazardous release solution has been compared to an integral model and it was concluded that it underestimates or overestimate the hazardous release consequences.

2.6 Fire accidents and smoke dispersion

In a case of a building fire in an urban fire accident or a wildlife fire near an urban area the smoke dispersion is defined by the wind and the fire buoyancy forces. In order to better understand the smoke dispersion, it is important to define the wind distribution around both complicated and simplified urban geometries [130].

Węgrzyński, et al. [131] divided the smoke's dispersion in wind conditions into six different categories: a) the indoor flows; b) the natural smoke ventilators; c) the tunnel ventilation; d) the wildfires e)the firebrand transport and f) the urban dispersion.

The fire's spread is influenced by the flame height and width [132], as well as the wind velocity [133]. The burning fuel type defines the fire and smoke characteristics [134-136]. The fire and smoke dispersion behaviour is different in an open space area than in an enclosed environment. For this reason the design of a building is defined by the pressure distribution due to wind forces acting around its walls. The areas with low pressure are acting as a suction of the inlet building's air while overpressure areas can be used for fresh air supply. Even though the pressure distribution around a building is the main mechanism that defines the smoke dispersion in the interior of a building after a fire accident [137-141], it is also important to define the wind flow around it in order to determine the smoke's dispersion with accuracy. The recirculation zones are areas with low velocities and important presence of turbulence. The buoyancy

forces and the external forces due to the wind movement are responsible for the smoke movement [142].

Cleaning the smoke of a building could be achieved by natural convection through roof vents.[140, 143] or by creating a high (positive) pressure zones, such as the stairwell and driving the airflow into fire zones [144]. Several researchers also study the natural ventilation and smoke distribution into atrium [138, 141, 145] or multi-store building [146]. The pressure distribution inside a building and the smoke ventilation of its interior is also influenced by nearby buildings [147].

The smoke dispersion after a fire accident inside a road or railway tunnel is a well documented subject due to its technical approach [148-153]. Another well documented area is the smoke spread after a wildland fire, as well as a wildfire interacting with an urban environment [154, 155]

The study of fire and smoke dispersion inside an urban environment is complicated and difficult to define due to the complex wind distribution around the complex building geometries [156] such as the street canyons [157, 158] or the urban environment [159].

CHAPTER 3. Aims and objectives

3.1 Introduction

This study focuses on the analysis of the dispersion of hazardous material in the urban environment after an accidental release more specifically the smoke dispersion after a fire accident at different scales of urban geometries. The urban environment is a complex geometry and none of the existing models can define the hazardous material dispersion precisely. In order to tackle effectively a hazardous dispersion, the first step is to simplify the geometry of the buildings and to remove any non-important information. The second step is to simplify the complex urban geometry to basic urban units and study them independently. In some of the urban areas a pattern approximation could be identified and accidental scenarios could be examined in order to predict the dispersion of a hazardous release. With simplified plans of the accidental scenarios for different airflow distributions, the risk area could be estimated and a risk map could be plotted. This study examines three typical urban geometry scenarios which are usual in urban cities. These are: a) the flow around an isolated building, b) the flow in a street canyon and c) a staggered building's array geometry.

In order to define the toxic zones, the risk manager should identify the possible positions of the fire accidents, combine them and analyse the consequences considering external parameters such as the airflow. A risk map analysis should take into consideration all the possible scenarios of accidents and create a practical deliverable which could be used for the treatment of the accidental consequences. Figure 3-1 combines all the possible scenarios of an accident around an isolated building for different source positions and two different angles of wind oblique. Similarly, Figure 3-2 and Figure 3-3 combine the different scenarios for a street canyon and a staggered array of buildings respectively. Cases were the source position is placed at any side of the cube are not examined in order to reduce the number of cases.
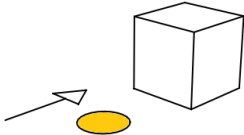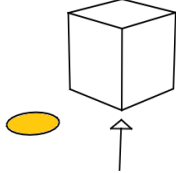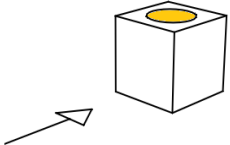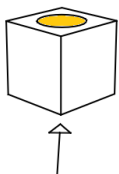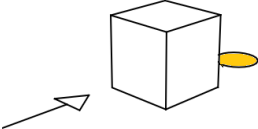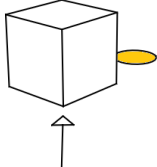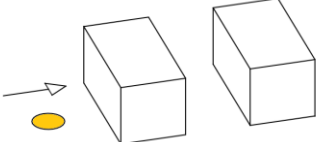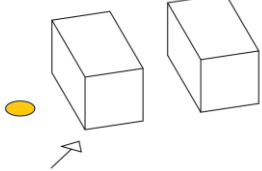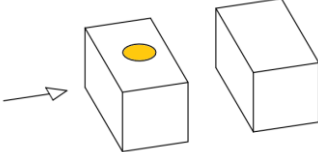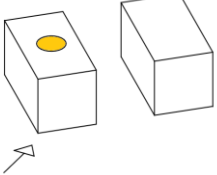
	Wind perpendicular to the cube front face	Wind approaches with an oblique angle of 45°
Pool fire located upwind of the isolated building		
Pool Fire located on the roof of the isolated building		
Pool Fire located on the wake of the isolated building		

Figure 3-1 Typical accidental scenarios for a hazardous release accident around an isolated building for different angles of wind oblique

	Wind perpendicular to the street canyon arrangement	Wind approaches with an oblique angle of 45°
Pool fire located upwind of the street canyon		
Source release at the roof of the upwind building of the street canyon		
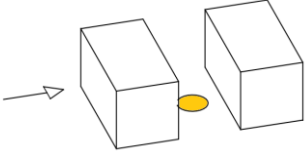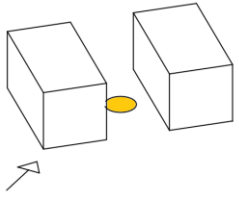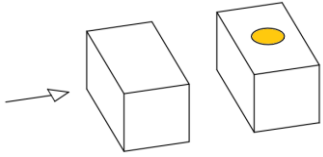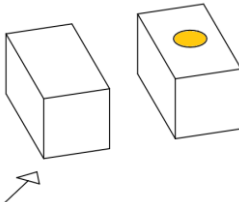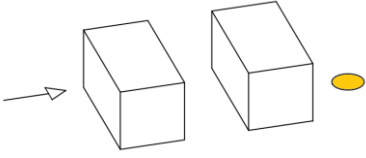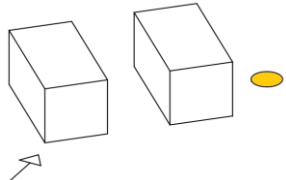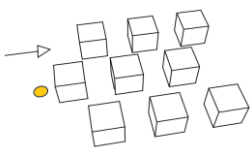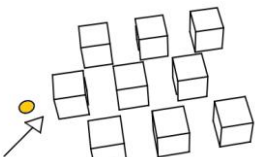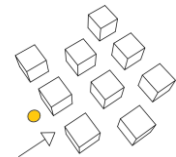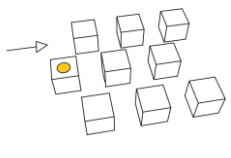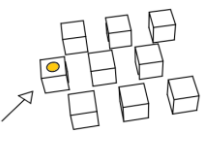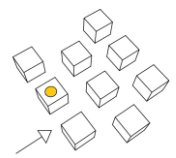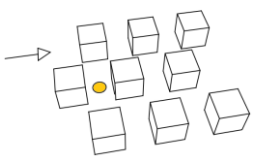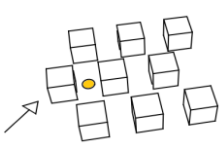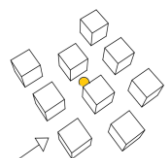
Source release inside the street canyon		
Source release at the roof of the leeward building of the street canyon		
Source release windward of the street canyon		

Figure 3-2 Typical accidental scenarios for a hazardous release accident in and around a street canyon for different angles of wind oblique

Wind perpendicular to the staggered nine cube array format	Wind approaches with an oblique angle of 45°	Wind perpendicular to the staggered nine cube array format
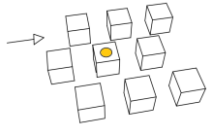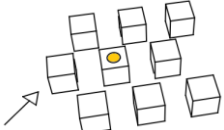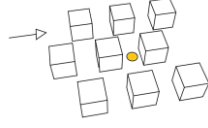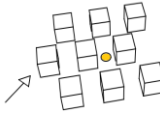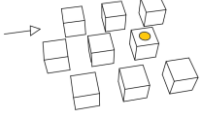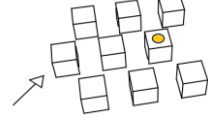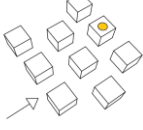
Figure 3-3 Typical accidental scenarios for an accident in and around a staggered array of cubes for different angles of wind oblique

For the purpose of this current research selected cases with references at the bibliography are studied in order to define the air flow, the hazardous dispersion and the toxic zones for a risk map generation.

3.2 Aims and Objectives of the thesis

The aim of this study is to define the dispersion of a hazardous materials, and more specifically the smoke dispersion after a fire accident at different scales of urban geometries. This research is based on a parametric analysis, in order to identify the risk points and critical conditions where a smoke fire's release will be followed by a harmful event.

The thesis' objectives are:

- To conduct parametric analysis for different points in a city, in order to predict the critical **conditions** of a harmful accident due to a fire's smoke release.

- To identify and analyze the **external parameters,** such as the airflow, and the meteorological conditions relating to the accident's evolution.

- To build a **qualitative and quantitative analysis** of a fire's smoke release accident for different simplified urban scales examples.
- To identify realistic **accident scenarios** that could occur in an urban environment.
- Using the results from the parametric analysis, to compose a **risk analysis map**

Computer fluid dynamics (CFD) techniques will be used in order to define the design criteria. The obtained results will be compared to experimental results.

Selected scenarios from Figure 3-1, Figure 3-2 and Figure 3-3 are studied with CFD and experimental methods.

3.3 Contribution to Science

This thesis focuses on the dispersion of a fire's smoke release in different units of the urban environment after an accident and on the definition of the risk zones in order to compose a risk map for intervention measures. It adds both to the fluid dynamics and fire safety literature by offering an in-depth analysis of how fluid dynamics can actively contribute to fire safety strategies.

The definition of the toxic zones inside an urban environment is not, as of yet, described in the bibliography due to the difficulty of the combination of the complex flow distribution and the definition of danger limits of the smoke concentration. This study is a first attempt to define the danger limits for simplified urban geometries after an accidental smoke release.

More specifically, the research's originality lays upon:

- The study of the smoke dispersion following a fire accident around simplified geometries for different scales of urban geometry. More specifically a cube, a street canyon and arrays of cubes. Most studies focus on pollutant dispersion rather than smoke dispersion. The present research attempts to fill the existing literature gap.

- The definition of the toxic zones of the smoke dispersion around the simplified geometries which is not very common in the current fire safety literature.
- The composition of risk maps at different scales of urban geometries, combining scientific criteria in order to generate applied mitigation risk strategies for safety policies.

The following list of articles published or in the process of publication constitutes a concrete outcome of this research.

Published:

Chapter 6 [160]: Vasilopoulos, K., I.E. Sarris, and P. Tsoutsanis, *Assessment of air flow distribution and hazardous release dispersion around a single obstacle using Reynolds-averaged Navier-Stokes equations.* Heliyon, 2019. 5(4): p. e01482.

Chapter 8 [161]: Vasilopoulos, K., I.E. Sarris, I. Lekakis, and P. Tsoutsanis. *Diesel Pool Fire Incident Inside an Urban Street Canyon.* 2019. Singapore: Springer Singapore. (In book: Proceedings of the 1st International Conference on Numerical Modelling in Engineering, pp.339-350)

Chapter 9 [121]: Vasilopoulos, K., M. Mentzos, I.E. Sarris, and P. Tsoutsanis, *Computational Assessment of the Hazardous Release Dispersion from a Diesel Pool Fire in a Complex Building's Area.* Computation, 2018. 6(4): p. 65

Ready for publication:

Chapter 7: Vasilopoulos, K., I. Lekakis, I.E. Sarris, and P. Tsoutsanis,

Large eddy simulation of the hazardous release from a fire accident around a cubical building

CHAPTER 4. Theoretical Methodology

4.1 Navier-Stokes equations

The fundamental laws of fluid mechanics are described by non-linear partial differential equations (PDE). The Navier-Stokes equations consist of time-depended continuity equations for conservation of mass, momentum and energy equations [162]. The governing equation for a Newtonian fluid of the continuity Equation is defined as:

$$\frac{\partial \rho}{\partial t} + \frac{\partial}{\partial x_i}(\rho\, u_i) = 0 \qquad (4\text{-}1)$$

and the momentum Conservation Equation is defined as:

$$\frac{\partial}{\partial t}(\rho\, u_i) + \frac{\partial}{\partial x_j}(\rho\, u_i\, u_j) = -\frac{\partial p}{\partial x_i} + \frac{\partial}{\partial x_j}\left[\mu\left(\frac{\partial u_i}{\partial x_j} + \frac{\partial u_j}{\partial x_i} - \frac{2}{3}\delta_{ij}\frac{\partial u_i}{\partial x_i}\right)\right] + \rho g_i \qquad (4\text{-}2)$$

where u_i is the velocity of the coordinates for the three directions, p is the pressure, µ is the viscosity, δ_{ij} is the Kronecker delta, ρ is the density of the fluid, g_i is the gravitational vector in i direction.

The energy equation using the concept of Reynolds to turbulent momentum transfer is given by the following equation:

$$\frac{\partial}{\partial t}(\rho\, E) + \frac{\partial}{\partial x_i}u_j\,(\rho\, E + p) = \frac{\partial}{\partial x_j}u_i\left[\mu_{eff}\left(\frac{\partial u_j}{\partial x_i} + \frac{\partial u_i}{\partial x_j} - \frac{2}{3}\frac{\partial u_i}{\partial x_i}\delta_{ij}\right)\right] + S_h \qquad (4\text{-}3)$$

Where E is the total energy, S_h is a source heat.

4.2 Turbulence

The turbulence is composed by different sizes of eddies which are characterized by a characteristic length scale defined by the flow velocity scale and the time scale. The larger eddies with higher kinetic energy are breaking to smaller eddies with lower kinetic energy. Finally, the smallest eddies are reaching to a length that the viscosity of the fluid dissipates the kinetic energy into internal energy. The Kolmogorov theory stated that for high Reynolds

number, the small scales turbulence motions are statistical isotropic but the large scales are not. This means that the small scales of turbulence scales are universal for all flows. The small scale eddies can be characterized by the Kolmogorov length scale n ,which is defined by the ratio of kinematic viscosity v to the energy dissipation ε:

$$n = \left(\frac{v^3}{\varepsilon}\right)^{\frac{1}{4}}$$

(4-4)

The Kolmogorov scales for the velocity and time can be given as follows:

$$u_n = (v\,\epsilon)^{\frac{1}{4}}$$

(4-5)

$$\tau_n = (v\,\epsilon)^{\frac{1}{2}}$$

(4-6)

The ratios of the Kolmogorov scales over the characteristic scales present in the mean flow, are related to the global Reynolds number and are given by the following equations:

$$n/l = Re^{-3/4}$$

(4-7)

$$\frac{u_n}{u} = Re^{-1/4}$$

(4-8)

$$\frac{\tau_n}{\tau} = Re^{-1/2}$$

(4-9)

The smallest and larger scales of turbulence can be defined. The energy is transferring from the larger to the smaller scales of energy (scales smaller than l and higher than n) , and it is characterized by the heat dissipation rate ϵ.

The turbulent flow is characterized by the kinetic energy distribution at different scales. This distribution is usually characterized by the energy spectrum function E(k), where k is the wave-number corresponding to a harmonic at the Fourier transform of the velocity.

The representation of the contribution to the kinetic energy from the Fourier modes is defined as:

$$\frac{1}{2}\langle u^2\rangle = \int_0^\infty E(k)dk$$

(4-10)
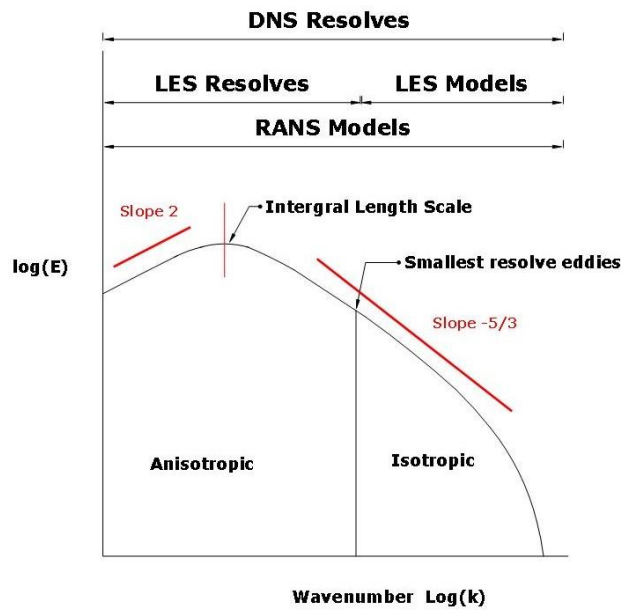
Figure 4-1 Energy spectrum against the inverted length in a log scale [163]

According to Figure 4-1 the energy spectrum is divided to three different ranges: a) the energy containing energy (slope 2); b) the inertial length scale and c) the Dissipation rate 9 (slope -5/3). The turbulence kinetic energy must be scaled properly. A graph with the energy spectrum against the invert length scale defines (the integral length scale defines the eddies with the most energy) is situated at the peak value as shown in Figure 4-1.

The DNS method resolves all the scales of the turbulent spectrum without any turbulence model. The RANS method is based on the statistical description of the flow and the equations are described with mean quantities. Finally, the LES models resolve the large eddies and model the smaller eddies.

4.2.1 RANS equations

In Reynolds averaging the variables are decomposed into their mean value and the fluctuate value. The velocity components are decomposed as :

$$u_i = U_i + u_i'$$

(4-11)

The same is applied for all the others scalar quantities:

$$\varphi = \Phi_i + \varphi' \tag{4-12}$$

where U_i is the mean velocity, u_i' is the fluctuation velocity, Φ_i is the mean pressure, energy, species concentration and φ' their fluctuations.

Substituting equations (4-11) and (4-12) to equations (4-1) and (4-2) the continuity and momentum equations can be written as:

$$\frac{\partial \rho}{\partial t} + \frac{\partial}{\partial x_i}(\rho\, U_i) = 0 \tag{4-13}$$

and the momentum Conservation Equation is:

$$\frac{\partial}{\partial t}(\rho\, U_i) + \frac{\partial}{\partial x_j}(\rho\, U_i\, U_j) \tag{4-14}$$

$$= -\frac{\partial P}{\partial x_i} + \frac{\partial}{\partial x_j}\left[\mu\left(\frac{\partial U_i}{\partial x_j} + \frac{\partial U_j}{\partial x_i} - \frac{2}{3}\delta_{ij}\frac{\partial u_i}{\partial x_i}\right)\right] + \frac{\partial}{\partial x_j}\left(-\rho\,\overline{u_i'u_j'}\right)$$

In this study the Reynolds-averaged Navier-Stokes (RANS) equations are used for the simulations of Chapter 4, where three different turbulence models are tested: the standard k-epsilon model, the Kato-Launder standard k-epsilon model [164], and the low-Reynolds k-epsilon model. Gorji, et al. [165] summarized the model constants, the damping functions and near wall correction functions. The general form of the k-epsilon model with the Boussinesq hypothesis for the swirl turbulent viscosity can be written as:

$$\frac{\partial}{\partial x_j}(\rho\, k\, u_i) = \frac{\partial}{\partial x_j}\left[\left(\mu + \frac{\mu_t}{\sigma_\kappa}\right)\frac{\partial k}{\partial x_j}\right] + G_k + G_b - \rho\,\varepsilon - D \tag{4-15}$$

$$\frac{\partial}{\partial x_j}(\rho\,\varepsilon\, u_j) = \frac{\partial}{\partial x_j}\left[\left(\mu + \frac{\mu_t}{\sigma_\varepsilon}\right)\frac{\partial\varepsilon}{\partial x_j}\right] + C_{1\varepsilon}\,f_1\,\frac{\varepsilon}{k}\,G_kG_b - C_{2\varepsilon}\,f_2\,\rho\,\frac{\varepsilon^2}{k} + E \tag{4-16}$$

Where k is the turbulence kinetic energy, ε is the dissipation rate, μ_t is the turbulent viscosity, σ_κ, $C_{1\varepsilon}$, $C_{2\varepsilon}$, f_1, f_2 are models constants, G_k is the turbulence kinetic energy production due to mean velocity fluctuations and described as $G_k = -\rho\,\overline{u_i'\,u_j'\frac{\partial u_j}{\partial x_i}}$, u_i' is the velocity fluctuations, G_b is the generation of turbulence

kinetic energy due to buoyancy and E are near wall correction functions for k and epsilon equations, respectively.

With a non-gravity and temperature gradient in a k-epsilon model, the k generation due to G_b for ideal gases is defined as:

$$G_b = -g_i \frac{\mu_t}{\rho \, Pr_t} \frac{\partial \rho}{\partial x_i} \qquad \textbf{(4-17)}$$

Where Pr_t is the turbulent Prandtl number,

For the standard k-epsilon model [166], $G_k = \mu_t \, S^2$, the turbulent viscosity is $\mu_t = \rho \, C_\mu \frac{k^2}{\varepsilon}$, $C_{1\varepsilon}=1.44$, $C_{2\varepsilon}=1.92$, D=E=0, $f_1=f_2=1$, and the rate-of-strain tensor, $S=\sqrt{2\,S_{ij}\,S_{ij}}$, is given by:

$$S_{ij} = \frac{1}{2}\left(\frac{\partial u_j}{\partial x_i} + \frac{\partial u_i}{\partial x_j}\right) \qquad \textbf{(4-18)}$$

For the Kato-Launder model, $G_k = \mu_t \, S \, \Omega$, $C_{1\varepsilon}=1.44$, $C_{2\varepsilon}=1.92$, $C_\mu=0.09$, D=E=0, $f_1=f_2=1$, $\mu_t = \rho \, C_\mu \frac{k^2}{\varepsilon}$, the vorticity rate is $\Omega=\sqrt{2\,\Omega_{ij}\,\Omega_{ij}}$ and the vorticity tensor is given by :

$$\Omega_{ij} = \frac{1}{2}\left(\frac{\partial u_i}{\partial x_j} - \frac{\partial u_j}{\partial x_i}\right) \qquad \textbf{(4-19)}$$

In the Yang and Shih low-Reynolds k-epsilon model [165]: the turbulent viscosity is $\mu_t = \rho \, f_\mu \, C_\mu \frac{k^2}{\varepsilon}$, $C_\mu=0.09$, $C_{\varepsilon1}=1.45$, $C_{\varepsilon2}=1.92$, $\sigma_K=1.0$ and $\sigma_\varepsilon=1.3$, $f_1=\frac{\sqrt{Re_t}}{1+\sqrt{Re_t}}$, $f_2=\frac{\sqrt{Re_t}}{1+\sqrt{Re_t}}$ where $Re_t=\frac{k^2}{v \cdot \varepsilon}$, and D=0, $E = v \cdot v_t \cdot \left(\frac{\partial^2 U}{\partial y^2}\right)^2$. The damping function is $f_\mu = \left[1\text{-}\exp\left(\text{-}1.5 \cdot 10^{-4} \cdot Re_y \text{-} 5.0 \cdot 10^{-7} \cdot Re_y^3 \text{-} 1.0 \cdot 10^{-10} \cdot Re_y^5\right)\right]^{0.5} / \left(1+\frac{1}{\sqrt{Re_t}}\right)$, where the turbulent Reynolds number is $Re_y=\frac{y\,k^{1/2}}{v}$, where $y^*=v^{-3/4}\,\varepsilon^{1/4}\,y$.

4.2.2 Filtered Navier-Stokes equations

The finite-volume discretization implicitly provides filtering on every solved quantity φ, by:

$$\bar{\varphi}(x) = \frac{1}{V} \int_V \varphi(x')dx', \quad x' \in v \tag{4-20}$$

where, V is the volume of the computational cell and x' stands for every coordinate direction i,j,k, corresponding to (x,y,z), respectively.

The filter function, G(x) applied is then:

$$G(x,x') = \begin{cases} \frac{1}{V}, & x' \in V \\ 0, & x' \text{ otherwise} \end{cases} \tag{4-21}$$

By filtering the continuity and the Navier-Stokes equations, we get:

$$\frac{\partial \rho}{\partial t} + \frac{\partial}{\partial x_i}(\rho \bar{u}_i) = 0 \tag{4-22}$$

and

$$\frac{\partial}{\partial t}(\rho \bar{u}_i) + \frac{\partial}{\partial x_j}(\rho \bar{u}_i \bar{u}_j) = \frac{\partial}{\partial x_j}(\sigma_{ij}) - \frac{\partial \bar{p}}{\partial x_i} - \frac{\partial \tau_{ij}}{\partial x_j} + \rho g_i \tag{4-23}$$

where, t is the time, ρ is the density, $\bar{u}_i$ is the filtered velocity in the i direction , $\bar{p}$ is the filtered static pressure, g is the acceleration of gravity and σ_{ij} is the stress tensor due to the molecular viscosity, defined by

$$\sigma_{ij} = \left[\mu \left(\frac{\partial \bar{u}_i}{\partial x_j} + \frac{\partial \bar{u}_j}{\partial x_i} \right) \right] - \frac{2}{3} \mu \frac{\partial \bar{u}_i}{\partial x_i} \delta_{ij} \tag{4-24}$$

And the τ_{ij} is the subgrid-scale stress defined by:

$$\tau_{ij} = \rho \overline{u_i u_j} - \rho \bar{u}_i \bar{u}_j \tag{4-25}$$

Subgrid -Scale Models

The subgrid-scale stresses τ_{ij} are requiring modelling and the Boussinesq hypothesis is applied in order to be computed.

$$\tau_{ij} - \frac{1}{3} \tau_{kk} \delta_{ij} - 2 \mu_t \bar{S}_{ij} \tag{4-26}$$

μ_t is the subgrid-scale turbulent viscosity, the $\bar{S}_{ij}$ is the rate-of-strain tensor as defined in equation (4-18) and τ_{kk} is the isotropic part of the subgrid-scale stresses and it is added to the filtered static pressure term.

For compressible flows, the Favre filtered operation is defined:

$$\tilde{\varphi} = \frac{\overline{\rho\,\varphi}}{\bar{\rho}}$$ (4-27)

The Favre-Filter equation for the subgrid tensor is written as:

$$\tau_{ij} = \bar{\rho}\,\widetilde{u_i u_j} - \bar{\rho}\,\tilde{u}_i\,\tilde{u}_j$$ (4-28)

which can be split into two parts, the deviatoric part: $\tau_{ij} - \frac{1}{3}\tau_{kk}\delta_{ij}$ and the isotropic part: $\frac{1}{3}\tau_{kk}\delta_{ij}$.

$$\tau_{ij} = \tau_{ij} - \frac{1}{3}\tau_{kk}\delta_{ij} + \frac{1}{3}\tau_{kk}\delta_{ij}$$ (4-29)

The deviatoric part is modelled with the compressible form of the Smagorinsky model:

$$\tau_{ij} - \frac{1}{3}\tau_{kk}\delta_{ij} = 2\,\mu_t\,(S_{ij} - \frac{1}{3}S_{kk}\delta_{ij})$$ (4-30)

The isotropic part of the subgrid-scale stresses τ_{kk} is not modeled, but is added at the filtered static pressure term.

The subgrid-scale turbulent flux of a scalar, φ, can be defined by the subgrid-scale of turbulent Prandtl number as:

$$q_j = \frac{\mu_t}{\sigma_t}\frac{\partial\varphi}{\partial x_j}$$ (4-31)

where q_j is the subgrid-scale flux.

The constant Smagorinsky-Lilly model [167] is used here, where the eddy-viscosity μ_t is modeled by

$$\mu_t = \rho \, L_s^2 \, |\bar{S}|$$

<div align="right">(4-32)</div>

where L_s is the mixing length for sub-grid scales $|\bar{S}| = \sqrt{2\,\bar{S}_{ij} \cdot \bar{S}_{ij}}$ and $L_s = \min(\kappa d, C_s \Delta)$, with $\kappa = 0.4$ the von Karman constant, d the distance to the closest wall, C_s kept constant at 0.17 , Δ the local grid scale and $\Delta = V^{1/3}$ is computed according to the volume of the computational cell.

The Favre-filtered energy equation takes the form:

$$\frac{\partial}{\partial t}\bar{\rho}\tilde{E} + \frac{\partial}{\partial x_i}\left[(\bar{\rho}\tilde{E} + \bar{p})\tilde{u}_j + \tilde{q}_j - \tilde{\sigma}_{ij}\tilde{u}_i\right] = -\frac{\partial}{\partial x_j}\left(\gamma C_v Q_j + \frac{1}{2}J_j - D_j\right)$$

<div align="right">(4-33)</div>

The SGS turbulent diffusion $\partial J_j/\partial x_j$ is defined as :

$$J_i = \bar{\rho}\left(\widetilde{u_j u_k u_k} - \tilde{u}_j \widetilde{u_k u_k}\right)$$

<div align="right">(4-34)</div>

The SGS viscous diffusion $\partial D_j/\partial x_j$ is defined as :

$$D_i = \bar{\rho}\left(\widetilde{u_j u_k u_k} - \tilde{u}_j \widetilde{u_k u_k}\right)$$

<div align="right">(4-35)</div>

The SGS heat flux Q_j is defined as :

$$Q_j = \bar{\rho}\left(\widetilde{u_j T} - \tilde{u}_j \tilde{T}\right)$$

<div align="right">(4-36)</div>

4.3 Species Transport Equations

The species transport equation of a contaminant concentration is expressed by:

$$\frac{\partial}{\partial t}(\rho\, Y_i) + \frac{\partial}{\partial x_i}(\rho\, u_i\, Y_i) = \frac{\partial}{\partial x_i}(J_i) + S$$

<div align="right">(4-37)</div>

where Y_i is the local mass fraction of each species, J_i is the diffusion flux of species i, and S is any source term inside the flow field.

The diffusion flux of species i due to concentration and temperature gradient for turbulent flows could be expressed as:

$$J_i = -\left(\rho \; D_{i,m} + \frac{\mu_t}{Sc_t}\right) \frac{\partial \; Y_i}{\partial x_i} - \frac{D_{T,i}}{T} \frac{\partial T}{\partial x_i} \qquad \textbf{(4-38)}$$

where, $D_{i,m}$ is the diffusion coefficient for species in the mixture, μ_t is the turbulent viscosity and Sc_t is the turbulent Schmidt number, an empirical number which may vary in general between 0.2-1.3 and plays an important role for the calculation [49]. In the present simulations the turbulent Schmidt number is kept constant at 0.7.

The filtered mass fraction equation for species i is written as:

$$\frac{\partial}{\partial t}\left(\bar{\rho} \; \tilde{Y}_i\right) + \frac{\partial}{\partial x_i}\left(\bar{\rho} \; \tilde{Y}_i \; \tilde{u}_i\right) = -\left(\bar{\rho} \; D_{i,m} + \frac{\mu_t}{Sc_t}\right) \frac{\partial \tilde{Y}_i}{\partial x_i} - \frac{D_{T,i}}{T} \frac{\partial T}{\partial x_i} + S \qquad \textbf{(4-39)}$$

The mean concentration is obtained through the non-dimensional concentration coefficient, K, that is defined as [40, 168]:

$$K = \frac{C_{measured}/C_{source} \cdot U_H \cdot H^2}{Q_{source}} \qquad \textbf{(4-40)}$$

where, $C_{measured}$ is the measured tracer concentration, C_{source} is the source tracer concentration, Q_{source} is the contaminant release rate and U_H is the velocity at the building's height.

CHAPTER 5.   Wind Tunnel experiments coupled with LES simulations

Most of the hazardous release accidents occur near the ground and therefore the study of the wind velocity distribution in different scales of urban geometries is necessary for the determination of the pollutant dispersion both experimentally and numerically.

This Chapter focuses on the understanding of the flow around buildings at different urban geometries performing wind tunnel experiments and numerical simulations using the LES method. The scope of this chapter is to describe the flow mechanisms of turbulence in specific urban geometries.

5.1 Introduction

The airflow around buildings is studied using field and wind tunnel experiments and numerical simulations. The reasons that the field experiments are costly and the flow conditions are not well defined, lead scientists to wind tunnel experiments. Even though, the wind tunnel experiments do not correspond exactly to actual atmospheric flows, this approach is considered adequate to study the airflow around buildings. One of the limitations of the wind tunnel experiments is the lack of the low-frequency turbulence fluctuations, resulting in lower longitudinal and transverse turbulence intensities than in the real-scale experiments. This means that full turbulence spectra is not captured [169]. This limitation also influences the pressure coefficient distribution (Cp) around the scaled buildings.

This chapter presents the study of three experiments (wind tunnel) and their corresponding numerical simulations flow studies (using LES) for the purpose of direct comparison to the extent that is possible. The three different experiments studied are the flow around a cube, the flow in a street canyon and the flow distribution between an array of buildings. The wind tunnel experiments made have scales 1:100 for the 6m cube and array of buildings and 1:570 for the street canyon which has 40m height. The LES numerical simulations were

performed at the same Reynolds number (Re ≈ 36,500) and with similar inlet characteristics as the wind tunnel experiments.

The wind tunnel experiments aim to understand and validate the flow around simplified geometries of different urban scales. The flow is validated with the pressure distribution around these models and with velocity measurements.

5.2 Wind tunnel description

The wind tunnel experiments were conducted in the historical Gottingen type wind tunnel of Prandtl which was built in 1938 and nowadays is installed at the University of West Attica. The wind tunnel is an "8" shaped closed-circuit wind tunnel with two open test sections with elliptic cross section nozzle of major axes 1.0 m x 0.69m and a maximum velocity of 35 m/s.
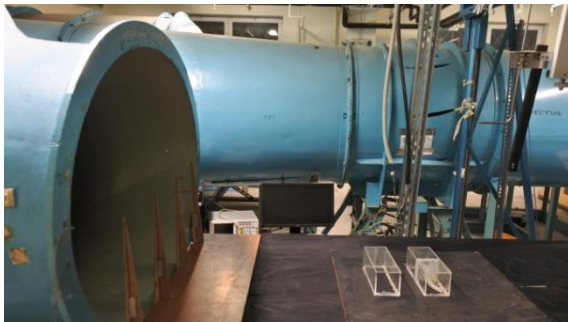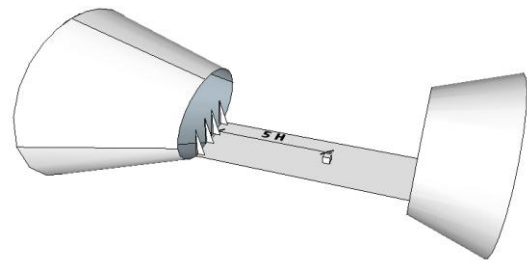
a)   b)

Figure 5-1 Prandtl's original wind tunnel, Gottingen type

In order to generate a thick enough boundary layer for the model studies, that correspond to the atmospheric boundary layer conditions, a wind tunnel with long development length test section is required. In the present study, this boundary layer is generated by four spires shown in Figure 5-1b according to Irwin [170]. The geometrical characteristics of these spires are described in Appendix A.

5.3 Measurements- Instrumentation

A pitot-static tube and hotwire anemometry are used for the velocity measurements. Pressure taps at the model's surfaces are used for the pressure distribution around the scaled buildings. In order to define the mean inlet wind velocity a pitot-static tube is situated around 5H upstream of the models. A constant temperature anemometer (AA Lab Systems AN-1005) with 4 channels of hotwire/film probes of one velocity components are used. The overheat temperature of the anemometer is 250 °C. The sampling rate frequency is 10 kHz. The analog signals are converted to digital signals with an analogue/digital (A/D) converter. The measurements are digitally recorded for 60sec in a PC.

The hot-wires probes: The vertical and horizontal velocity components in the stream-wise measured with an X-wire probe. The mean and fluctuating flow velocities are measured with a dual-sensor TSI 1241-20 X-wire. It a probe for gas applications and it is applied for a 60°C maximum fluid temperature. The probe consists of two wires with 5 μm in diameter and 1.2mm long each. Two X-wire probes are used for the calculation of the u'-w' fluctuations at the x-y cross-sectional plane and for the u'-v' fluctuations at the x-z cross-sectional plane. The turbulent shear stresses u'-v' and u'-w' are defined from these measurements. The X-wire calibration procedure is described in Appendix A.

Micro-manometer: An FCO560 high accurate differential pressure measurement device, with an accuracy of greater than 0.1% of reading at pressures down to 1 Pa is used for the pressure measurements. It has a data-logging facility with USB and RS232C output. Silicon tubes are used in order to connect the pressure taps connections with the micro-manometer.

Temperature: The temperature in the test section is controlled with a National Instrument's 1-channel J type thermocouple measurement device (NI USB-TC01) which includes built-in software. The temperature is recorded in a PC with a USB port and it is real-time monitored. The Recommended warm-up time is 15 minutes and the accuracy is 1.25 °C maximum and 0.6 °C typical.

Traversing system: The accuracy of the probe positions is achieved with a 3D traversing system.

Figure 5-2 Traversing system for the probes positioning into the open test section of the wind tunnel.

Smoke flow visualization: A smoke generator in order to create the instantaneous streamlines formation around the models inside the wind tunnel. The streamlines define the separation, the surface reattachment and the recirculation regions behind the buildings. A smoke-wire flow visualization system for generating smoke (in lab developed) is also used for the flow visualization.

Camera: A Nikon D700 digital camera with a Nikon 180 mm lens was used to capture the smoke streamlines

Surface pressure: In order to define the pressure distribution around the cubical and orthogonal geometries pressure taps are placed on their faces. The pressure distribution is transmitted to the FCO560 high accurate differential pressure micro-manometer with silicon tubes.

5.4 Boundary layer/Atmospheric boundary layer

A pitot-static tube and a hot wire anemometer are used for the measurements of the velocity characteristics at the inlet of the wind tunnel test section. Both are positioned at the centreline of the wind tunnel and 5H upstream of the

model. The measured mean velocity profile at the inlet of the wind tunnel test section with a pitot-static tube is shown in Figure 5-3.
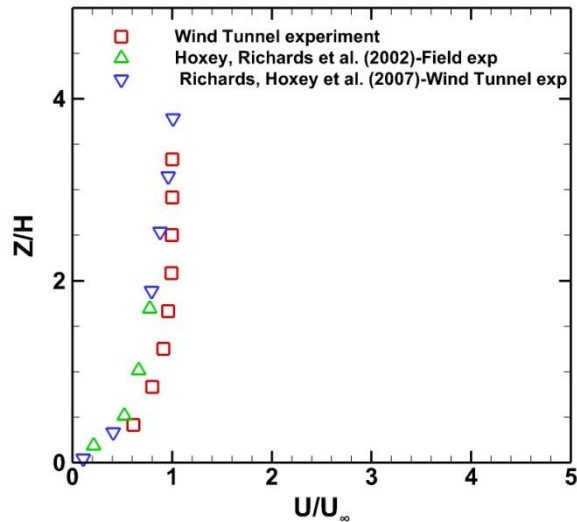
Figure 5-3 Normalized mean velocity profile at the tunnel's test section inlet

The boundary layer thickness, δ, formed in the wind tunnel is approximately twice the building's height and its mean velocity distribution follows the equation (5-1) with the mean velocity at the height of 0.06 m is 9.1 m/sec

$$U_z = \frac{u_*}{\kappa} ln\left(\frac{z}{z_0}\right) \tag{5-1}$$

The friction velocity can be calculated knowing the mean velocity at two points in the log-region (U_2-$U_1 = \frac{u_*}{\kappa} ln\left(\frac{z_2}{z_1}\right)$), which yields u_*=1.034 m/sec. The constant κ is the von Karman constant, with value 0.43. The z_0 defines the roughness height of the flat plate on which the model is placed and the flow is assumed to be neutrally stable. Measurements also of mean velocity at two points within the logarithmic layer define the average roughness height to be z_0=0.00268. The wind tunnel test section is open, so the streamwise pressure gradient is zero.

5.5 Turbulence Intensities

For the experiments performed, the free stream velocity is U_∞=10.5 m/sec. The velocity fluctuations in the three coordinate directions are measured with an X-

film probe, using the interpretation procedure of the anemometer output voltages into the corresponding velocity components proposed by Lekakis [171] in Appendix A. When the x-plane of the two sensors is in the x-z coordinate plane measures the u and w fluctuations and in the x-y plane measures the u,v fluctuations.

The turbulence intensities and the intensity of turbulent kinetic energy are defined respectively below $\frac{u_{rms}}{U_\infty}, \frac{v_{rms}}{U_\infty}, \frac{w_{rms}}{U_\infty}$ and $\frac{1}{U_\infty}\sqrt{\frac{\overline{u_{rms}^2} + \overline{v_{rms}^2} + \overline{w_{rms}^2}}{3}}$ where $u_{rms}, v_{rms}, w_{rms}$ are the rms of the fluctuating velocities in the three directions and U_∞ is the streamwise velocity at the same stream. As shown in Figure 5-4, the longitudinal turbulence intensity at the free stream is 10% and at the building's height is 20%.
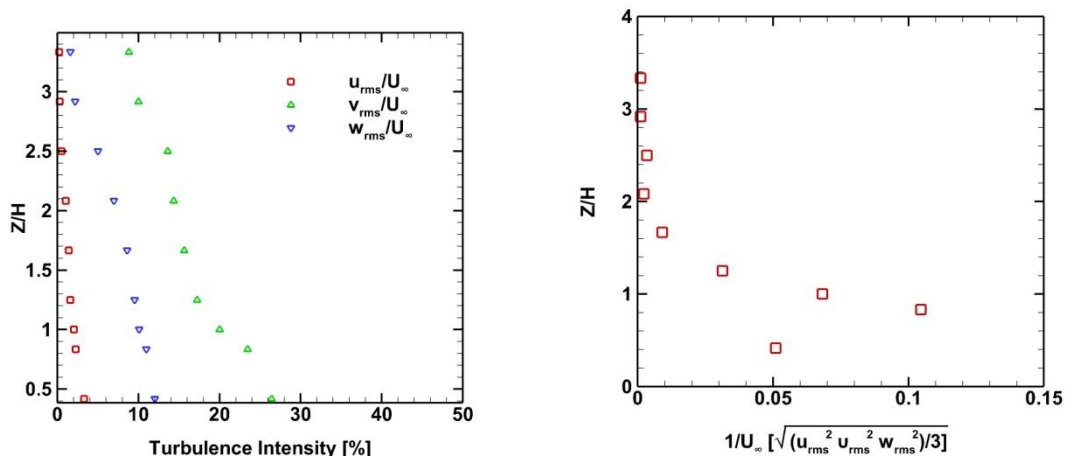
Figure 5-4 Turbulence intensity for a) the three velocity components and b) of the kinetic energy fluctuations.

The streamwise velocity power spectra density normalized with the corresponding root-mean-square (rms) velocity squared, both for the wind tunnel measurements and the LES simulations, are shown in Figure 5-5. The power spectra densities of the streamwise velocity, S_{uu}, is calculated as the square of the Fast Fourier Transform of the streamwise velocity fluctuations time series. The Kolmogorov −5/3 (non-weighted representation) is shown by the straight line in Figure 5-5. The wind tunnel experiments match those of LES

at those frequencies which this method resolves and differ in the inertial subrange.
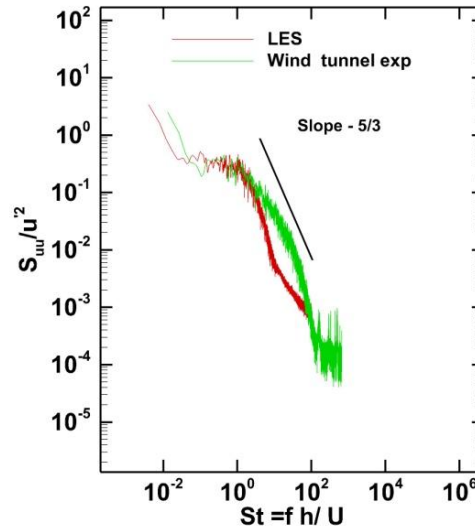
Figure 5-5 Power spectra density of the streamwise velocity fluctuations in the wind tunnel test section and the corresponding LES results.

5.6 Numerical Methods

LES simulations based on the Smagorinsky-Lilly Model, the details of which are given in chapter 4.2.2 were applied to the wind tunnel experiments. For the case of the isolated cube a grid with 2,648,748 cells is used, for the case of the street canyon a grid with 2,719,843 cells is used and for the case of SILSOE cube arrangement a grid with 3,486,725 cells is used.

The computational fluid dynamics (CFD) Ansys Fluent 17 solver is used for the flow simulation. The PISO scheme for the pressure correction and convection equation is used. The second order non-linear terms are calculated with a second order upwind discretization scheme. A second order scheme is, also, used to calculate the pressure at each cell face, the turbulent kinetic energy, and turbulent dissipation rate. The convergence criteria are kept less than 10^{-5} based on the absolute error of all quantities. For the unsteady simulations, a time step of 0.005 sec is used. In order to initialize the case, a steady state simulation was performed with the application of a k-epsilon RANS model.

5.7 Flow around a Cube

5.7.1 Experimental distribution of mean pressure coefficient

The flow and the pressure distribution around a 6cm cube made of plexiglas is studied, when the upwind face of the cube is perpendicular to the wind tunnel mean flow direction. Two different experiments are performed with cubes of the same height but with the pressure taps differently distributed on their faces. The first cube has 33 pressure taps that are positioned at the centre line of the windward face, roof and, leeward face of the cube as shown in Figure 5-6a, where the pressure taps are 0.5 mm apart. In the second cube, as shown in Figure 5-6b, the pressure taps are arranged uniformly in the form of a grid on the windward face, roof and leeward faces of the cube in order to measure the pressure distribution (with 16 pressure tap on each face)

a)   b)   c)
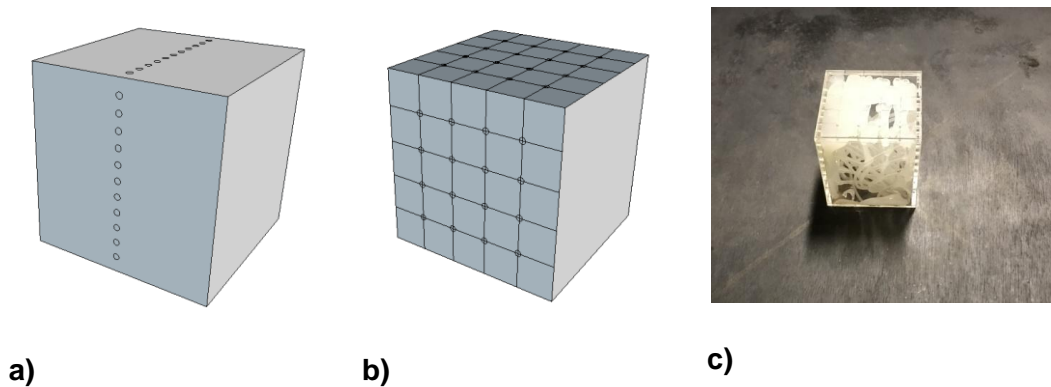
Figure 5-6 Pressure distribution a) along the intersection line of the cube's surface and the symmetry plane, b) on different cube faces; c) photo of cube in the wind tunnel.

The pressure taps are sampled with the frequency of 10Hz and the pressure coefficient is defined by the equation below :

$$C_p = \frac{p - p_\infty}{\frac{1}{2}\rho_\infty U_\infty^2} \tag{5-2}$$

where, p is the static pressure, p_∞ is the static pressure in the free-stream, U_∞ is the free-stream velocity and ρ_∞ is the free-stream fluid density.

The distribution of the mean pressure along the symmetry line on the cube surfaces is shown in Figure 5-7 against the wind tunnel experiments of Castro, et al. [18], Richards, et al. [169] and the field experiments of Hoxey, et al. [172]. The present wind tunnel experiments have close longitudinal turbulence intensities with Richards, et al. [173] field experiments.

Castro, et al. [18] measured the pressure coefficient distribution around cubes for a boundary layer thickness to cube height ratios with δ/H=1.063, 2.127, 10. Their study also showed that when the boundary layer thickness to cube height ratio is higher than δ/H =1.4 the shear layer is separated at the leading edge of the cube and reattaches on the roof of the cube. As the ratio δ/H is increasing the reattachment point is moving towards the leeward edge of the cube. It is also found that when δ/H is lower than 1.4 the reattachment is intermittent.

Richards, et al. [169] contacted wind tunnel experiments for the flow around a cube with a boundary layer thickness that is up to twice the height of the cube and for a roughness height 0.42mm, the pressure coefficient measurements are shown in Figure 5-7. These wind tunnel experimental data are in close agreement with Hoxey, et al. [172] field experimental data. The small differences in the turbulence inlet between the present wind tunnel experiments and the LES simulations influence the pressure distribution on the cube.
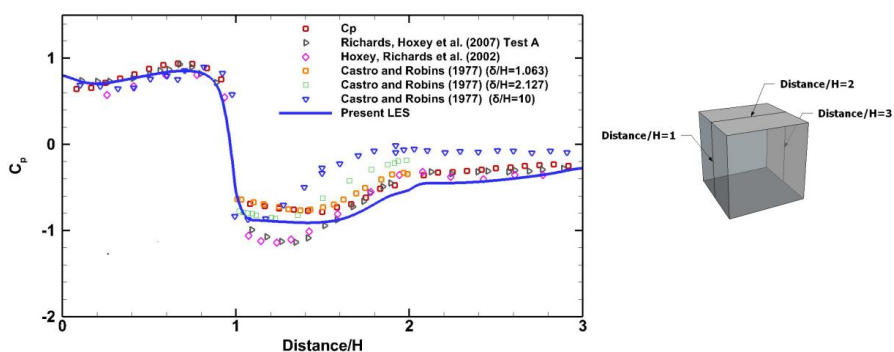
Figure 5-7 Mean pressure coefficient distribution along the symmetry line of the flow around a cube

The pressure distribution on the windward face of the cube is similar for all the wind tunnel and field's experimental data. Essential differences exist on the roof

of the cube between the field and the wind tunnel experimental data. These differences are due to the inlet velocity distribution. Richards, et al. [169] and Hoxey, et al. [172] results, show more negative values for a distance of one cube height downstream of the leeward face of the cube. The present experimental data for the static pressure on the roof of the cube are almost identical to the Castro, et al. [18] experimental data for the case when δ/H=1.063, where δ is the boundary layer thickness.

Figure 5-8 shows the comparison of the pressure coefficient distribution on the windward cube face between the experimental and the LES method. The results are in a good agreement, even though the presented differences on the contour graphs are due to the number of pressure taps on the cube's surfaces.
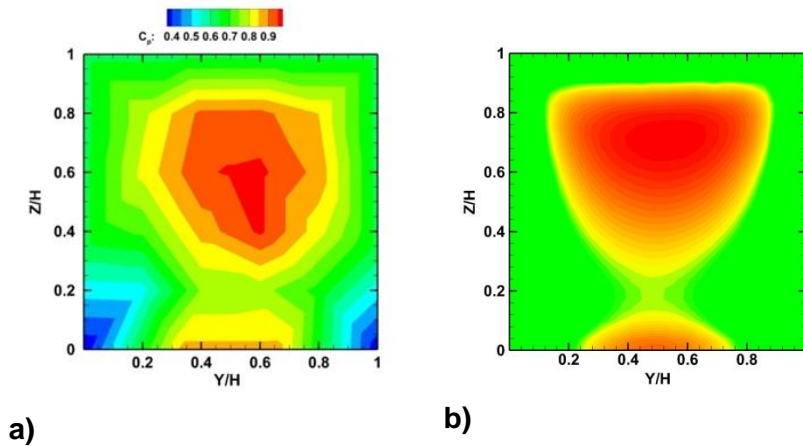
Figure 5-8 Comparison of the pressure coefficient on the windward cube face from a) the experiments and b) the corresponding LES

5.7.2 Velocity distribution around the cube based on LES

The reattachment position on the roof of the cube depends on the turbulence level at the inlet of the test section. The boundary layer thickness for the wind tunnel experiment is almost twice the height of the cube, which is above the critical ratio value of 1.4 where the shear layer detaches at the front roof corner of the cube and reattaches on the roof surface [18].

In Figure 5-9, which shows smoke visualization experiments, the shear layer indeed reattaches on the roof surface of the cube and at a distance from the

front corner 0.74H, where H is the cube's height. It also shows that the length of the recirculation zone is approximately 1.58H.
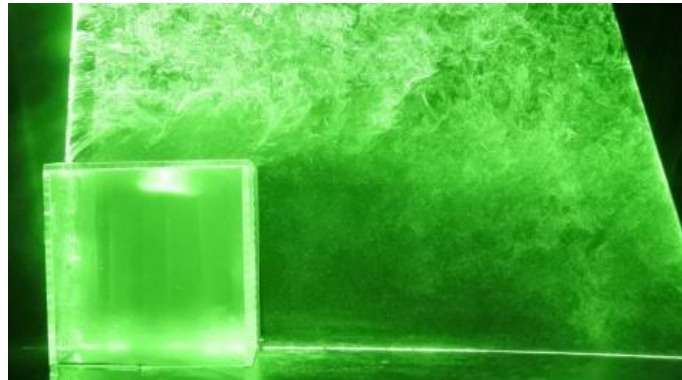
Figure 5-9 Smoke visualization of the flow around the cube

In order to find the reattachment point behind the cube, the method of Antoniou and Bergeles was applied [174, 175]. The X-film probe was position 6H away from the centre line of the cube and at a 0.03 H height, and it was moved towards the leeward face of the cube to the position where the velocity is minimum, marking the reattachment position. This is found to be 1.46 H behind the cube, which is in good agreement with other experimental data [20, 172].

As shown in Figure 5-10a, the streamwise normal stress $\overline{u'^2}/U_\infty^2$ has the highest values above the roof of the cube where the shear layer separates and then reattaches. Large values exist near the ground of the upwind area of the cube where the horseshoe vortex is formed. Figure 5-10b shows that the transverse stress $\overline{w'^2}/U_\infty^2$ show high values at the trailing edge of the cube, where the shear layer formed on the roof of the cube interacts with the recirculating flow behind it. Finally, Figure 5-10c shows the spanwise stress $\overline{v'^2}/U_\infty^2$ with similar characteristics as the transverse stress. All normal stresses show high values in the horseshoe vortex region near the upwind wall of the cube.

a)

b)

c)

Figure 5-10 Normalized normal stresses at the symmetry plane for a) the streamwise $\overline{u'^2}/\mathrm{U}_\infty^2$, b) the transverse $\overline{w'^2}/\mathrm{U}_\infty^2$, and c) the spanwise $\overline{v'^2}/\mathrm{U}_\infty^2$ stresses

Figure 5-11 shows a 3-dimensional view of the normal stresses in the three coordinate directions. Figure 5-11a shows the streamwise stress where the maximum values are on the lateral sides of the cube and at the horseshoe vortex region. The transverse stress gets maximum values in the middle part of the lateral sides of the cube (Figure 5-11b). Finally, the spanwise normal stress shows high values towards the end of the lateral sides of the cube and at the

area where the roof shear layer meets the rear recirculation zone of the cube (Figure 5-11c).

a)   b)   c)

Figure 5-11 Normalized normal Reynolds stresses in a three-dimensional space for a) the streamwise $\overline{u'^2}/U_\infty^2$, b) the transverse $\overline{w'^2}/U_\infty^2$, and c) the spanwise $\overline{v'^2}/U_\infty^2$ stresses

Figure 5-12 shows the normalized Reynolds stress $\overline{u'v'}/U_\infty^2$ on the symmetry plane where negative shear stress values appear on the horseshoe vortex area.

Yakhot, et al. [176] indicate in their study that in regions where the turbulence stress is negative the flow is not in equilibrium. In these areas the energy is transfered from small to large scales, which is characteristic of anisotropic flows. This phenomenon appears in regions where the flow near walls decelerates ($\partial U/\partial x$ has negative values)
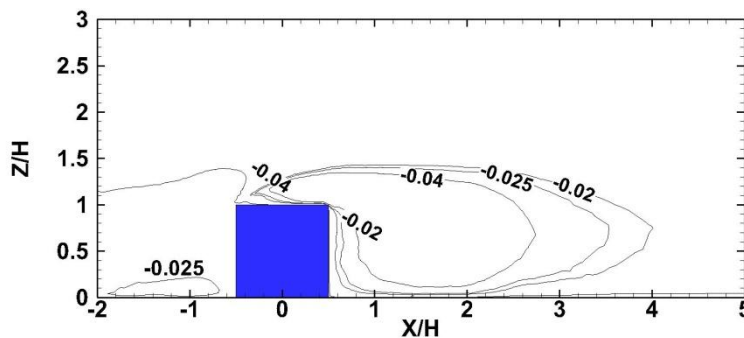
a)
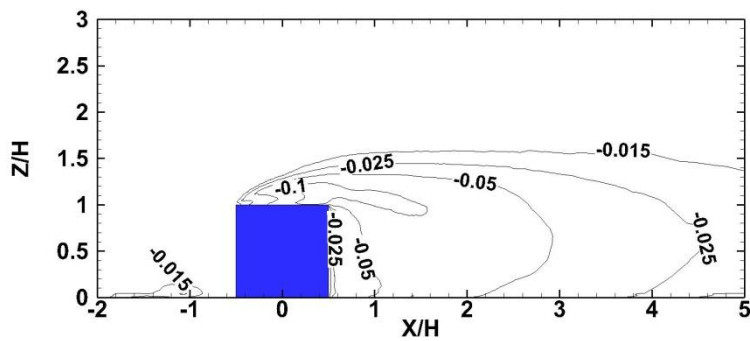
b)

Figure 5-12 Normalized Reynolds stresses a) $\overline{u'v'}/U_\infty^2$ **and b)** $\overline{u'w'}/U_\infty^2$ **on the symmetry plane**

Figure 5-13a shows the $\overline{u'v'}/U_\infty^2$ turbulence shear stress and Figure 5-13b the $\overline{w'v'}/U_\infty^2$ turbulence shear stress on a parallel to the ground plane, placed at a height plane at Z/H=0.08 height. For both stresses, the highest values are shown in the horseshoe vortex area. The $\overline{u'v'}/U_\infty^2$ shear stresses are presented in the spanwise direction, and the $\overline{w'v'}/U_\infty^2$ shear stresses are turning from the spanwise direction to the streamwise direction.
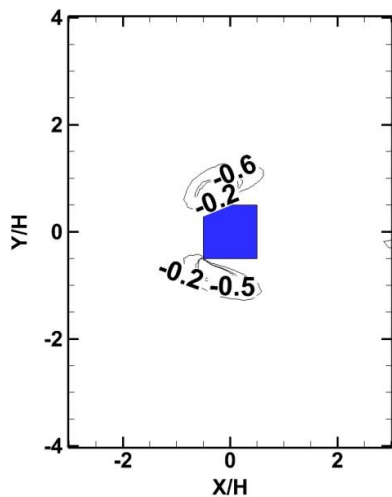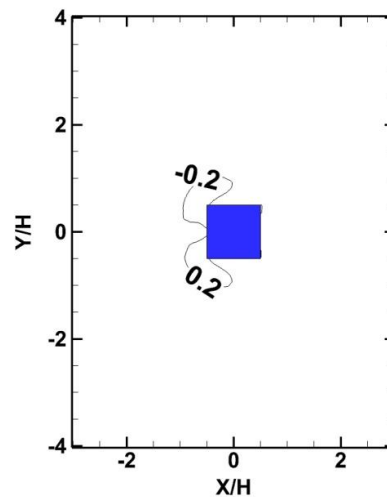
a) **b)**

Figure 5-13 Reynolds stresses on the horizontal plane at Z/H=0.08 for a) $\overline{u'v'}/U_\infty^2$ **and b)** $\overline{w'v'}/U_\infty^2$

77

5.7.3 Unsteady characteristics of the flow from LES

The identification of the coherent structures and the vortices can be made with the iso-surfaces of the Q-criterion. The definition of the Q-criterion is [177]:

$$Q = C_Q \ (\Omega^2 - S^2) \qquad \textbf{(5-3)}$$

where C_Q, is a constant for the impressions with a value 10^{-3}, S is the Strain Rate [equation (4-18)] and Ω is the vorticity rate [equation (4-19)].

The flow around a cube shows areas with significant fluctuations due to the vortices which are created at the cube's edges and transferred to the downstream region. These areas are identified by the vorticity Magnitude (Figure 5-14a) and the Q criteria (Figure 5-14b).

a)   b)
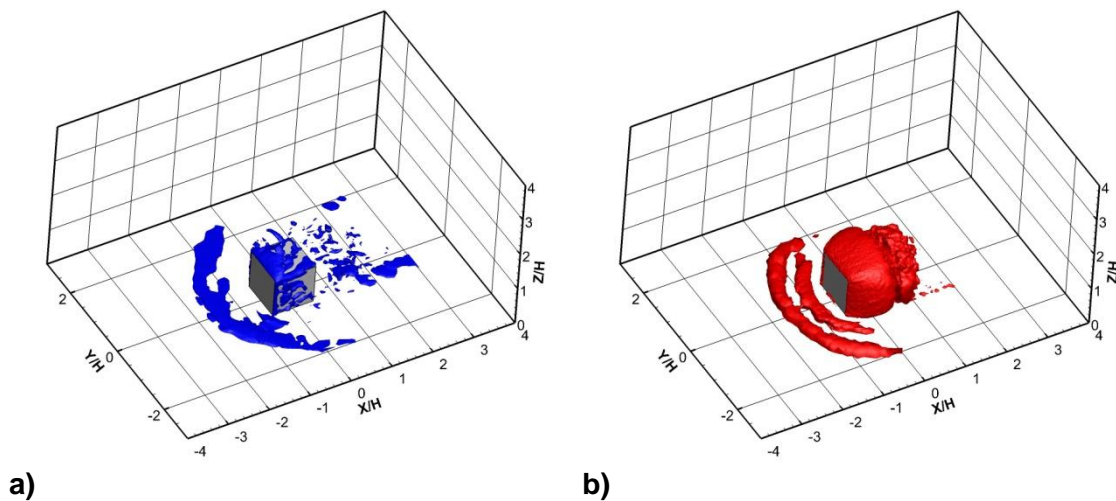
Figure 5-14 Iso-surface of the a) Vorticity Magnitude for a value of 20 $(1/\sec^2)$ **and b) the Q criteria at a constant value** $1/\sec^2$

Figure 5-15a presents the normalized pre-multiplied energy spectra distribution (PSD) of the streamwise velocity fluctuations effectuated with the X-wire anemometer and Figure 5-15b presents the present LES numerical results at a position 2H downstream of the cube and at a 0.5H and 2H height normalized by the velocity at the height of the cube [178]. The spectra space is well behaved with the Kolmogorov's theory with a -2/3 slope at the high frequencies.

The characteristic wavelength of the spectral peak also called as, dominant shedding peak, is presented at frequencies of $St = f H/U_H = 0.12$, this value is similar to the Sattari, et al. [179] and Hussein, et al. [22] experimental data, as well as with the DNS numerical calculations of Schlatter, et al. [180]. The PSD values of the LES results present values that are slightly lower (less energy) than the X-wire experimental data even though the Kolmogorov's length scale was not resolved. The Kolomogorov's length scale for homogenous and isotropic turbulence is defined as $n_K = \left(\frac{v^3}{\bar{\varepsilon}}\right)^{1/4}$, where the turbulence's energy mean dissipation rate is defined as $\bar{\varepsilon} = \overline{\frac{\partial u_i'}{\partial u_j'}\frac{\partial u_i'}{\partial u_j'}}$, is the smallest scale that spatially is resolved. The smaller values of n_K are presented near the wall regions where the $\bar{\varepsilon}$ increases.
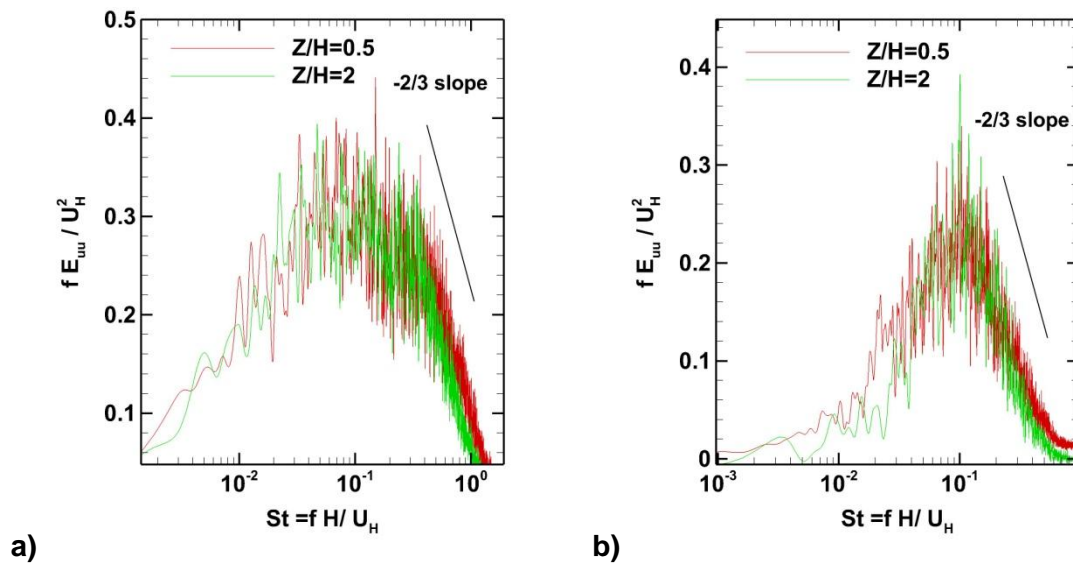
Figure 5-15 Frequency Spectra for the streamwise velocity at a 2H position downstream of the cube at measured a) at the wind tunnel and b) numerically calculated for the positions of 0.5H and 2H height.

5.8 Street canyon Flow

5.8.1 Experimental Pressure distribution

The model street canyon as shown in Figure 5-16, is made of two buildings of 0.07 m height, 0.07 m width and 0.21 m length and with a distance between the two buildings 0.07 m, thus forming a street canyon with aspect ratio H/W=1. On every face of the buildings forming the canyon and at the symmetry plane are positioned 13 pressure taps. The taps have a distance of 4.2 mm. According to Oke [58] this flow is called "skimming flow", as a stable vortex is formed inside the canyon.
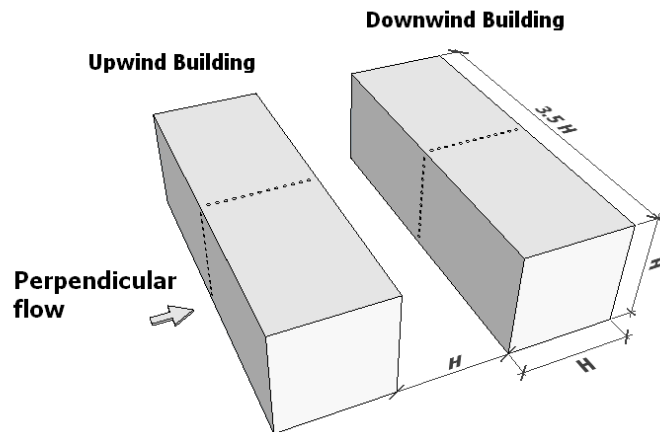
Figure 5-16 Street canyon geometry

The pressure coefficient distribution around the upwind building of the canyon is shown in Figure 5-17. The experimental data are compared also against the numerical data of Pancholy, et al. [181], that used a RANS model to study the flow pattern in a street canyon with objective to define the pedestrian comfort in it. This study employs an atmospheric boundary layer at the inlet of the computational domain (δ/H=45).
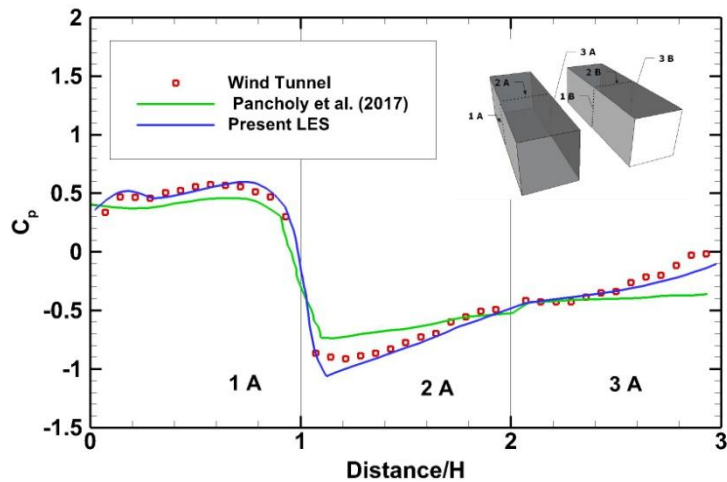
Figure 5-17: Pressure coefficient distribution around the upwind building of the street canyon

From Figure 5-17, it is shown that the maximum value of the pressure coefficient is found at the 0.6 H position of the front face of the upwind building in agreement with the LES results.

5.8.2 Velocity distribution in and around the canyon based on LES

A horseshoe vortex is created at the bottom corner of the windward building. Eddy circulations also formed at the lateral sides of the windward building which are entering inside the street canyon, forming a primary eddy inside the canyon.
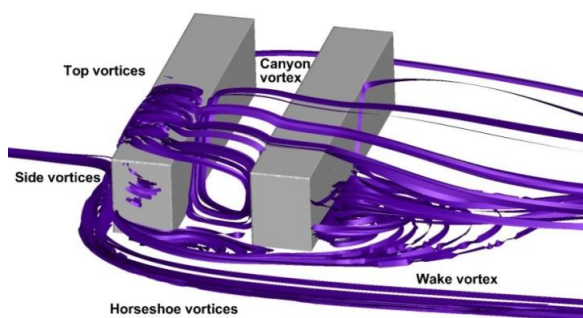
Figure 5-18 Main vortices formed in a street canyon
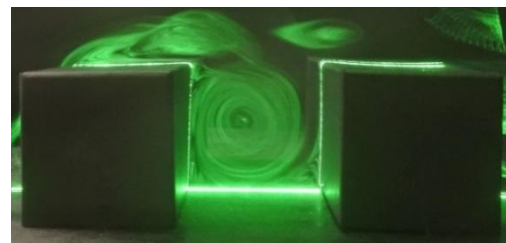
Figure 5-19 Smoke flow visualization in the street canyon.

When the wind is oblique to the street canyon (within $\pm 60^o$) a helical moving vortex appears in the street canyon [67] and not a standing vortex [182]. Nakamura and Oke [16] made similar observations from field experiments.

As shown in Figure 5-20 from the streamlines and the iso-contour lines of the mean velocity U on a horizontal plane which is at a height Z/H=0.01, the flow separates at the sides of the two buildings and part of the separated shear layer on the upwind building is roll up inside the canyon. On the symmetry plane, Figure 5-21, shows that the flow detaches at the leeward building's roof and reattaches on the same roof. This is in agreement with the important negative values of the pressure coefficient (Figure 5-17) near the leading edge on the roof of the upwind building due to the flow separation at this point and the approximately near-zero values due to the flow reattachment near the downstream edge on the same roof [18]. A recirculation zone appears with its centre at the middle of the roof (Figure 5-21). The main flow from the upwind building moves to the downwind building, however part of the flow recirculates inside the street canyon towards the upwind building and re-enters into the main flow.
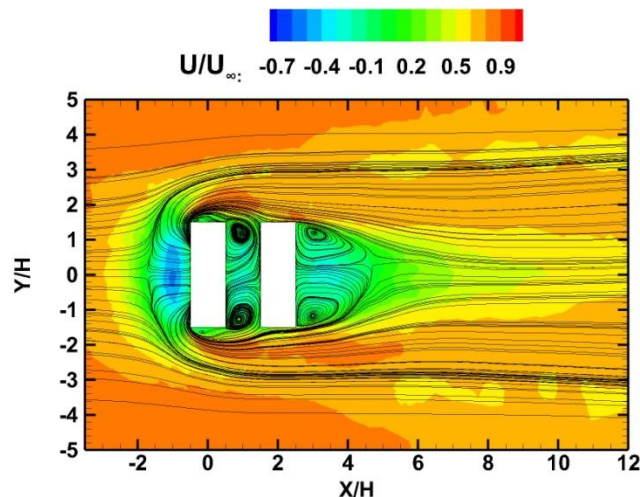
Figure 5-20 Streamlines and iso-contour lines of the normalized mean velocity distribution on a horizontal plane at Z/H=0.01.
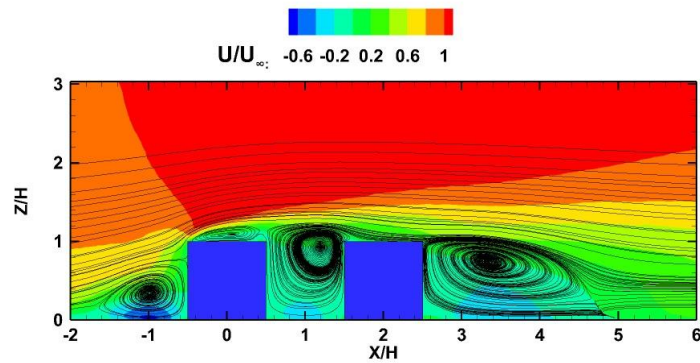
Figure 5-21 Streamlines and iso-contour of the normalized mean velocity distribution on the symmetry plane.

The lengths of the main recirculation regions are: X_f for that in front of upwind building, X_b downstream of the downwind building of the upwind building and X_r for the roof, illustrated in Figure 5-22 and summarized in Table 5-1.
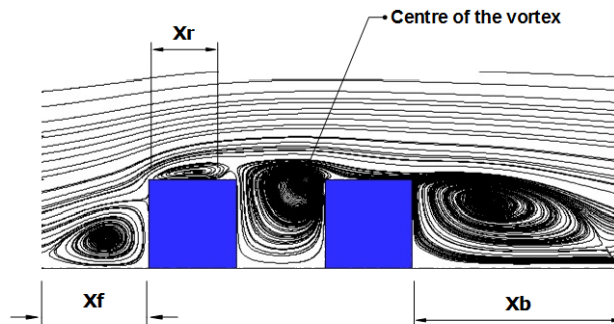
Figure 5-22 Length in a street canyon

Table 5-1 Main separation region lengths

Model	X_f	X_r	X_b	Centre of the vortex
Present LES	0.49 H	0.82 H	2.34 H	X=1.19 H Z=0.91 H

As shown in Figure 5-23a, the normalised streamwise $\overline{u'^2}/U_\infty^2$ normal stresses gets the highest values above the roof of the upwind building where the shear layer separates and then reattaches. High values are also present in front of the upwind building where a horseshoe vortex is formed. All the region above the

83

roof of the upwind building up to the roof of the downwind building and even downstream shows also high values of the streamwise normal stresses. Figure 5-23b shows that the mean transverse stress $\overline{w'^2}/U_\infty^2$ indicates the highest values inside the street canyon near the upstream face of the downwind building. Finally, Figure 5-23c shows the spanwise stresses $\overline{v'^2}/U_\infty^2$ indicating similar characteristics with that of the transverse stresses. All normal stresses have important high values in the horseshoe vortex region in the corner upstream of the upwind building.
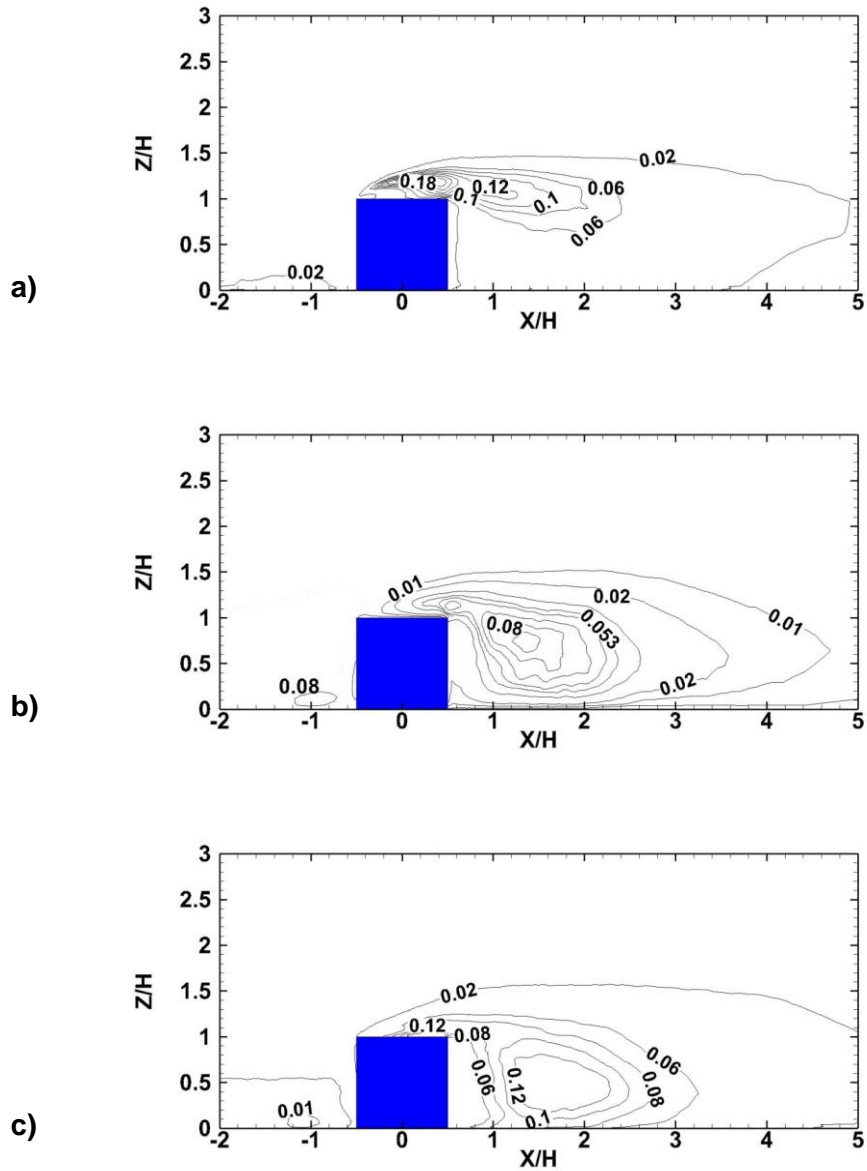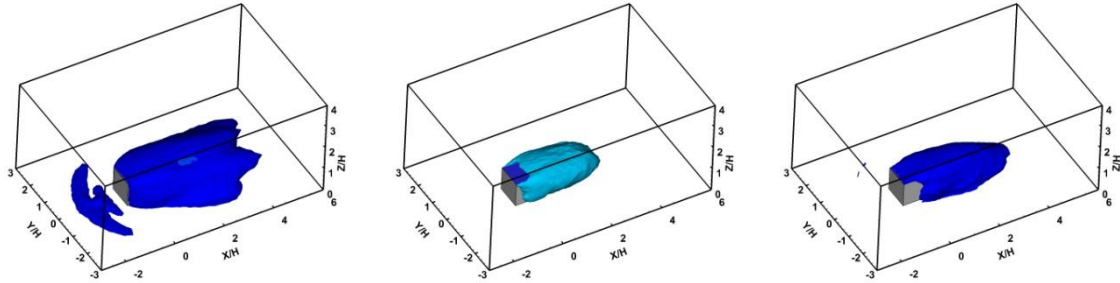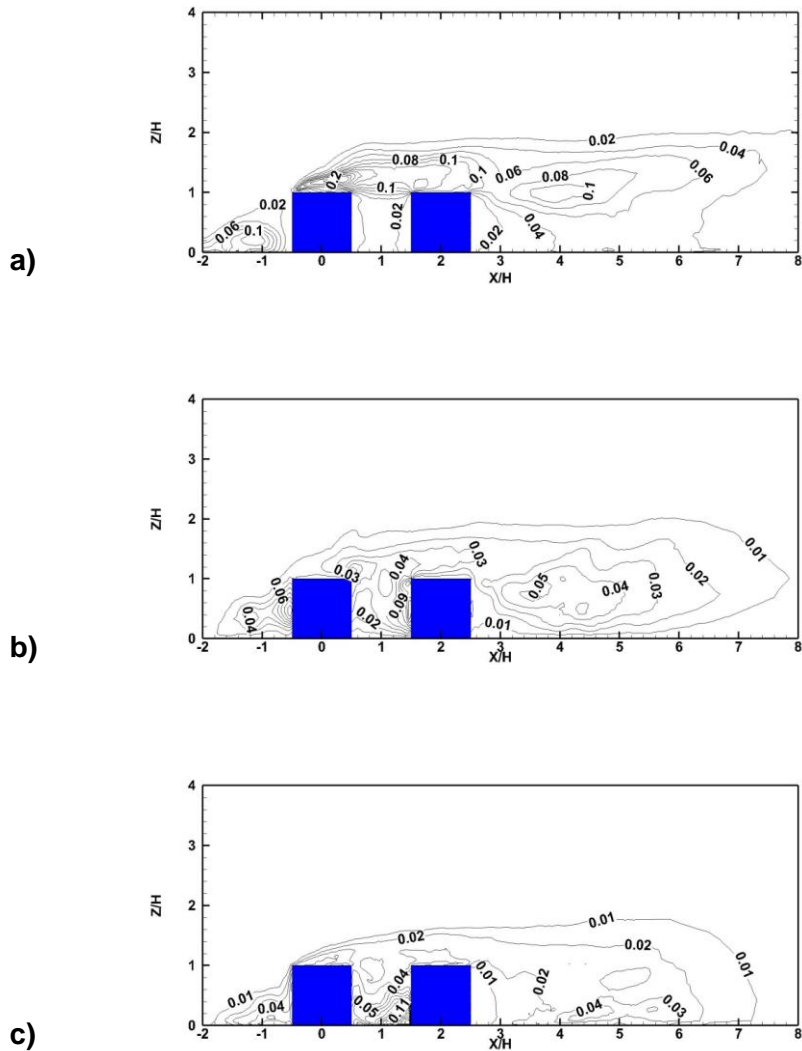

Figure 5-23 Normalized stresses on the symmetry plane for a) the streamwise $\overline{u'^2}/U_\infty^2$, b) the transverse $\overline{w'^2}/U_\infty^2$, and c) the spanwise $\overline{v'^2}/U_\infty^2$ stresses

84

The normalized Reynolds stresses $\overline{u'w'}/U_\infty^2$ on the symmetry plane (Figure 5-24a) shows negative values in the horseshoe vortex area, inside the street canyon cavity and in the wake area of the downwind building. Similar behaviour shows the Reynolds stresses $\overline{u'v'}/U_\infty^2$ on the symmetry plane (Figure 5-24b).

a)

b)
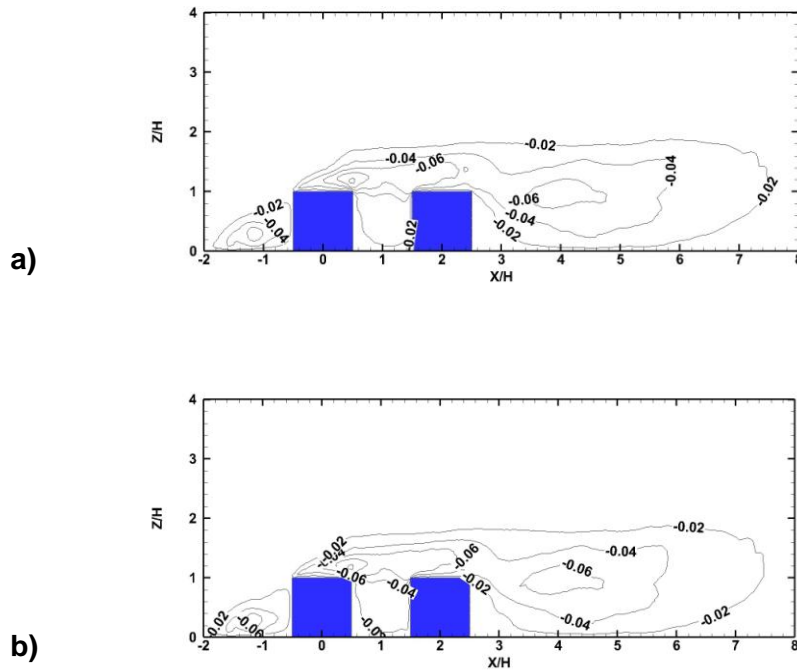
Figure 5-24 Normalized Reynolds stresses on the symmetry plane for a) $\overline{u'w'}/U_\infty^2$**, and b)** $\overline{u'v'}/U_\infty^2$

Figure 5-25a shows the $\overline{u'w'}/U_\infty^2$ turbulence shear stresses and Figure 5-25b the $\overline{v'w'}/U_\infty^2$ turbulence shear stresses on a parallel to the ground plane at a height Z/H=0.08. For both stresses, the highest values exist in the horseshoe vortex area. The $\overline{u'w'}/U_\infty^2$ shear stresses are presented in the spanwise direction and the $\overline{v'w'}/U_\infty^2$ shear stresses are turning towards the spanwise direction. In both cases, elevated values are shown on the arch vortex area where the flow enters through the lateral sides into the canyon.
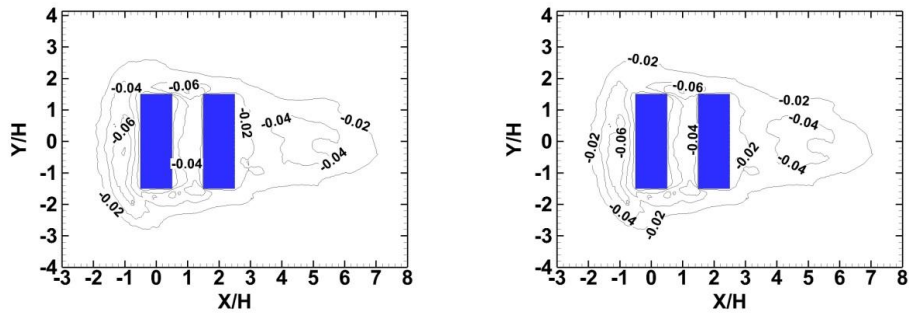
a)   b)

Figure 5-25 Normalized Reynolds stresses on a horizontal plane at a height Z/H=0.08 for a) $\overline{u'w'} / U_\infty^2$ **, and b)** $\overline{v'w'} / U_\infty^2$

5.8.3 Unsteady characteristics of the flow based on LES

The Vorticity Magnitude square and the Q criterion iso-surfaces (Figure 5-26) show the areas of significant vorticity, delineating the vortices created at the building edges and their extension to the downstream region.
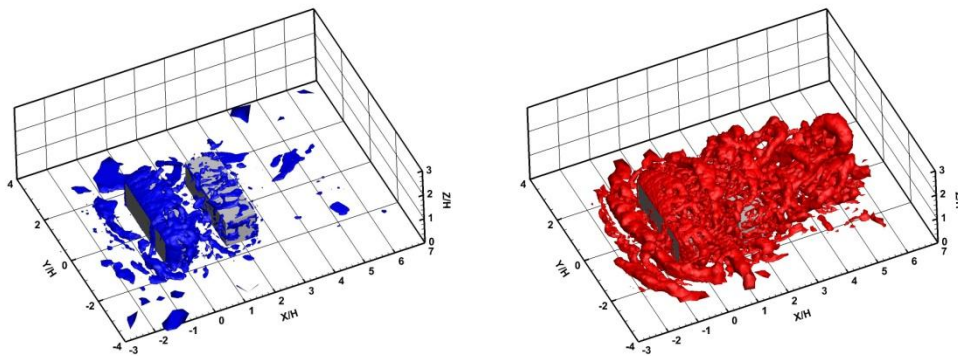
a)   b)

Figure 5-26 Iso surfaces of a) the vorticity magnitude at a constant value 20 $1/\sec^2$ **and b) the Q criteria at a constant value** $1/\sec^2$ **.**

Figure 5-27a and b shows the normalized pre-multiplied energy spectra density of the streamwise and transverse velocity fluctuation measured with the X-wire anemometer and Figure 5-27c and d presents the LES numerical results at the same position for the same velocities. The characteristic wavelength of the

spectral peak is $St = f H / U_H = 0.11$ for the streamwise velocity and 0.06 for the transverse velocity, both concerning the anemometry measurements. The LES method presents a spectra peak at a the value 0.16 for the streamwise velocity and 0.34 for the transverse velocity. The power spectra presents higher level (more energy) in the direction of the streamwise velocity than the transverse velocity.

a)

b)

c)

d)
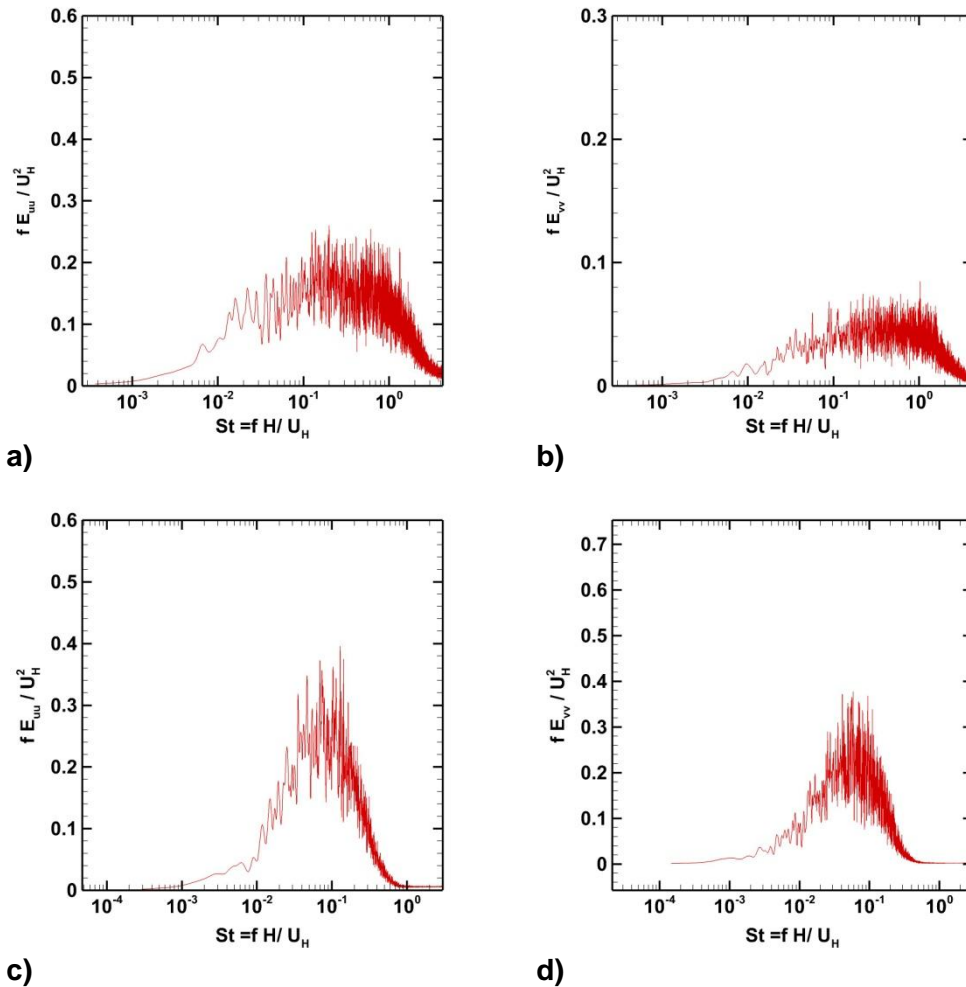
Figure 5-27 Normalized Power Spectra Density for the streamwise velocity at a 2H position downstream of the street canyon and at 2H height for the a) streamwise velocity and b) the transverse velocity for the wind tunnel experiments and c) the streamwise velocity and b) the transverse velocity for the numerical simulations.

5.9 Air flow around an array of buildings

5.9.1 Arrangement of Buildings

A staggered arrangement of cubes, as shown in Figure 5-28a and b is examined in the wind tunnel. This arrangement is exactly the same as the SILSOE arrangement for which field and wind tunnels experiments have been performed [183]. The cubes have a constant height of 0.06 m. The isolated SILSOE cube (Figure 5-28) is the same as the one, carrying the linear 33 pressure taps (Figure 5-6a). The building arrangement consists of 9 buildings in a staggered array and with an area coverage of $\lambda_p=25$ % (equation (2-1)).

a)   b)
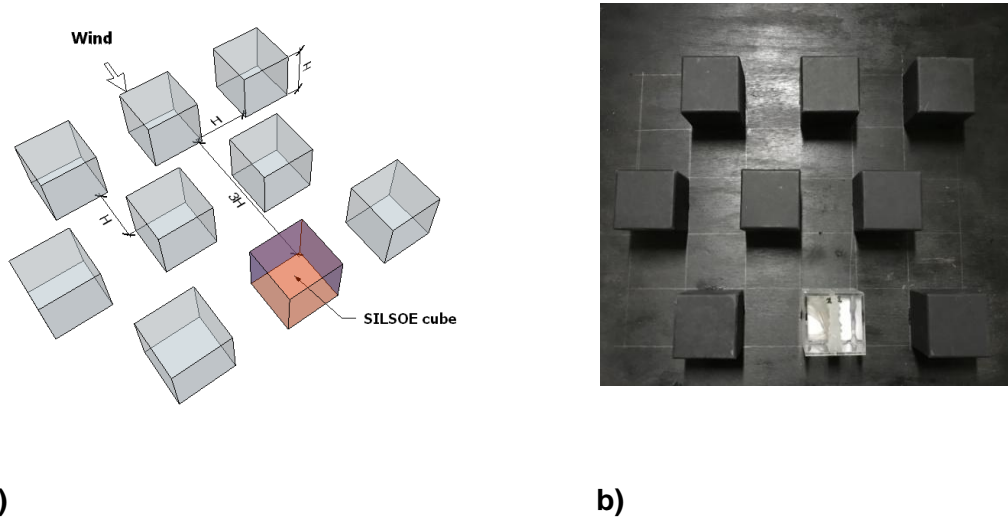
Figure 5-28 Staggered array of cubes a) Sketch and b) photo in the wind tunnel.

5.9.2 Velocity distribution around an array of buildings based on LES

The streamlines and the contour lines of the normalized mean velocity are shown in Figure 5-29 on a horizontal plane placed at a height Z/H=0.01. The wind is accelerated around the outer cubes (B1, D1 and F1) and between the passages B1-D1 and D1-F1. There are separation zones at the sides of all the cubes and recirculation zones with low velocities between the cubes which are arranged asymmetrically. A horseshoe vortex is created at the bottom of the B1, D1 and F1 upwind buildings. The eddy circulations which are formed due to the

shear flow at the lateral sides of these buildings enter in the free space of the array of buildings.
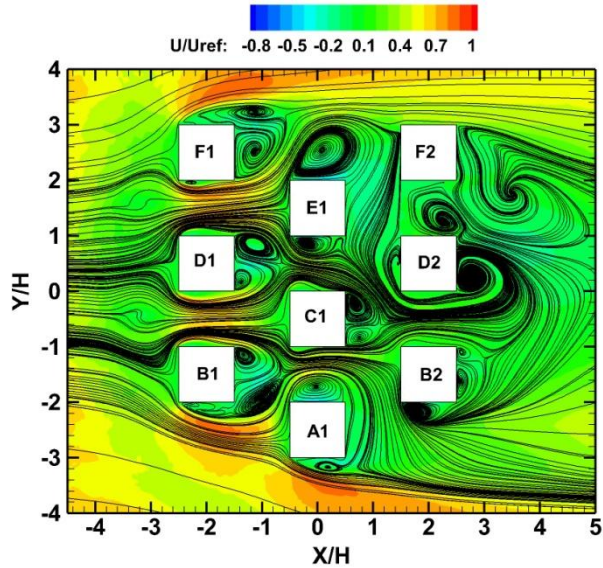
Figure 5-29 Streamlines and the normalized mean velocity distribution U/U_∞ on a horizontal plane at a height Z/H=0.01

Figure 5-30 and Figure 5-31 show the stresses on the vertical plane passing through the centres of D1 and D2 cubes. As shown in Figure 5-30a, the normalized streamwise $\overline{u'^2}/\mathrm{U}_\infty^2$ normal stresses gets the highest values at the area just above the two cubes and in the middle of the two cubes distance. This area is also where the transverse stresses, $\overline{w'^2}/\mathrm{U}_\infty^2$, indicates the highest values (Figure 5-30b). The spanwise stresses, $\overline{v'^2}/\mathrm{U}_\infty^2$, also appears to have the maximum values between these two cubes.

a)

b)

c)
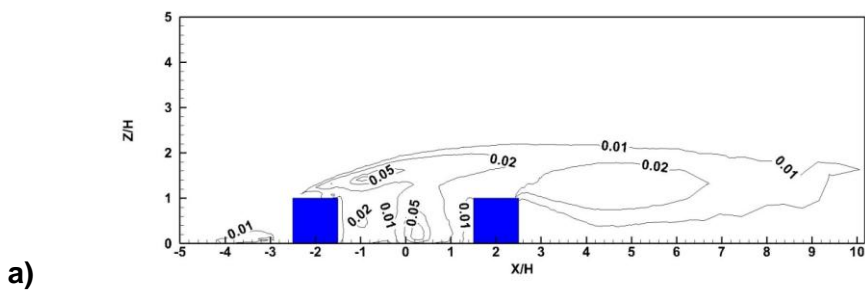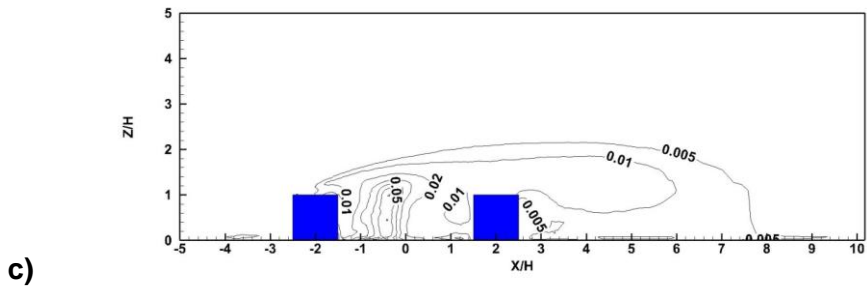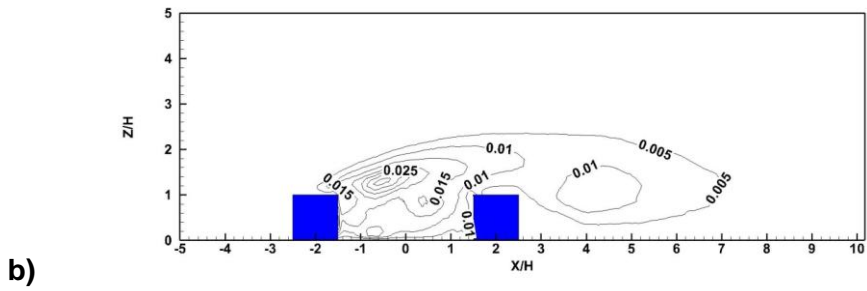
Figure 5-30 Normalized normal stresses on the symmetry plane   a) the streamwise $\overline{u'^2}/U_\infty^2$, b) the transverse $\overline{w'^2}/U_\infty^2$, and c) the spanwise $\overline{v'^2}/U_\infty^2$ stresses

Figure 5-31a shows that the normalized Reynolds stresses $\overline{u'w'}/U_\infty^2$ have almost the same behaviour with the normalized Reynolds stresses $\overline{u'v'}/U_\infty^2$ which is indicated as both give the highest values inside the street canyon cavity.

a)

b)
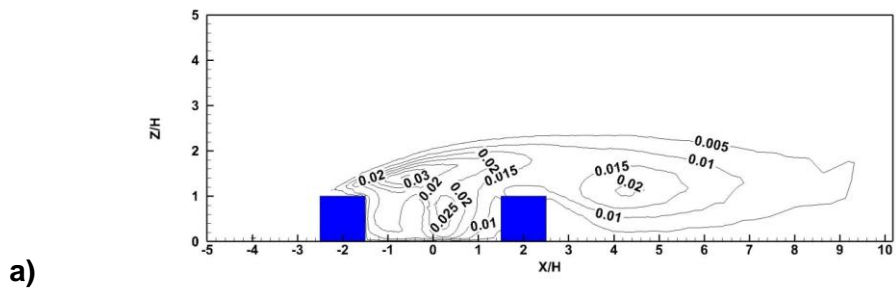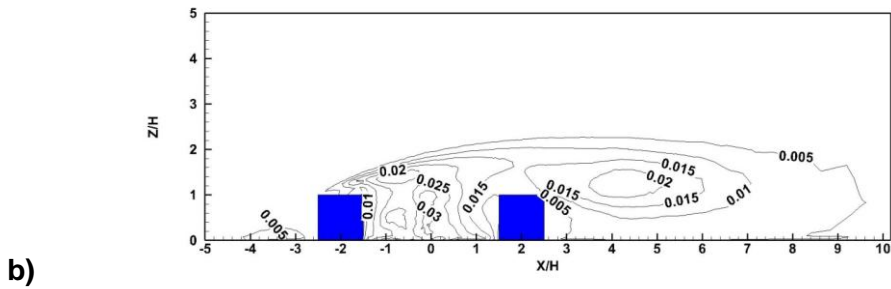
Figure 5-31 Normalized Reynolds stresses on the symmetry plane for a) $\overline{u'w'}/U_\infty^2$

, and b) $\overline{u'v'}/U_\infty^2$

Figure 5-32 shows the non-dimensional Reynolds stresses on a horizontal plane at a height Z/H=0.08. The non-dimensional Reynolds stresses $\overline{u'w'}/U_\infty^2$ and $\overline{u'v'}/U_\infty^2$ give their highest values between the cubes in the array of building and more specifically in the central area between the A1-C1 and C1-E1 cubes. The non-dimensional Reynolds stresses $\overline{u'w'}/U_\infty^2$ give significant values in the horseshoe vortex area, which starts at the corners of front faces of the upwind external cubes (B1-D1-F1) as shown in Figure 5-32a and b.

a)   **b)**
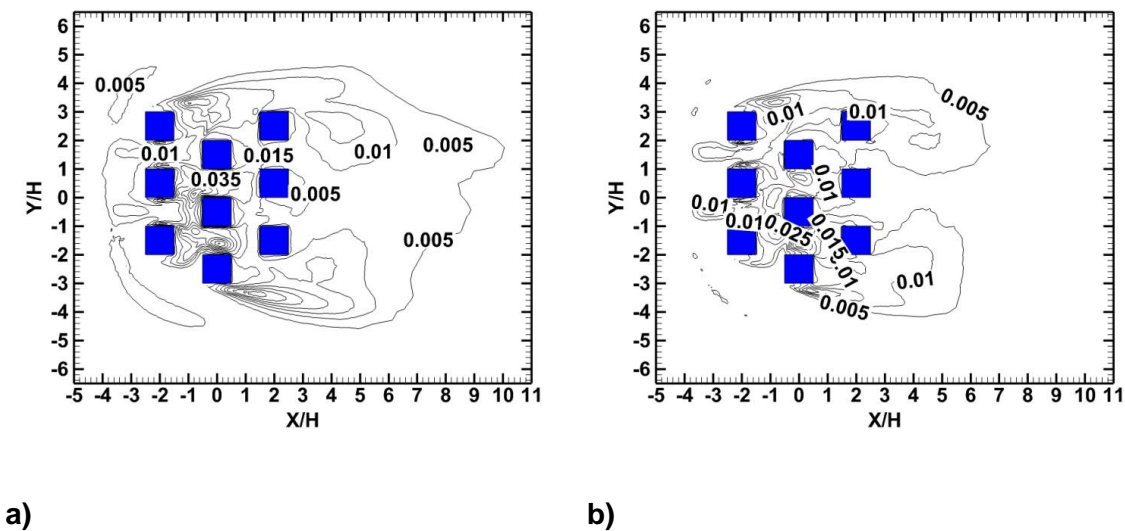
Figure 5-32 Normalized Reynolds stresses on a horizontal plane at a height Z/H=0.08 for a) $\overline{u'w'}/U_\infty^2$ **and b)** $\overline{u'v'}/U_H^2$

91

5.9.3 Experimental Pressure distribution around the SILSOE building inside the staggered array

During this experiment the pressure distribution on the surface of the SILSOE cube along a symmetry line is measured with pressure taps arranged as in Figure 5-6a. The present experimental data and the LES results are compared against the wind tunnel experimental data of Gough [183] in Figure 5-33. The data are in a good agreement for the front and rear face of SILSOE cube but show slight differences on the roof of the cube due to turbulent inlet conditions. The present experimental data show a higher negative value for the pressure coefficient comparing with the numerical results.
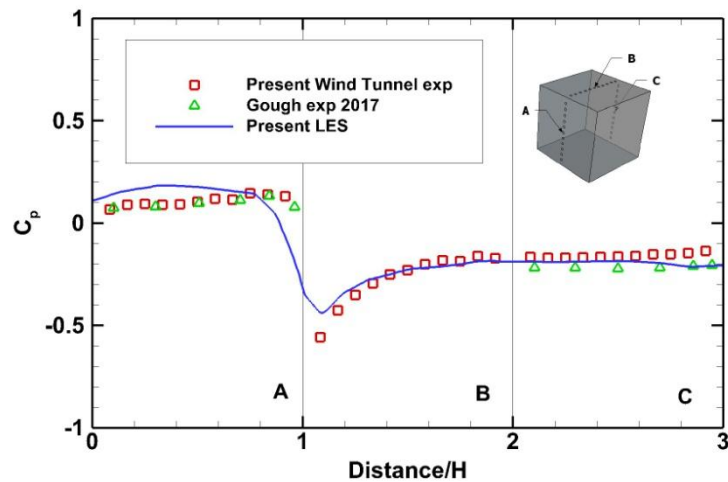
Figure 5-33 Pressure coefficient distribution on the surface of SILSOE cube

Figure 5-34a and b shows the normalized pre-multiplied energy spectra of the streamwise and transverse velocity fluctuations measured with the X-wire anemometer and Figure 5-34c and d presents the LES numerical results at the same position for the same velocities. The spectra values are normalized by the free-stream velocity. The characteristic wavelength of the spectral peak is $St = f H/U_H = 0.14$ for the streamwise velocity and 0.056 for the transverse concerning the anemometry measurements. The LES method presents a spectra peak of 0.14 for the streamwise velocity and 0.12 for the transverse

velocity. The power spectra presents higher level (more energy) in the direction of the streamwise velocity than the transverse velocity.

a)

b)

c)

d)
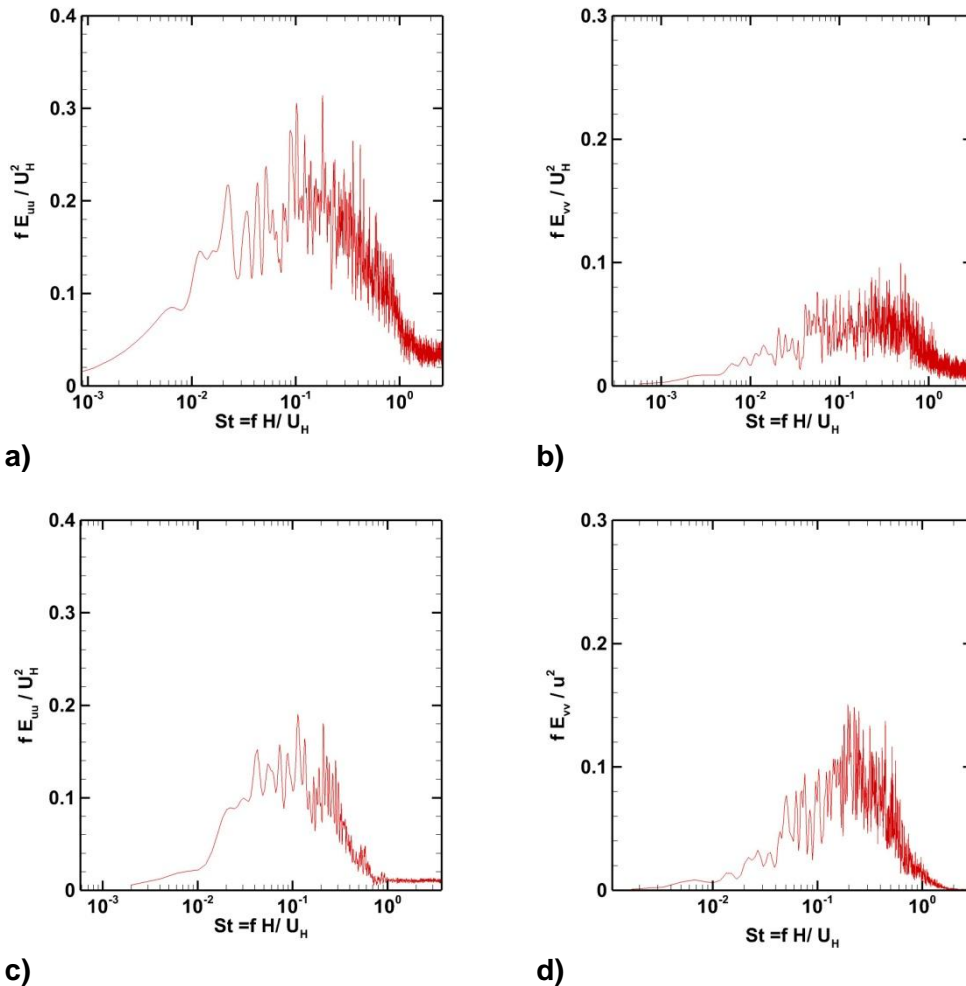
Figure 5-34 Normalized Power Spectra of velocity downstream of the SILSOE cube for a) streamwise and b) transverse velocity fluctuations at the position (2H,2H) for the wind tunnel experiments and c) the streamwise and d) the transverse velocity fluctuations at the same position for the numerical simulations.

5.10 Smoke dispersion

For a general understanding of the smoke dispersion, experiments were made in the wind tunnel environment using a source of the fire smoke barbecue firelighters. The free-stream inlet velocity is described with equation (5-1).

The mechanism of smoke dispersion around a building depends on the molecular mass flux, the mean convective mass flux, and the turbulent mass flux. The turbulent mass flux is created by the velocity fluctuation and the species concentration fluctuation, and it is apparent that gets high values in areas with high turbulence or high species concentration [184].

As shown in Figure 5-35a when the smoke is released inside the cavity zone of the cube, because of the recirculation flow pattern behind the cube and because the buoyancy forces are not important, the smoke cannot escape from this zone. Figure 5-35b shows the dispersion of the smoke in the complex arrays of buildings. Finally, Figure 5-35c shows the smoke dispersion inside a street canyon. The smoke is moving towards the leeward face of the upwind building and it is controlled by the re-circulating flow of the wind inside the canyon and not by the buoyancy forces of the fire source.
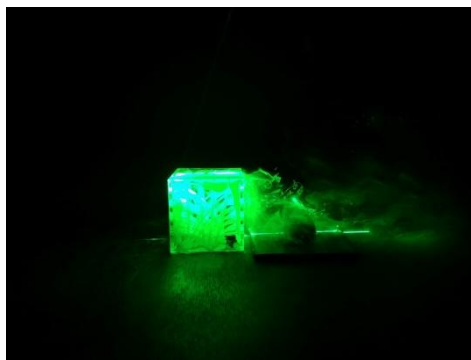
a)
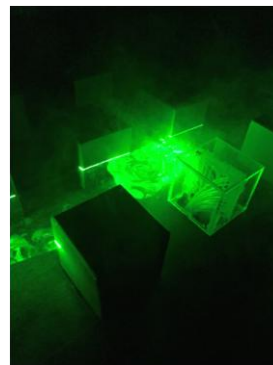
b)

c)

Figure 5-35 Smoke dispersion of a fire located at a) the wake area of the cube, b) in the middle of a buildings array and c) inside a street canyon.

5.11 Conclusions

Experimental and numerical studies have been performed around different urban arrangements of buildings with objectives to understand all the physical parameters that influence the flow and the dispersion of pollutants. The present numerical and experimental results are found to be in good agreement as well as with other numerical and experimental studies from bibliography. This preliminary study provides also the needed experience for the definition of the boundary conditions and the understanding of the physical phenomena involved in this class of problems.

The numerical studies, using LES, revealed the fields of the computed Reynolds stresses which indicate the regions where important momentum fluxes appear and also the regions of intense mixing and dispersion. The flow patterns around different urban arrangement of buildings defined the vortex structures, the recirculation zones and the intense shear layers. This chapter plays also the role of an introduction to the smoke dispersion around these typical urban geometries after a hazardous release accident.

CHAPTER 6. Assessment of air flow distribution and hazardous release dispersion around a single obstacle using Reynolds-averaged Navier-Stokes equations

This chapter focuses on assessing the performance of various RANS models using an unstructured mesh in order to define the air flow and the dispersion of a toxic pollutant around an isolated cubical building. The RANS models around the building underestimate the flow characteristics and influence the pollutant dispersion prediction. The numerical data for the air flow, the turbulence characteristics of the flow and the pollutant dispersion are compared with experimental data from the bibliography. A Gaussian model is also applied, presenting a long extension of the pollutant concentration.

6.1 Introduction

The flow around a cubical building, with a passive vent plume at the central point of the top of the cube, is studied. The Reynolds-averaged Navier-Stokes and species concentration equations are solved for Reynolds number, Re= 40,000, is based on the height of the cube. The predictions obtained with the standard, the Kato-Launder, and the low-Reynolds number k-epsilon models are examined with various wall functions for the near wall treatment of the flow. Results are compared against Martinuzzi and Tropea measurements (J. of Fluids Eng., 115, 85-92, 1993) for the flow field and against Li and Meroney (J. of Wind Eng. and Industrial Aerodynamics, 81, 333-345, 1983) experiments and Gaussian models for the concentration distribution. It is found that the present unstructured mesh model performs similarly to the structured mesh models. Results from the Kato-Launder model are closer to the experimental data for the flow patterns and contaminant distribution on the cube's roof. However, the Kato-Launder model has an over-prediction for the recirculation zone and the contaminant distribution windward of the cube. The standard k-epsilon and the low-Reynolds number k-epsilon models predict similar flow patterns and are closer to the experimental data of the cube's windward and side face.

6.2 Computational definition

6.2.1 Flow field description

The applied computational field is presented in Figure 6-1. The upstream computation length is 5H, the downstream computational length is 10H, the lateral width is 11H and the total height is Z=2H, where H is the height of the cube in the base of which the axes origin is considered.

The results of the simulations are validated against the Martinuzzi and Tropea [20] experimental results that were conducted in a 156H x 24H x 2H wind tunnel in fully turbulent flow with Reynolds's number equal to 40,000, based on the cube's height. For our simulations, we also kept the same Reynolds number.
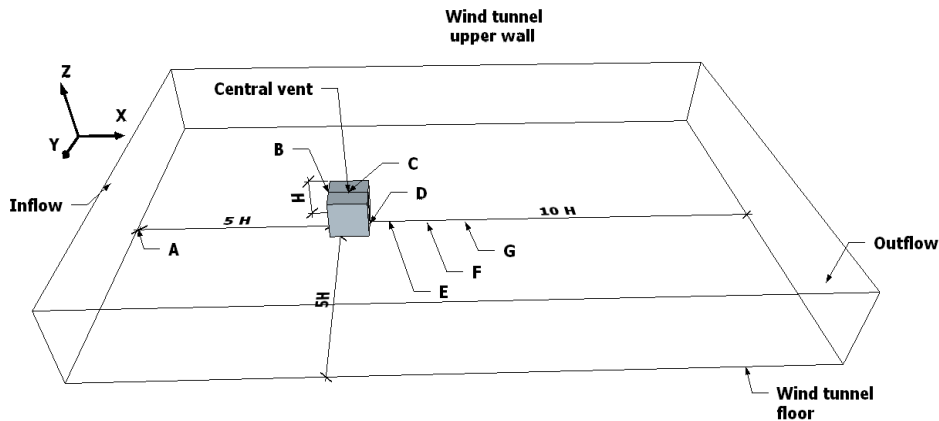
Figure 6-1 Computational domain and boundary conditions. Letters indicates monitoring positions: A (X:-5H, Y:0, Z:0), B(0,0,H), C(0.5H,0,H) , D(H,0,0), E(1.5 H,0,0), F(2.5H,0,0), G(3.5H,0,0).

The vent location is located at the central point of the cube's roof at point C of Figure 6-1. A point source with passive vent plumes and a low minimum dilution criterion is examined. The wind orientation is kept streamwise at 0°. The plume dispersion results are compared against the experimental data of Li and Meroney's [40]. The experimental data for the concentration are collected at Re=11,050, and since the critical Reynolds number for concentration variations is for Re=11,000 [185], no changes on the concentration distributions are expected.

The study of this obstacle at a Reynolds number of 40,000 and a cube of 0.025 meters height corresponds to contaminant dispersion around a typical rectangular building in an urban landscape on a reasonably calm day, which however is challenging for turbulence models due to the low Re turbulent flow regime.

6.2.2 Turbulence models

The Reynolds-averaged Navier-Stokes (RANS) equations are used for the simulations of the present study, where three different turbulence models are tested: the standard k-epsilon model, the Kato-Launder standard k-epsilon model [164], and the low-Reynolds k-epsilon model. Gorji, et al. [165] summarized the model constants, the damping functions and near wall correction functions.

6.2.3 Boundary conditions

The velocity distribution at the inlet is defined with a logarithmic profile [186] obtained from the experimental data:

$$U(z) = U_b \left(\frac{Z}{H}\right)^{0.25}$$

<div align="right">(6-1)</div>

where U_b, is the bulk (average) velocity and H=0.025m is the cube height. The inlet turbulence kinetic energy is calculated using experimental data from the Journal Engineering databank [20].

The inlet boundary conditions for the k and epsilon profiles are well described by Breuer, et al. [30]. The turbulence kinetic energy profile is expressed as k(z)=1.5 (I(z)U(z))^2 where I(z)=$\sqrt{u'^2}$/U$_b$ is the turbulence intensity. The dissipation rate is described as ε(z)=$C_\mu^{\frac{3}{4}}k^{\frac{3}{2}}$/κ L$_u$, where L$_u$ is the turbulence length scale and set as 0.1 H.

No-slip boundary conditions are applied at the bottom, top and cube walls and two different wall function approaches are used. At the top of the computational domain, a wall boundary is applied. The standard wall functions that are based

on the theory of Launder and Spalding [187], for the standard k-epsilon and standard k-epsilon with Kato-Launder models. At the lateral sides, symmetric boundary conditions are applied and usual outflow conditions are applied at the outlet, where the pressure is kept equal to zero and the streamwise derivatives of all other quantities are vanished. These boundary conditions are set far enough downstream from the cube location.

A passive scalar simulates the pollutant release from an orthogonal source on the centre and at the top of the cube with $4 \ 10^{-6}$ m^2 area. The exhaust velocity is kept equal to 1.54 m/sec in all simulations. This velocity is low enough to avoid the jet effect phenomenon [188].

6.2.4 Mesh type

Two types of meshes are used. Far away the walls, an unstructured tetrahedral grid is used and, near the walls a prism mesh. The first cells at the walls are at $7.5 \ *10^{-5}$ m and the expansion ratio for the prism cells is 1.3 which corresponds to $1 < y^+ < 5$. This range of y+, satisfy the minimum values for the low-Reynolds model which is the most restricted. The log-law for the mean velocity near the walls is applied when $5 < y^+ < 11.225$ and the laminar stress-strain relationship is applied for lower values. Furthermore, the enhanced wall treatment is applied for the standard k-epsilon with the low Reynolds model. This near-wall modeling method combines the two-layer model with enhanced wall functions.

The near-wall mesh is fine enough to resolve the laminar sublayer. As shown in Figure 6-2, a grid independence test is conducted based on the standard k-epsilon model with the standard wall functions. It is found that the solution is grid-independent for 4,023,449 cells, where the maximum velocity difference is less than 0.5% from the finer case tested at the location X/H=-5. The coarse grid has 2,036,242 cells and the finer grid has 8,597,367 cells.
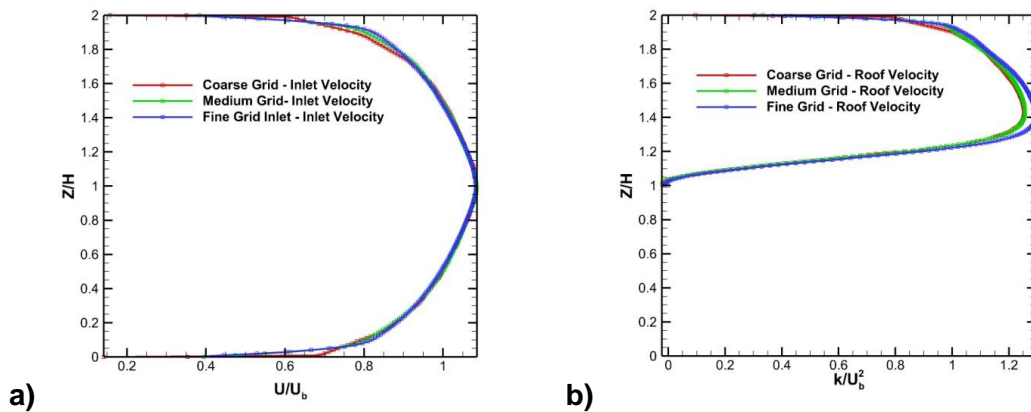
Figure 6-2 A grid independence test based on the standard k-epsilon model with standard wall functions, a) Inlet velocity, location X/H=-5 b) location X/H=0.5

6.2.5 Numerical schemes

The CFD flow solver Ansys Fluent 15 is used for the flow calculation. The SIMPLE scheme is used for pressure and velocity coupling. The nonlinear terms are calculated with a second order upwind scheme, and second order schemes are used for the calculation of all the other terms. The residual error is less than 10^{-5} for all quantities.

6.3 Results and discussion

6.3.1 Flow field results

A 3D geometry with three different turbulence models is compared: the standard k-epsilon model with standard wall functions (St-ke-WF), the Standard k-epsilon with the Kato-Launder model (St-ke-KL) and the Standard k-epsilon with low Reynolds model (St-ke-low-Re). The results obtained from these turbulence models are compared against Martinuzzi and Tropea [20] experimental data in order to validate the flow field and Li and Meroney [40] experimental data for validation of the pollutant dispersion around a cubical building. The comparison of the flow field is made in terms of velocity and turbulence kinetic energy distributions and flow patterns. The flow fields at the symmetry plane, where the main recirculation zone exists and the major

100

separation points formed are presented in the streamlines plots of Figure 6-3a ,b and c, for the St-ke-WF model, St-ke-KL model and St-ke-low-Re models, respectively.

a)

b)

c)

d)
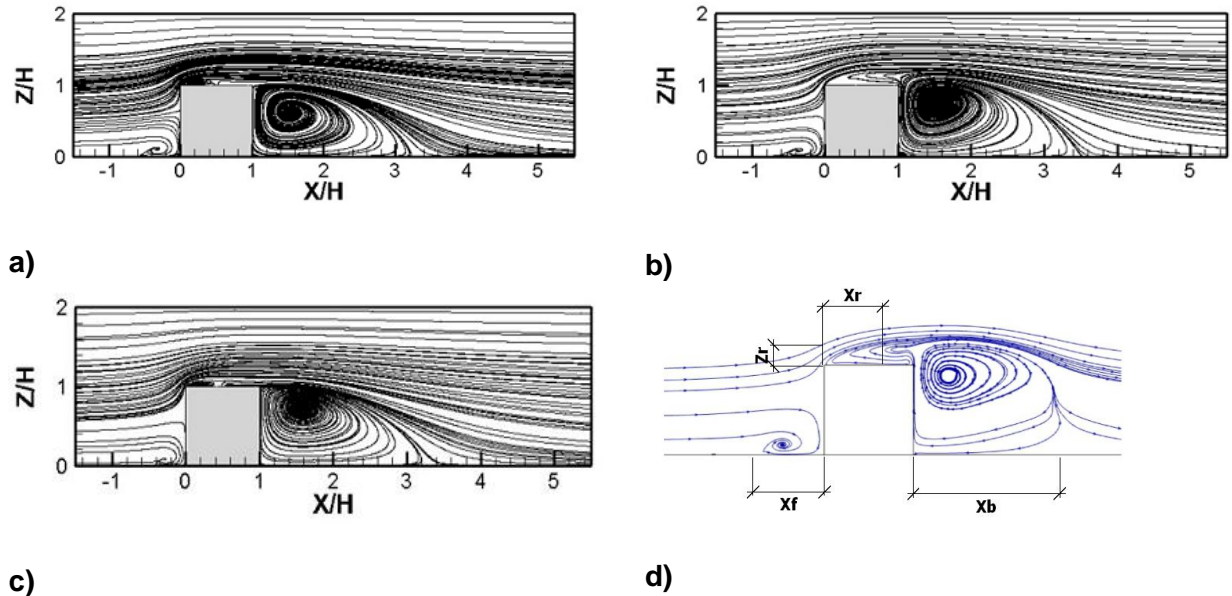
Figure 6-3 Streamlines of the flow at the symmetry plane for a) St-ke-WF model, b) St-ke-KL model, c) St-ke-low-Re model, d) Characteristic separation lengths

The calculated lengths of the main separations points are: X_f for the upstream locations of the cube, X_b for the downstream, X_r for the roof, Z_r is the roof's recirculation height. All are illustrated in Figure 6-3d and summarized in Table 6-1. The centre of the vortex is also summarized in Table 6-1.

Table 6-1 Main separation point lengths

Case	Model	X_f	X_r	X_b	Z_r	Centre of the vortex
Standard k-epsilon with standard Wall functions	St-ke-WF	0.6 H	0.47 H	2.2 H	0.1 H	X =1.55 H Y =0.59 H
Standard k-epsilon with Kato-Launder model	St-ke-KL	0.55 H	-	2.46 H	-	X =1.5 H Y =0.76 H
Standard k-epsilon with low Reynolds model	St-ke-low-Re	0.4 H	0.42 H	2.3 H	0.1 H	X =1.56 H Y =0.78 H
Martinuzzi, et al. [20] experimental data		1.04 H	-	1.61 H	0.17 H	X =1.5 H Y =0.93 H
Lakenhal and Rodi (1997)	k-epsilon with wall functions	0.651 H	0.432 H	2.182 H	-	X =1.58 H Y =0.72 H

As the flow approaches the leeward surface of the cube, the main separation vortex appears. At the leeward cube's surface, the boundary layer detaches and binds the cube by forming the well-known shape of a horseshoe vortex [189]. All the k-epsilon models underestimate this recirculation zone which experimentally is found to extend to $X_f = 1.04$ H. The St-ke-WF model predicts the closest to the experimental separation point at $X_f = 0.6$ H. The St-ke-KL model predicts almost a similar separation point at $X_f = 0.55$ H and the St-ke-low-Re model gives the worst prediction of the separation point at $X_f = 0.4$ H. Moreover, it is found that the St-ke-KL model calculates a long separation zone and does not predict a reattachment point on the cube's roof. This is in agreement with the experimental data and defines better the pollutant dispersion. Results obtained using the St-ke-low-Re and St-ke-WF, models are quite similar i.e.: a small recirculation zone and a reattachment point are found at positions $X_r = 0.47$ H and $X_r = 0.42$ for the St-ke-low-Re and the St-ke-WF models respectively. According to Table 6-1, the St-ke-KL model has a better approximation for the flow around the cube since it does not present a reattachment point at the roof of the cube.

The velocity profiles along Z at points C and D (see Figure 6-1) are illustrated in Figure 6-4 a and Figure 6-4 b. It is found that the St-ke-WF and St-ke-low-Re models predict the velocity profile with a significant difference close to the wall in comparison to Martinuzzi and Tropea experiments. In contrast, similar behavior of the St-ke-WF and St-ke-low-Re models is found to the numerical results of Lakehal and Rodi [36] where the standard k-epsilon model is used in a structured mesh solver. Results obtained by the St-ke-KL model are closer to the experimental ones and the reverse flow is better predicted. At the windward edge of the cube's roof point, only the St-ke-KL model predicts the reverse flow at the edge compared to the other models where the reattachment flow is situated before the cube's centre point.

Figure 6-4 c and Figure 6-4 d illustrate the turbulence kinetic energy distribution at the position C and D, respectively. Results at the C location from the St-ke-WF and St-ke-low-Re models are observed again to be similar; however, results

of the St-ke-KL are found to be in better agreement with the experimental data (except at the peak value) due to the reduced calculated turbulence kinetic energy. The difference in the turbulence kinetic energy peak between models and experiments is more significant at location D. At this position all models underestimate the turbulence kinetic energy compared to the experimental data.
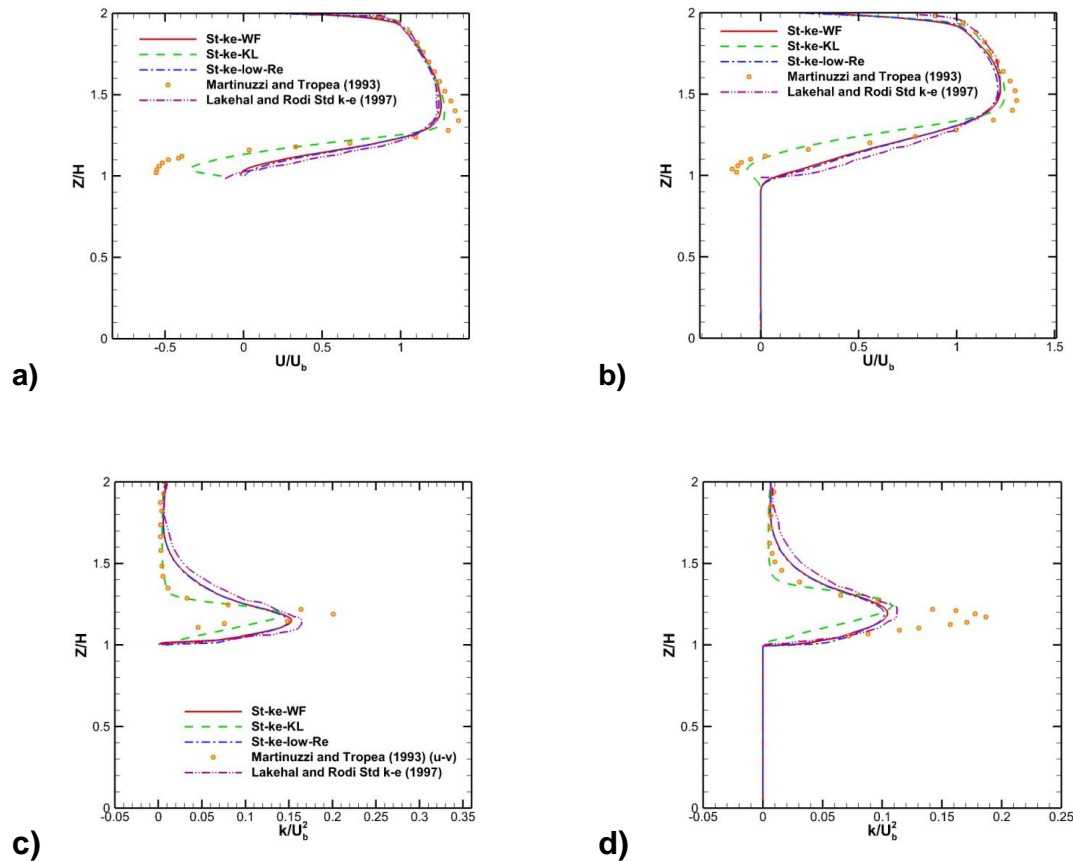
Figure 6-4 Mean velocity (upper) and turbulence kinetic energy (bottom), along Z, normalized by U_b and U_b^2, respectively, for the locations X/H=0.5 (a and c) and X/H=1 (b and d)

All the k-epsilon models over predict the length of the cavity recirculation zone as a result of the underestimation of the turbulence kinetic energy on all cases. Using the St-ke-WF model we obtain results closer to the experimental data with X_b=2.2H. The St-ke-KL model gives the worst overestimated recirculation length with X_b=2.46H, and finally, the St-ke-low-Re model predicts the separation at X_b=2.3H. The windward area behind the cube could be separated

into two different zones. The *cavity zone* (at location E) where the recirculation zone appears with low velocities and high turbulence [190] and the *near-wake zone* situated after the cavity. The velocity distribution from the unstructured grid calculation at the cavity zone and at the near-wake zone are in good agreement against the experimental data of Martinuzzi, et al. [20] and the numerical results from Lakehal and Rodi [36] as shown in Figure 6-5. This result is significant because it shows that the present unstructured solver has the potential to simulate flows in urban environments, despite their complex geometries, with the same accuracy as with a structured mesh solver. Figure 5 a,b and c show the non-dimensional mean velocity distribution at positions E, F and G, respectively. At positions, E and F the mean velocity distribution is in good agreement with the experimental data. At G position the velocity distribution is in agreement at the part above the cube height's and shows differences at the lower part.

a)   b)   c)
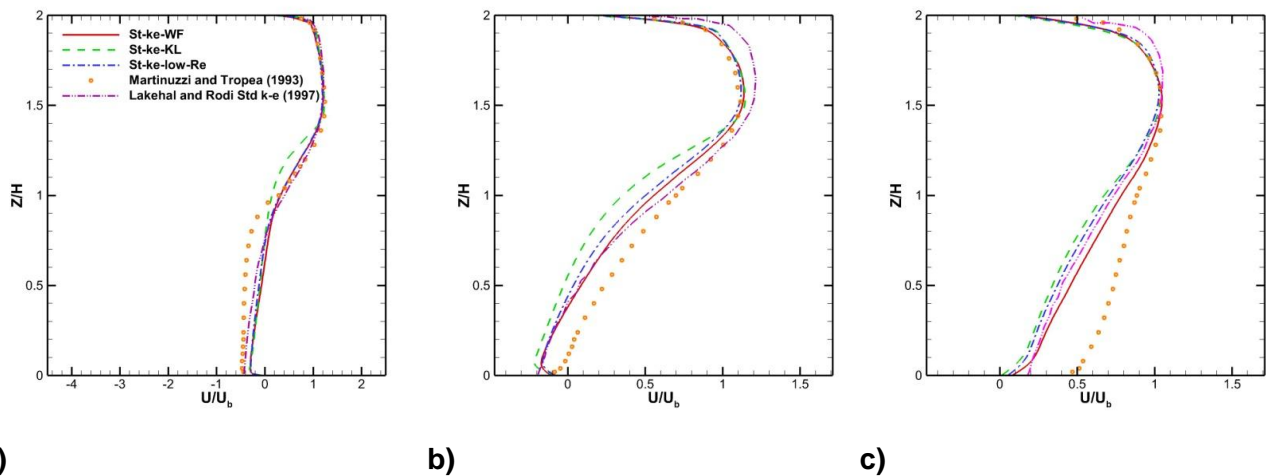
Figure 6-5 Mean velocity U / U_b **at the symmetry plane for the locations a) X/H=1.5, b) X/H=2.5 c) X/H=4**

Figure 6-6 illustrates the iso-surface of the Q criteria, Q=0.1 1/sec^2, for the three different models. It can be seen that the horseshoe vortex is formed on the leeward face of the cube. The horseshoe vortex has a considerable downstream extension for the St-ke-KL (Figure 6-6b) compared to the others models due to the vorticity based formulation of its production source term. The arc-shaped vortex on the leeward face of the cube is similar for all the three

cases. The flow inside the recirculation zone is a strong mixing and turbulence generation region.

a)   b)   c)
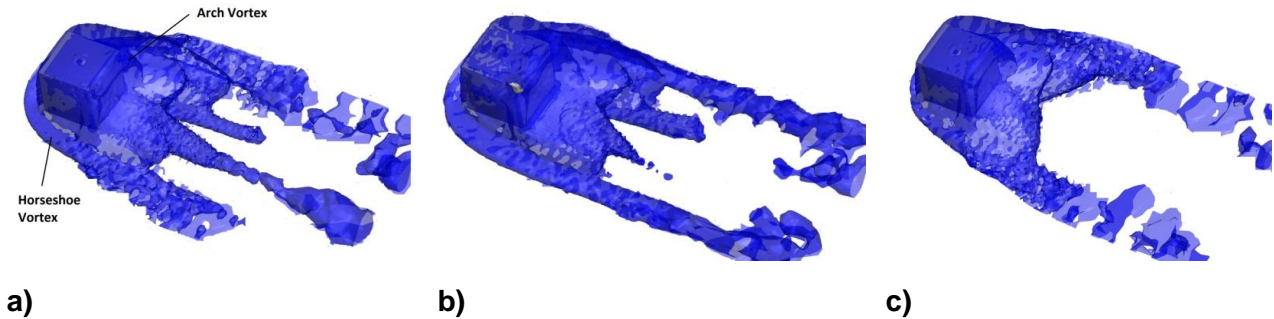
Figure 6-6 Isosurface of the Q=0.1 criteria for a)the St-ke-WF model, b) the St-ke-KL model, c)the St-ke-low-Re mode

6.3.2 Concentration

In order to define the advantages and disadvantages of each numerical model, the distribution of the non-dimensional concentration coefficient, K (equation (4-40)), of the pollutant release around the cube for all the different numerical model is compared. The K distribution is also compared against the Huber and Snyder model (Figure 6-7d) and the Li and Meroney's experimental data (Figure 6-7e).

Huber and Snyder [191] studied the wake effect for short emitted sources and developed a Gaussian equation model to predict the dispersion and transportation of emitted plumes from buildings. According to this model, that is suitable for flows of Re>36,000, the non-dimensional coefficient distribution can be described from the equation :

$$\frac{C\,U_r H}{Q} = \frac{\left[e^{\left(-\frac{1}{2}\frac{y^2}{\sigma_y^2}\right)}\right]\left\{e^{\left(-\frac{1}{2}\left(\frac{z-H_S}{\sigma_z}\right)^2\right)} + e^{\left(-\frac{1}{2}\left(\frac{z+H_S}{\sigma_z}\right)^2\right)}\right\}}{2\,\pi\,\sigma_y\,\sigma_z\Big/_{H^2}}, \tag{6-2}$$

and the dispersion parameters can be calculated from the expression :

$$\frac{\sigma_z}{H} = \frac{\sigma_y}{H} = 0.115\left(\frac{x}{H}\right)^{0.8}, \tag{6-3}$$

H_s is the source height that is situated in the cube, and in our case $H_s = H$ since the pollutant is released from the top of the cube.

Figure 6-7, shows some qualitative characteristics regarding the dispersion of the non-dimensional concentration coefficient, K with isopleth graphs. In order to understand the mechanism of the concentration dispersion, the study of the mass diffusion is realized. According to equation (4-37) and (4-38) the concentration is treated as species which is transferred by the advection-diffusion equation. The convective transfer of the mean concentration is defined as $Q_{convection} = CU$, the turbulent concentration flux is defined as $Q_{turbulent} = -\frac{v_t}{Sc_t}\frac{\partial C}{\partial x_i}$, and the molecular diffusion flux is defined as $Q_{molecular} = -D_{i,m}\frac{\partial c}{\partial x_i}$ [192].

Furthermore, in order to understand the mechanism of the concentration dispersion around the cube, the convective concentration fluxes (Figure 6-8) and the turbulent concentration flux (Figure 6-9) for the streamwise (x-direction) at the symmetry plane is realized for all the numerical cases. As shown in Figure 6-8 , the pollutant is primarily transferred by convection downstream of the cube and only a small quantity of the pollution reaches at the cube's cavity zone.

The St-ke-WF, St-ke-low-Re and Huber and Snyder models present similar distributions for the concentration coefficient, K, at the constant value of 1 (Figure 6-7a,c). On the other hand, the St-ke-KL model (Figure 6-7b) presents a larger concentration length leeward the cube, at the constant value of 1. The Kato-Launder wall functions at the cube's surfaces have as result the negative values of the convective mass flux at its rooftop and present a larger concentration length due to the higher convective mass flux (Figure 6-8b). Negligible differences at the convective mass flux distribution at the cube's roof between the St-ke-WF and St-ke-low-Re models have as result small differences at the concentration's length.
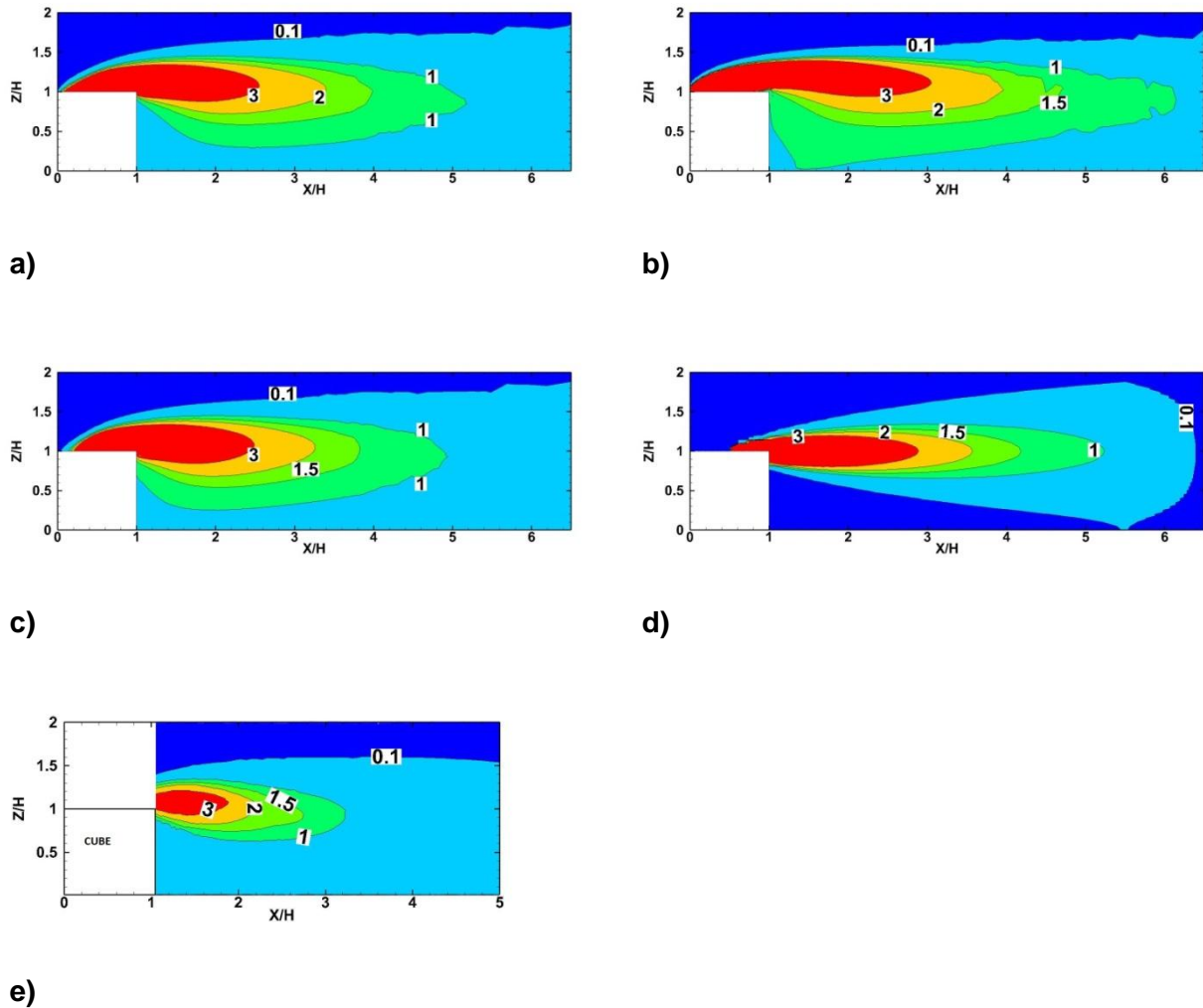
Figure 6-7 The non-dimensional K distribution at the symmetry plane for a) St-ke-WF, b) St-ke-KL, c) St-ke-low-Re d) Huber and Snyder models and e) the experimental data Li and Meroney (1983).

The St-ke-KL model presents important concentration values near the ground (Figure 6-7b) because the turbulent mass flux area is extended in a higher limit at the cube's height and traps more pollutant into the cavity and wake area (Figure 6-9b). Huber and Snyder models cannot predict the downwash effect that brings higher concentration near the ground (Figure 6-7d). Li and Meroney's experimental data present a smaller extension for the pollutant concentration comparing to all the present numerical models and the Huber and Snyder model.
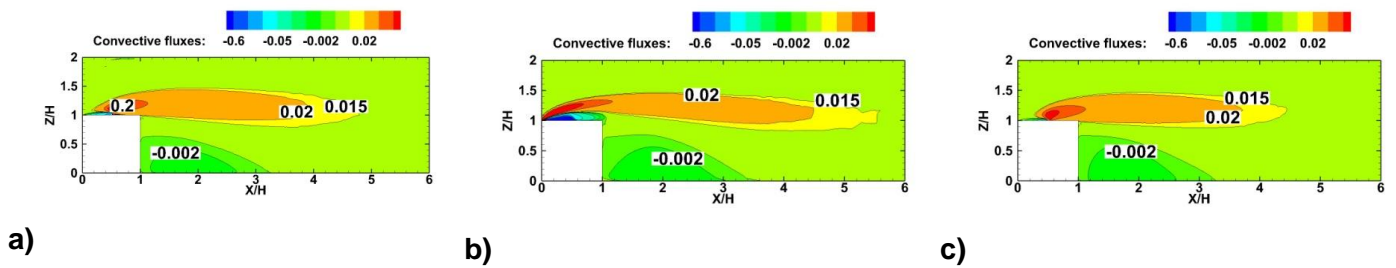
Figure 6-8 Convective mass flux at the symmetry plane for a) St-ke-WF, b) St-ke-KL, c) St-ke-low-Re model
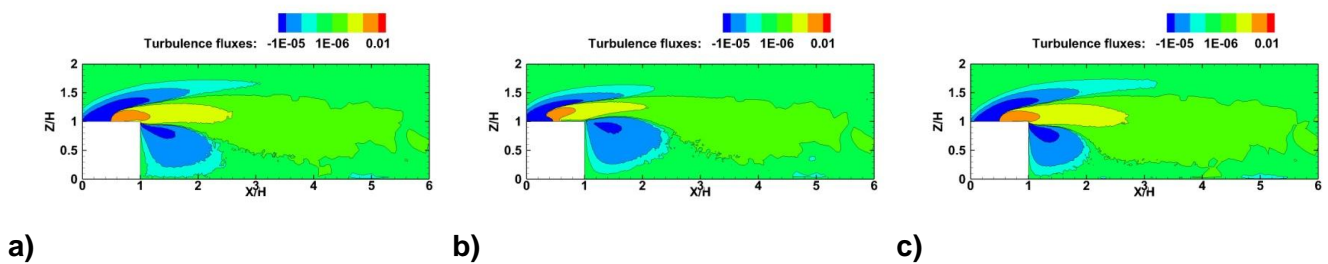
Figure 6-9 Turbulent mass flux at the symmetry plane for a) St-ke-WF, b) St-ke-KL, c) St-ke-low-Re models

The k-epsilon models predict different K distributions also in the roof of the cube (Figure 6-10) because of the velocity distribution and turbulence kinetic energy differences. The St-ke-WF and St-ke-low-Re models predict higher values of K windward of the release vent. Instead, the St-ke-KL model predicts a higher concentration area at the upwind vent area. The concentration distribution predicted by the St-ke-KL model is in better agreement with the Li and Meroney experimental data [40]. This agreement is due to the better calculation of the reverse flow at the top of the roof since the reattachment point is windward to the vent location. For this reason, the pollutant is trapped into the recirculation zone. Figure 6-11 shows a 3-dimensional view of the non-dimensional concentration dispersion for the constant value of 1. The negative values of the convection mass flux (Figure 6-8b) are moving the plume direction opposite of the wind direction.
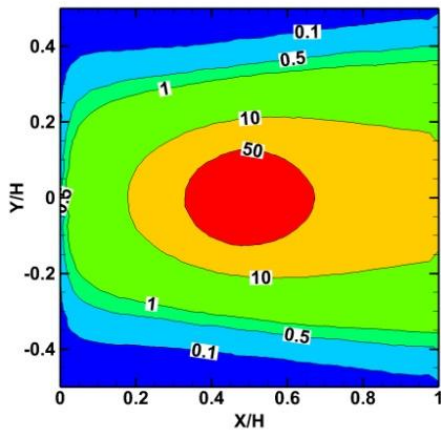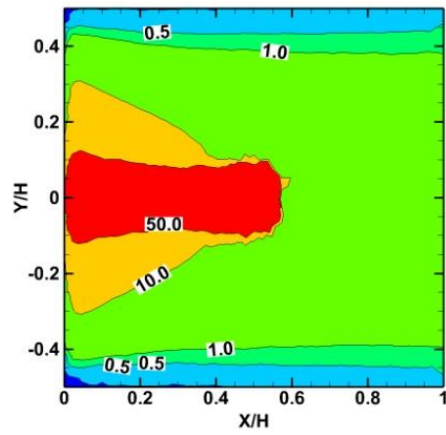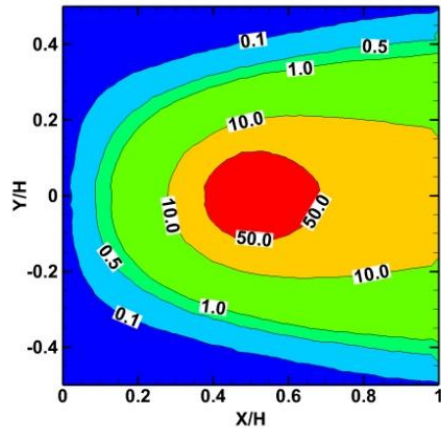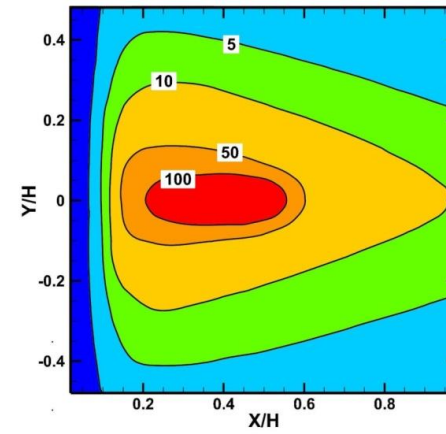
Figure 6-10 K distribution at the cube's roof a) St-ke-WF , b) St-ke-KL, c) St-ke-low-Re models and d)the experimental results from Li and Meroney (1983)
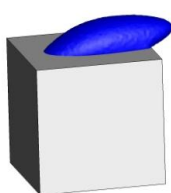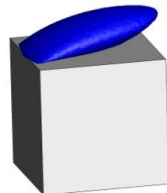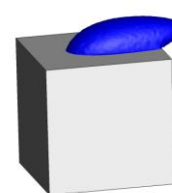
Figure 6-11 Iso-surface for K=1 distribution at the cube's roof for a) St-ke-WF , b) St-ke-KL, c) St-ke-low-Re models

Figure 6-12 shows the contours of K on the downstream wall of the cube. The dominant experimental K values (Figure 6-12d) on the windward face of the wall lie between 0.5 and 1.0 which is in a better agreement with the St-ke-KL model distribution (Figure 6-12b). The St-ke-WF (Figure 6-12a) and St-ke-low-Re (Figure 6-12c) models calculate similar K distribution that differs from the experimental concentration one. Higher values of K are found mostly in the center area of the windward face of the cube and are presenting an expansion towards the cube's base.
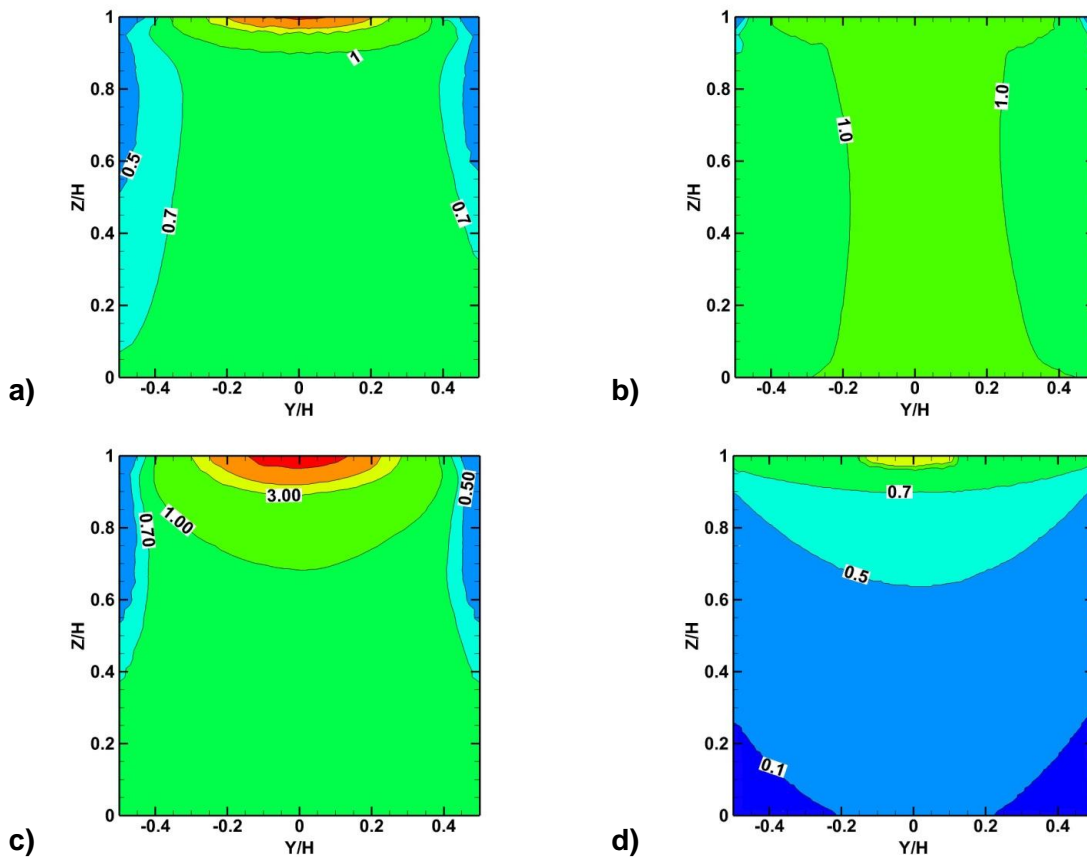
Figure 6-12 K distribution at the cube's windward face for a) St-ke-WF, b) St-ke-KL, c) St-ke-low-Re models and d)the experimental results from Li and Meroney (1983)

The K concentration at the side wall of the cube is illustrated in Figure 6-13. The experimental data shows that the main concentration is transported from the roof to the upper part of the side wall (Figure 6-13d). The present results (Figure 6-13a, b, c) under-estimate the concentration at the upper part of the side wall

and found important concentration at the lower part of the wall which is transferred from the leeward face of the cube. The K distribution is quite similar for the St-ke-WF (Figure 6-13a) and St-ke-low-Re (Figure 6-13c) models, which present higher concentrations at a small area at the low part of the side wall cube. The St-ke-KL model (Figure 6-13b) concentration values are at the lower part of the side wall of the cube but there is much higher dispersion at the side wall of the cube.
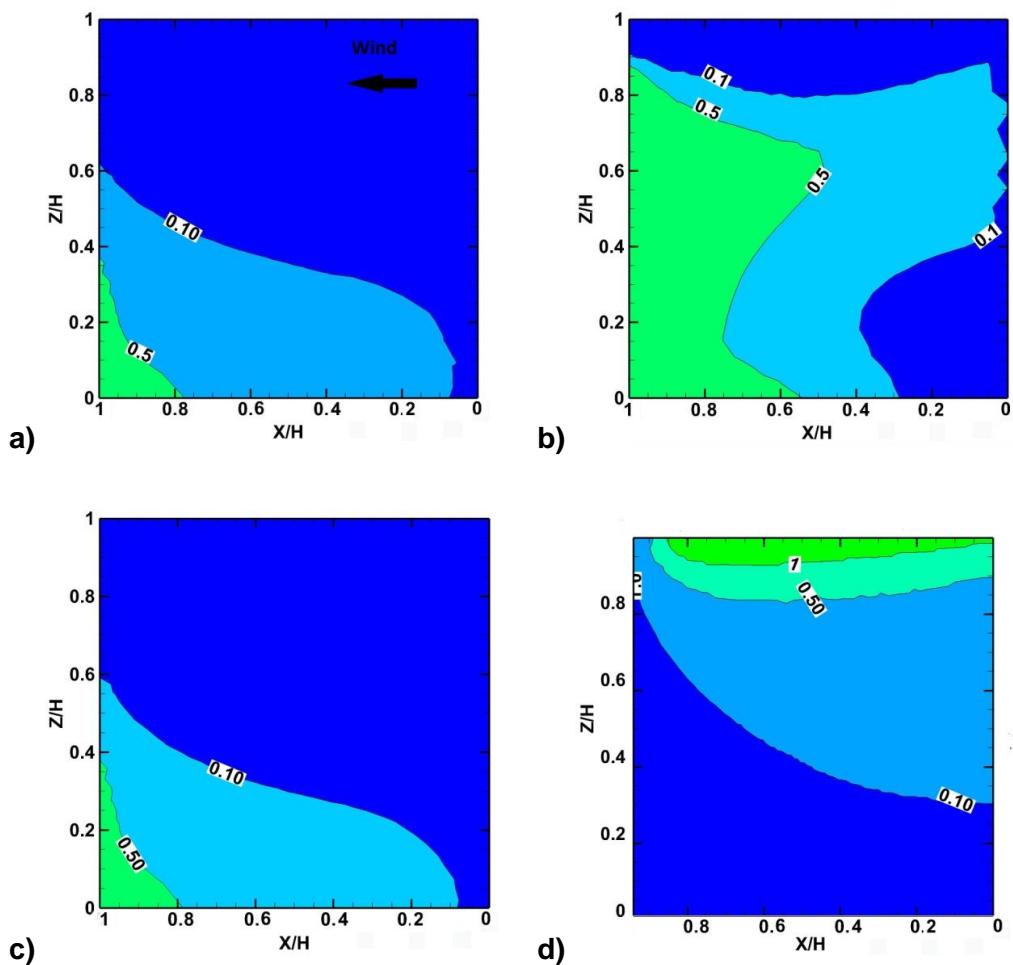
Figure 6-13 Non-dimensional concentration coefficient distribution at the cube's left face a) St-ke-WF, b)St-ke-KL, c)St-ke-low-Re models, and d) the experimental results from Li and Meroney (1983)

The K level decreases as the flow passes through the cube edges. The plume concentration distribution follows the air flow behavior. The concentration rapidly decreases after passing the cube edge as is shown in Figure 6-14. At the edge point of the cube, a significant underestimation of the non-dimensional

concentration coefficient appears for all the k-epsilon models compared to Li and Meroney's experimental data. Predictions from St-ke-WF and St-ke-low-Re models are in better agreement with the experimental data while the one from the St-ke-KL model underestimates K.
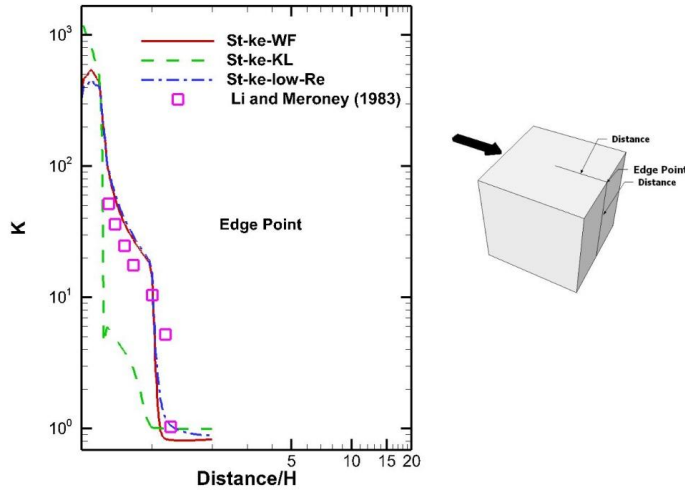
Figure 6-14 K distribution on the cube's roof and leeward face at the symmetry line (Distance line is marked in the right cube).

Different lateral isopleths planes are examined at the positions E, F and G in Figure 6-15. The highest K value is observed at the centre of the isopleths at the source height. Moving downstream from the release source the values decrease and the K distribution is expanding laterally and longitudinally. Increasing the distance windward of the cube, all numerical results (Figure 6-15a,b,c,d,e,f,g,h,i) appear to have higher K values than in the Li and Meroney experimental data (Figure 6-15m,n,o). The K distribution for the Huber and Snyder model (Figure 6-15j, k,l) is denser around the plume centerline than the other results. Finally, the K distributions, as predicted by the numerical results, show a crucial vertical dispersion towards the lower part of the cube, contrary to the experimental results that show an important lateral dispersion.
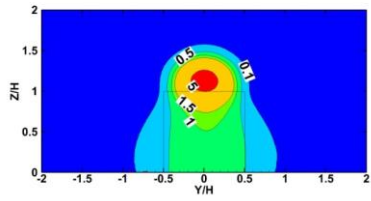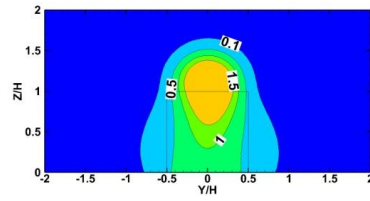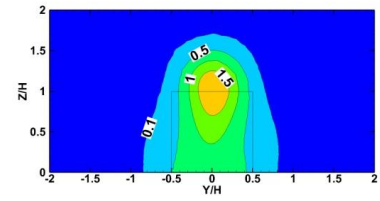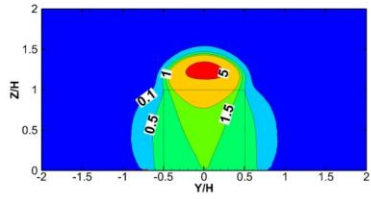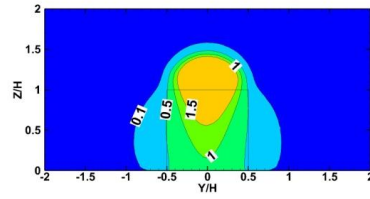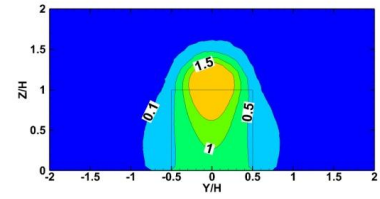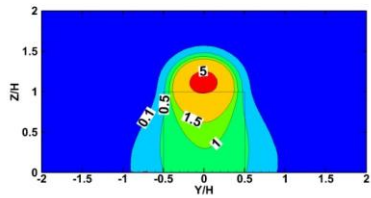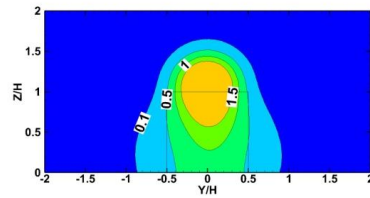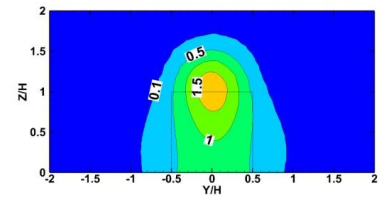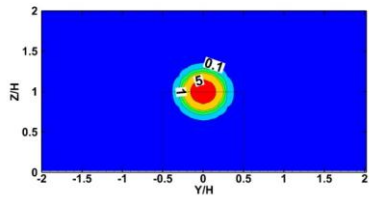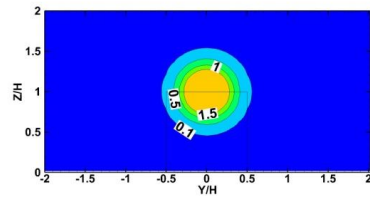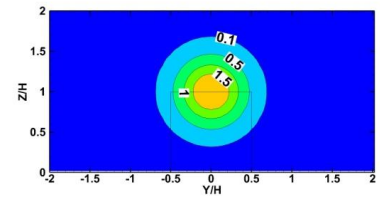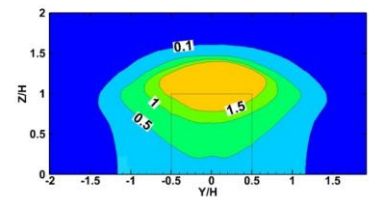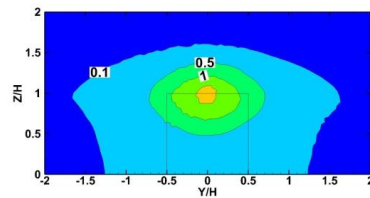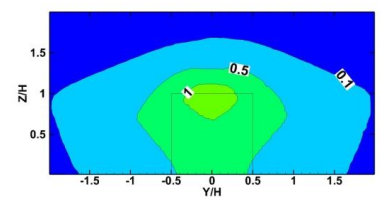
Figure 6-15 K profiles for the St-ke-WF model: (a) at X/H=1.5, (b) at X/H=2.5, (c) at X/H=3.5, the St-ke-KL model: (d) at X/H=1.5, (e) at X/H=2.5, (f) at X/H=3.5, and St-ke-low-Re model: at (g) at X/H=1.5, (h) at X/H=2.5, (i) at X/H=3.5 , the Huber and Snyder model: (j) at X/H=1.5, (k) at X/H=2.5, (l) at X/H=3.5) , and the experimental results from Li and Meroney (1983): (d) at X/H=1.5, (e) at X/H=2.5, (f) at X/H=3.5

Figure 6-16 illustrates the K variation in the Z direction for different positions behind the cube. At point E, inside the recirculation zone, the prediction of the St-ke-KL model is in better agreement with the experimental data than the other two k-epsilon models. Moreover, K distributions from the St-ke-WF and St-ke-low-Re models predict similar behavior and an important dimensional concentration increase is found slightly above the cube height. At point F, near the limit where the recirculation zone ends, the St-ke-WF and St-ke-low-Re models have similar behavior and are in a better agreement with the experimental data. The St-ke-KL model overestimates the prediction of K compared to the other two models. At point G, all numerical models are in a good agreement with the experimental data. The St-ke-KL shows a small overprediction of the K values.

a)   b)   c)
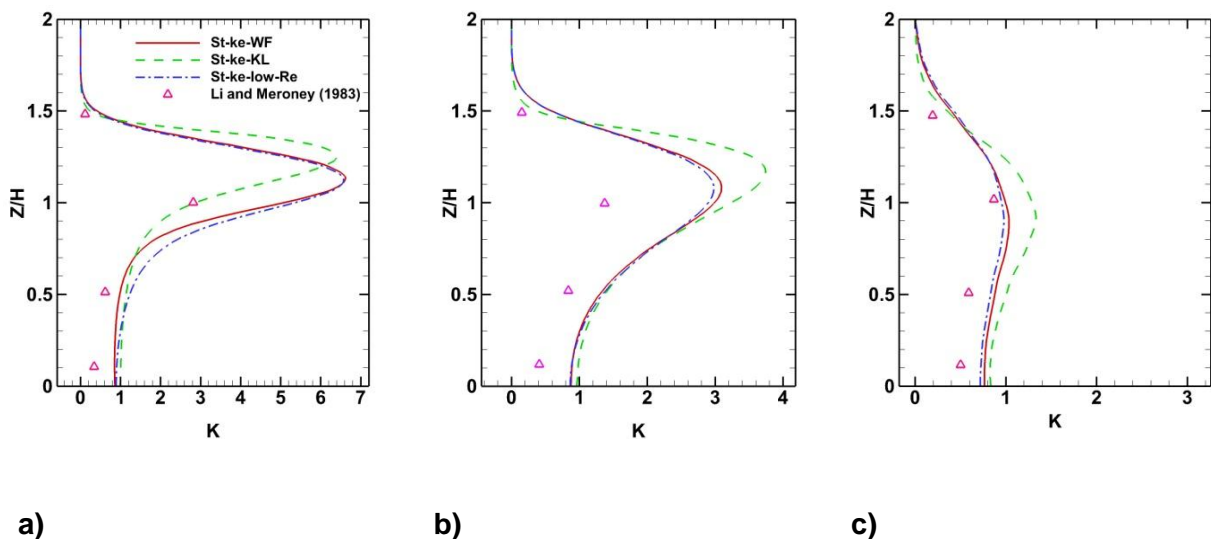
Figure 6-16 Non-dimensional concentration coefficient distribution at a) X/H=1.5, b) X/H=2.5 and c) X/H=3.5

6.3.3 Conclusion

In this research, the flow around a cube with a contaminant source release at the roof is tested with different k-epsilon turbulent models. The obtained results are compared against the experimental data of Martinuzzi, et al. [20] and Li and Meroney [40], the numerical results of Lakehal and Rodi [36], as well as the Gaussian model of Huber and Snyder [191]. All k-epsilon models are found to

underestimate the flow characteristics around the cube something that affects the inflation of the pollutant dispersion around the cube.

At the cube's roof the St-ke-KL model predicts a long separation zone and does not have a reattachment point on the top of the cube's roof. The St-ke-WF and the St-ke-low-Re models predict a small recirculation zone and a reattachment point at a position which is situated before cube's centre. This estimation led to high concentrations windward of the release vent which is not confirmed from the experimental data.

All the k-epsilon models over-predict the length of the cavity recirculation zone. St-ke-KL gives the most overestimated recirculation length and the St-ke-WF gives results closer to the experimental data. St-ke-low-Re and St-ke-WF show similar recirculation zones. This long recirculation length results from the underestimation of the turbulence kinetic energy (G_k term).

The concentration level decreases as the flow passes through the cube's edges. At the edge point of the cube an important underestimation of the dimensional concentration appears for all the k-epsilon models compared to Meroney's experimental data. St-ke-WF and St-ke-low-Re models are in better agreement with the experimental data. The St-ke-KL plume dispersion is in better agreement with the Meroney's experimental data and shows a more diffusive main core than the St-ke-WF and St-ke-low-Re models.

According to the symmetry plane, the St-ke-WF and St-ke-low-Re models have similar dimensional concentration lengths to the Huber and Snyder model. St-ke-KL dimensional concentration length is slightly longer. The experimental data results give smaller lengths than RANS and Huber and Snyder model. But Huber and Snyder's model fail to predict the downwind shift of the dimensional concentration. On the other hand, RANS models are in better agreement with the experimental data. Comparing different lateral isopleths planes behind the cube, St-ke-WF is better agreement with the experimental data compare to the other k-epsilon models near the wake cube. In contrast, moving away behind the cube the St-ke-low-Re is in a better agreement with the experimental data.

In order to define the hazardous release dispersion for safety approaches, it is important to study the advantages and disadvantages of each model. The St-ke-WF and St-ke-low-Re failed to accurately predict the central roof hazardous material release. St-ke-KL has a better approach and could be an option for this kind of problems. On the contrary, St-ke-KL over-predicts the hazardous zone compare to the other two models that are in a better agreement with the experimental data. None of the examined models were able to satisfactorily predict the lateral dispersion of the pollutant at the sides of the cube, as measured in the experiment of Li and Meroney [40]. St-ke-WF and St-ke-low-Re are in better agreement with the experimental data of the non-dimensional concentration variation with distance from the edge of the cube. St-ke-KL over predicts the non-dimensional concentration. It is found that the St-ke-WF and St-ke-low-Re models give a better approximation for the hazardous release dispersion windward of the cube, but the St-ke-KL model is better for the dispersion at the cube's roof.

CHAPTER 7.   LES study of the hazardous release from a fire accident around a cubical building

The aim of this chapter is to verify the accuracy of the LES method in the event of a hazardous dispersion when an unstructured mesh is used. The idea is to compare the flow characteristics of the wind around a cube combined with a fire accident occurring in the wake zone of the flow. The numerical results of the flow around a cube without any hazardous material release are compared with the experimental data of the SILOSE cube. A fire pool accident is studied as an accidental scenario. Two different fuel cases are studied, a case with a crude oil pool fire and a case of a diesel pool fire.

The smoke distribution is calculated for both cases and the toxic zones around the cube are defined. The smoke dispersion due to buoyancy forces is compared with Tominaga, et al. [16] experiments. Besides buoyancy forces, large-scale turbulent motion is generated which controls the diffusion of mass and momentum. The mixing of fuel and air is controlled by this relatively slow turbulent mixing process rather than the fast chemical kinetics.

One of the study's most important conclusions is that it defines the toxic zones, which is necessary for the post-accident intervention. Even though different fire accidents produce different total heat rate releases, the toxic zones that are generated present similar characteristics.

7.1 Introduction

The turbulent smoke dispersion from a pool fire around a cubical building is studied using Large-eddy Simulations for the high Reynolds number of Re= 4.1×10^6, based on the height of the cube. Two different cases of fuel fire are studied, the crude oil fire case with a 7.8 MW heat rate release and the diesel pool fire accident case with 13.5 MW heat release rate. The fire accidents are found to be influenced by convective, buoyancy forces and turbulence mixing processes that affect the concentration dispersion in the building's wake zone,

defining the toxic zones behind the cube. The wind behavior and the smoke concentration around the cube is compared against standard experimental data. In both the cases studied, the downstream length of the toxic zone is approximately the same, indicating that the large scales are mainly responsible for smoke dispersion.

The objective of the present work is to verify the accuracy of the LES method in studying hazardous dispersions using unstructured mesh and to compare the flow characteristics around a cube in combination with a fire accident occurring in its wake zone. To achieve these objectives:

- The numerical results of the flow around a cube without released hazardous materials are compared with the experimental data of the SILOSE cube.
- A fire pool accident scenario for two different fuel cases are studied, the first case with a crude oil pool fire and the second case with a diesel pool fire.
- The smoke distribution is computed and the toxic zones around the cube are defined. In the cases of fire, the flow is driven by buoyancy forces that increase the turbulent mixing in the rising plume [193]. The smoke dispersion due to buoyancy forces is compared with Tominaga, et al. [16] experiments.

7.2 Computational definition

7.2.1 Flow field details

The present simulations study the turbulent flow field around the SILSOE cube that is considered a standard case for atmospheric flows around isolated buildings. The SILSOE cube experiment was performed in the SILSOE Research Institute where a 6m height cube was exposed in the open country. Several different studies were performed for the flow around this cube [14, 15, 17, 173, 194]. Except for the field experiments, wind tunnel and numerical simulation studies have been also performed for the SILSOE cube [28, 172, 194-196].

The present computational domain is shown in Figure 7-1, where the coordinate's origin is in the middle of the rear edge of the bottom face of the cube. The upstream boundary of the computational domain is 5H from the front face of the cubic building, the downstream computational boundary is 10H from the rear cube face, the lateral width of the computational domain is 11H and its height is Z=5H, where H is the height of the cube. The German Association of Engineers (VDI) guidelines suggest that the maximum blockage effect of the cube should be below 10%, which for our selected computational domain is 5% [197].
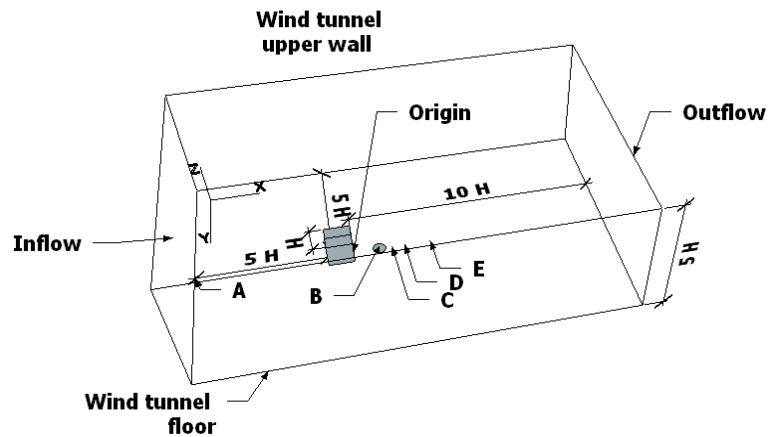
Figure 7-1 Computational domain and boundary conditions. The alphabetic letters indicate the monitoring positions: A (X:-5H, Y:0, Z:0), B(H,0,0), C(1.5 H,0,H) , D(2 H,0,0), E(3 H,0,0) and the origin (0,0,0) is located at the rear face of the cube

The Reynolds number in the present simulation is kept equal to Re= 4.1×10^6, based on the cube height H. The wind orientation is kept in the streamwise direction, 0°. The centre of the emission source, point B, is located on the floor of the computational domain and at a distance H behind the cube. Two different cases are studied, one with crude oil and the other one with diesel oil.

7.2.2 Pool fire characteristics

The fire source is considered as a plume above the 3m diameter pool of oil. Two different pool fire cases are studied. Case 1 corresponds to a crude oil pool

fire and Case 2 to a diesel pool fire. The fuel mass loss $\dot{m}''$ and the total heat release rate $\dot{q}$(HRR) are calculated as [198] :

$$\dot{m}'' = \dot{m}''_{\infty} (1 - e^{-k\beta D})$$ **(7-1)**

$$\dot{q} = m'' \Delta H_{c,eff} \dot{A}_{pool}$$ **(7-2)**

where, $\dot{m}''_{\infty}$ is the infinite-diameter pool mass-loss rate, $\Delta H_{c,eff}$ is the heat of combustion, A_{pool} is the fire surface of the pool, β is the mean beam length corrector, k is the absorption extinction coefficient of the flame, and D is the pool diameter.

The crude oil pool fire mass burning rate is 0.028 kg/sec m^2 and the total heat release rate $\dot{q}$ (HRR) is 7.8 MW [198]. The mass burning rate of the diesel pool fire is set to 0.045 kg/sec m^2 and the HRR is 13.5 MW. The convective part of the HRR for both cases is $\dot{q}_c$=0.7$\dot{q}$.

Smoke yield is an important parameter for the smoke products and defines the ratio of the smoke's mass production to the fuel mass loss (kg smoke/kg fuel). The smoke yield for crude oil is from 10% to 15% according to Evans, et al. [199] and here is taken to be 12.5% [6]. The diesel oil is composed of 75% saturated hydrocarbons and 25% aromatic hydrocarbons. Walton, et al. [200] assumed that the smoke yield varies between 15% and 20% for the diesel oil [6] and the average value of 17.5% is considered here. The composition of emissions of a petroleum hydrocarbon fire is water vapor, carbon dioxide (92%), carbon monoxide (3.2%) and PM (5%) [201].

The pool fires are modeled as a source of a thermal gas which is injected normal to the ground into the computational domain through a circular area of radius R=1.5 m at location B. The mass of smoke released for crude oil pool fire and diesel pool fire are 0.032 kg/sec and 0.053 kg/sec, respectively.

7.2.3 Boundary conditions

The inlet velocity distribution of the atmospheric boundary layer is experimentally defined by Richards, et al. [194] as:

$$U(z) = \frac{u_*}{\kappa} \, ln\left(\frac{z + z_o}{z_o}\right) \qquad \text{(7-3)}$$

$$u_* = \frac{\kappa \, U_{ref}}{ln\left(\frac{z_{ref}}{z_o}\right)} \qquad \text{(7-4)}$$

where, $z_{ref} = 10$ m is the reference height, $U_{ref} = 10.13$ m/sec is the wind speed at the reference height [172], $z_0 = 0.01$ is the roughness height [202], $C_\mu = 0.09$ is the model constant, $\kappa = 0.4$ is the von Karman constant [203]. In order to define the fluctuations at the inlet for the LES model, the vortex method is applied.

At the lateral sides of the domain, periodic boundary conditions are applied and usual outflow conditions at the outlet, where all derivatives vanish and the pressure is kept equal to zero are applied. These boundary conditions are set far enough downstream of the cube.

7.2.4 Buoyancy Forces

In a fire accident, buoyancy plays an important role in the fire pollutant concentration and dispersion due to the thermal upward fluid motions. On the other hand, the wind flow with its inertial forces curves the fire plume and traps the fire pollutants inside the cube's recirculation zone. The ratio of the thermal buoyancy forces to the wind convection forces is described by the Richardson number:

$$Ri = \frac{g \, \Delta T \, H}{T_\infty \, u^2} \qquad \text{(7-5)}$$

where, ΔT is the temperature difference between the fire plume, the air temperature T_∞, g the gravity and u the velocity at the cube height. At low Richardson numbers the temperature difference, ΔT, is small and the buoyancy forces are not significant. In the present case, it is found that the Richardson number is 2.36 and 2.56 for the crude oil and the diesel pool fires, respectively. For both the cases, the high Richardson numbers show that the buoyancy

forces to be important and the mixing between the smoke products and the air is minimized.

7.2.5 Numerical schemes

The CFD flow solver Ansys Fluent 17 is used for the flow calculation. The PISO scheme is used for the pressure and velocity coupling. The nonlinear terms are calculated with a second order Upwind scheme. A second order upwind scheme is used also for the discretization of all other terms of equations (1-21), (1-22) and (1-29). The convergence criteria are kept less than 10^{-5}, based on the absolute error of all quantities. For the unsteady simulations, a time step of 0.005 sec is used. In order to initialize the case, a steady state simulation was performed with the application of the standard k-epsilon RANS model.

7.2.6 Grid Resolution

Two types of meshes are used, a tetrahedral unstructured grid outside the boundary layers and a prismatic mesh inside the boundary layers. The first cells normal to the walls are at 7.5×10^{-5} m and the expansion ratio for the prism cells is 1.3. The near-wall mesh is fine enough to resolve the laminar sublayer. In order to estimate the error due to the grid sensitivity, the grid convergence index (GCI) method is used [204] as described by Chatzimichailidis, et al. [205]. Three different grids are studied, a coarse, a medium and a fine grid. Three different grids are used, a coarse, a medium and a fine grid. The error estimated from these grids is:

$$GSI = \frac{f_2 - f_1}{1 - r^p} \qquad \text{(7-6)}$$

where, f_2 is the numerical solution obtained by a coarse grid, f_1 is the numerical solution obtained by a finer grid, r is the refined factor between the coarse and the fine grid and p is the accuracy of the algorithm (p=2). A coarse grid consistent of 1,527,575 cells, a medium grid of 2,415,662 and a fine grid of 3,659,771 are used. This means that the refined factor between the grids is r=1.5.

a) b)
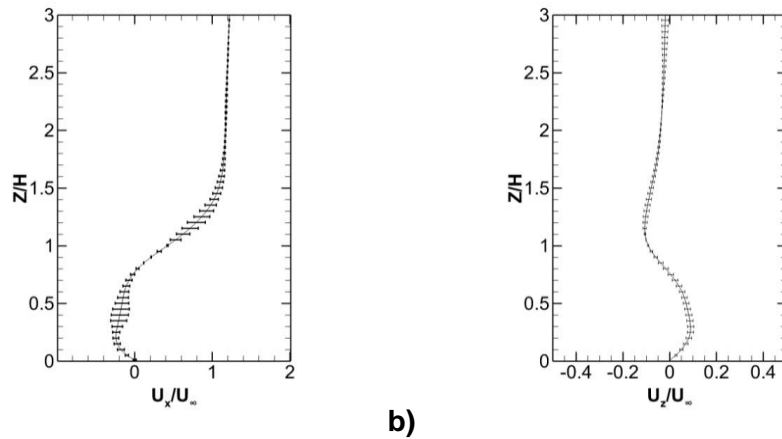
Figure 7-2 The GCI error bars estimated from medium to fine grid for the computed non-dimensional U_x / U_∞ and U_z / U_∞ mean velocities based on the medium grid 0.5H behind the cube

The grid error is examined in a streamwise position 0.5H behind the cube, inside its wake. The GCI values are tested for the U_x/U_∞ and U_z/U_∞. The GCI values between the coarse and the medium grid are found to be 2.56% for the U_x/U_∞ 0.93% for the U_z/U_∞ and 1.37% for the U_y/U_∞. Comparing to the GCI values between the medium and the fine grid it is found to be 0.34% for the U_x/U_∞ , 0.63% for the U_z/U_∞ and 0.36% for the U_y/U_∞. The differences between the medium and the fine grid are smaller and adequate for the numerical results. Finally, the medium grid is selected for this study.

7.3 Results and discussion

7.3.1 Flow field results and code validation

Initially, the flow over a cubical building without concentration dispersion is simulated. The present results are compared against the full-scale SILSOE cube experiments that were conducted by the Hoxey, et al. [172] and the LES results of SILSOE cube reported by Richards, et al. [28]. This comparison is based on the velocity flow patterns and pressure coefficient distribution around the cube. The averaged flow fields on the symmetry plane (in the form of streamlines), where the roof reattachment occurs on the roof, a recirculation

zone windward of the cube and the recirculation zone downstream of the cube exist, shown in Figure 7-3.
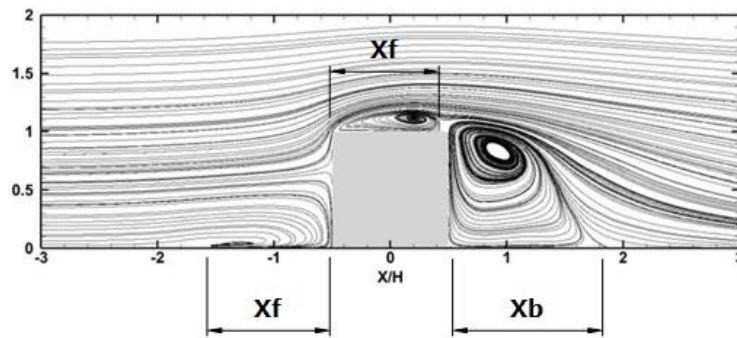
a)

Figure 7-3 Streamlines of the mean flow on the symmetry plane, for a) present results, B) characteristic separation lengths

The calculated lengths of the main separation regions are: X_f for the upstream of the cube, X_b for the downstream and X_r for the roof. They are illustrated in Figure 7-3 and compared in Table 7-1.

Table 7-1 Main separation point lengths

	Case	Upstream separation X_f	Roof reattachment X_r	Down-stream reattachment X_b
Hoxey, et al. [172]	Full Scale experiment	0.75	0.57	1.4
Richards, et al. [28]	LES	0.9	0.9	≈1.4
Present results	LES	0.99	0.9	1.37

As the flow approaches the leeward surface of the cube from the roof, the main separation vortex appears. In the front corner of the cube with the ground and in the corresponding side corners a horseshoe vortex [189] is formed which has its head in the front corner (forming a recirculation zone there) and its legs in the corresponding side corners are binding the cube. The upstream recirculation zone is found experimentally to extend to $X_f = 0.75$ H [172]. The present study overestimates this zone which is found to be $X_f = 0.99$ H, is in good agreement with the LES results of Richards, et al. [28]. Moreover, the computed length of

the separation zone on the roof of the cube, $X_r = 0.9 \, H$, is found to be exactly the same with that predicted by Richards, et al. [28], as well as the flow behaviour there looks almost the same. This predicted reattachment length is found to be higher than the experimental value of $X_r = 0.57 \, H$. The down-stream of the cube recirculation zone is similar for all the different cases studied with an approximate value of the reattachment length $X_b \approx 1.4 \, H$. The flow field behind the cube could be separated into two different zones: the cavity zone with low velocities and high turbulence [190] and the near-wake zone after the cavity. The velocity profile at the inlet point A is illustrated in Figure 7-4 and it is compared with the log-law velocity profile of Equation (7-3). The two profiles are in good agreement. In order to validate the flow behaviour around the cube, the pressure coefficient which is defined by the equation (5-2) is calculated.

The pressure coefficient profile around the SILSOE cube is illustrated in Figure 7-5. It is found that the present results are in good agreement with experimental data of Richards, et al. [15].
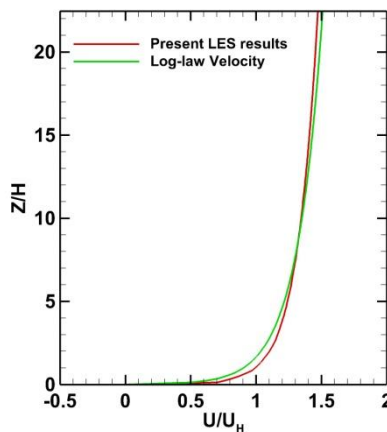
Figure 7-4 Inlet velocity distribution
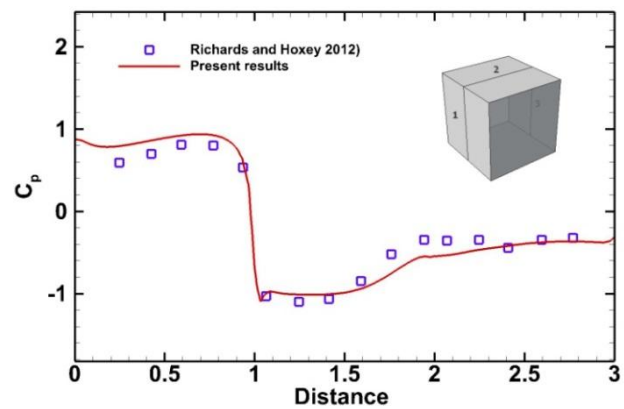
Figure 7-5 Pressure coefficient distribution around the cube's surfaces

Figure 7-6 shows the non-dimensional, spectra at position (-1H, 0, 0.09H) where the -5/3 Kolmogorov law (in non-weighted representation) is found to be applied.
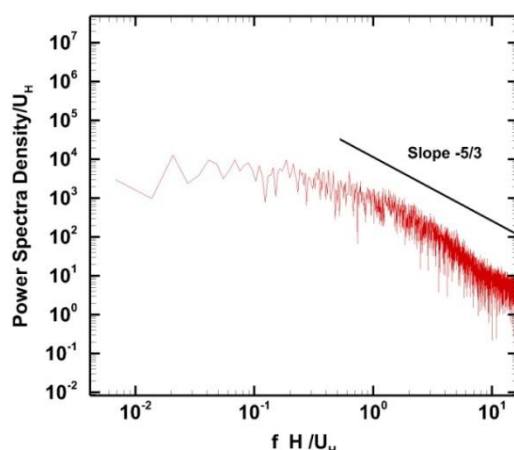
Figure 7-6 Normalized spectrum

7.4 Hazardous dispersion

A fire source in the near wake of the cube produces large wind fluctuations and non-uniform distributions of exhaust gases. The pool fire is considered here as a local heat and chemical species source that is affecting the density of the air. Even though the produced thermal plume results in strong buoyancy forces, its effect on the size of cavity zone is small due to its locality. The size of the recirculation zone for the different pool studied changed comparatively very little. For the crude oil pool fire, the recirculation zone is found to be X_b=1.31 and for the diesel pool fire is found X_b=1.285. The buoyant forces cause a small decrease in the recirculation zone and an increase of the height of the cavity zone. These results are in agreement with Olvera, et al. [55] studies. Brzoska, et al. [206] similarly observed that when the plume extent is within the recirculation zone, its size is not affected drastically and it is independent of the source location.

The present numerical results of the smoke dispersion around the cube are validated against the Tominaga, et al. [16] experimental data, which are obtained in the wind tunnel of the Institute of Industrial Science at the University of Tokyo. This wind tunnel experiment employs mixtures of different gases such as C_2H_4 (neutral), He and C_2H_4 (light) and SF_6 and C_2H_4 (heavy gases) for the study of the dispersion around a cubical obstacle. The mixture release point is

126

located at the position X/H=0.5, behind the cube and within the recirculation zone. The light gas is considered to play the role of a thermal plume. The comparison of the smoke dispersion of the diesel's pool fire with the aforementioned experimental data is shown in Figure 7-7. The numerical results of the non-dimensional concentration of the diesel pool fire accident are comparing well with the dispersion of the light gas experimental data at the position D (X/H=2).
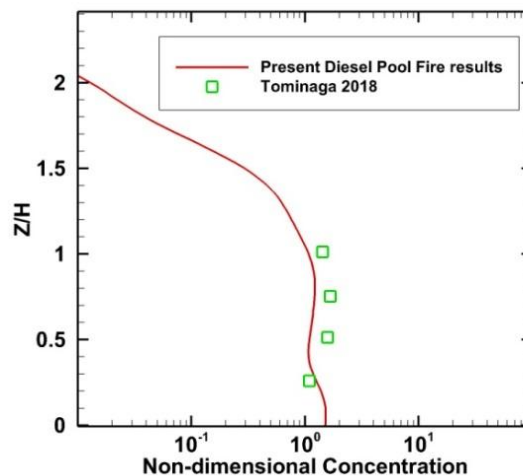
Figure 7-7 Profiles of the non-dimensional mean concentrations of the total products of the fire behind the building at the D position against the experimental data of Tominaga, et al. [16]

Figure 7-8 shows the time average smoke concentration at positions B, D and E at X/H=1, 2, 3, respectively with important differences in the profiles. The smoke concentration just above the source (point B) has a similar distribution for both accidents. At position, D and E, the smoke concentration distribution shows important differences between crude oil and diesel oil cases. In both cases, the plume spreads with the distance away from the source. At the fire point B and at height Z/H=0.2, the smoke concentration for the diesel pool fire is 9 times higher than the crude oil fire. For the same height at point D, the diesel pool fire concentration is 1.72 times higher than that of crude oil fire, while at point E is 1.56 times higher. These differences in the smoke mean concentration are

primarily due to the fact that diesel pool fire produces higher amounts of smoke and secondary to the turbulence dispersion of the pollutant smoke.

Figure 7-9 shows the profiles of the time average smoke concentration (mg/m^3) at the different heights of Z/H=0.33, 0.5 and at the cube's height at Z/H=1.

a)   b)   c)
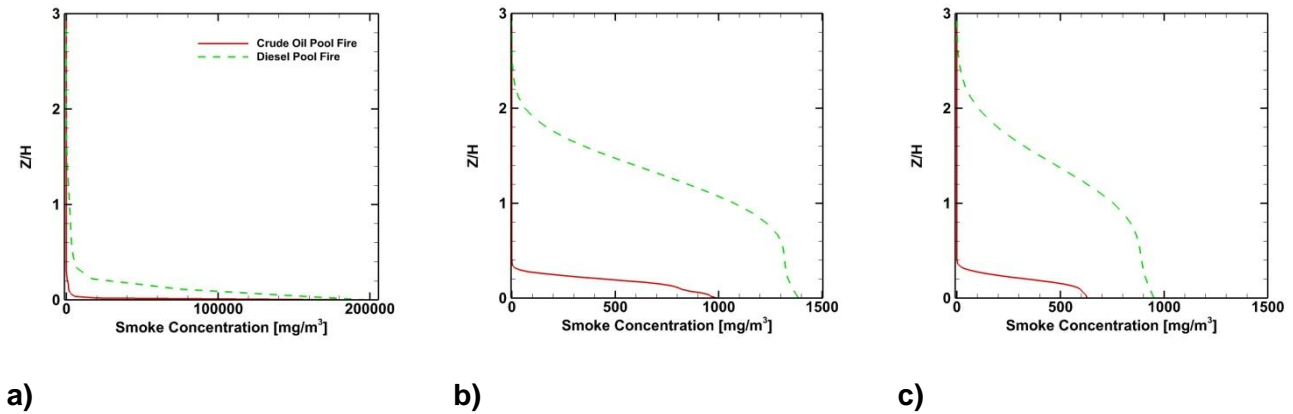
Figure 7-8 Time average smoke mean concentration profiles (mg/m^3) at : a) B, b) D and c) E positions

a)   b)   c)
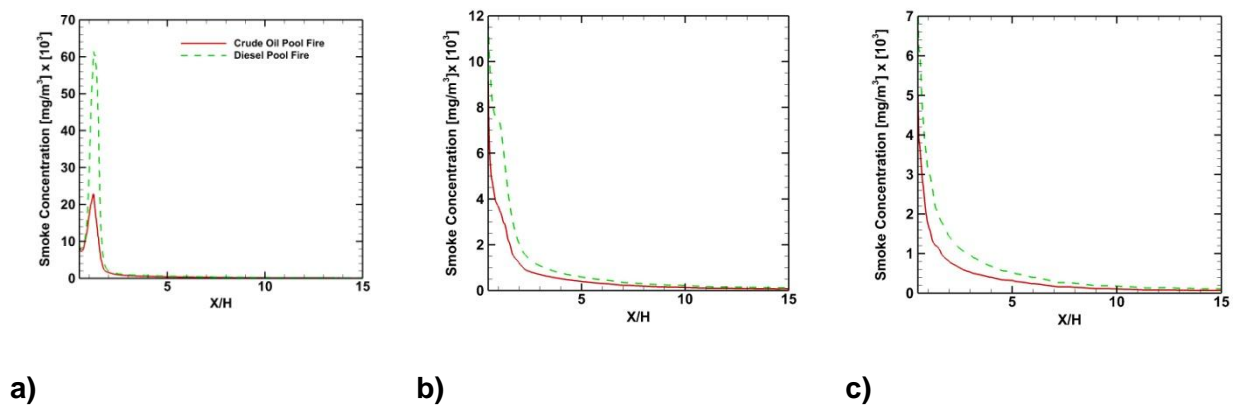
Figure 7-9 Time average smoke concentration profiles (mg/m^3) at a) Z/H=0.33, b) Z/H=0.5m, and c) Z/H=1 heights

In order to study the mechanism of smoke dispersion inside the wake zone the convective and turbulent mass fluxes are examined for the LES results. The definition of the time average filtered convective mass flux in the x direction is defined as $q_{x,convective}=<\tilde{u}_x><\tilde{c}>$ and for the z direction, $q_{z,convective}=<\tilde{u}_z><\tilde{c}>$.

Similar, the definition of the time average mass turbulent flux in the x direction is defined as $q_{x,turbulent} = <\widetilde{u_x'}\,\widetilde{c'}>$ and for the z direction, $q_{z,turbulent} = <\widetilde{u_z'}\,\widetilde{c'}>$, where $\widetilde{u_x'}$, $\widetilde{u_z'}$ and $\widetilde{c'}$ are the resolved fluctuations [192]. In order to express the non-dimensional form, the reference mass flux is defined as [192]:

$$q_0 = C_0 U_H \qquad\qquad \textbf{(7-7)}$$

and the reference concentration is given as:

$$C_0 = \frac{Q_e}{H^2 U_H} \qquad\qquad \textbf{(7-8)}$$

Where Q_e is the pollutant exhaust rate.

The non-dimensional convective mass flux of the crude oil smoke's plume fire in the x direction ($q_{x,\,convective}/q_0$) is shown in Figure 7-10a and for the z direction ($q_{y,\,convective}/q_0$) in Figure 7-10b. Similarly, the turbulent mass flux in the x-direction is shown on Figure 7-11a and for the z-direction is shown on Figure 7-11b. Because of the similarity between the crude oil fire and the diesel pool fire non-dimensional results, only the crude oil fire results are shown.

As shown in Figure 7-10a, the convective mass flux, at the symmetry plane is mainly convected towards the leeward face of the cube due to the negative velocity created into the cavity zone behind the cube. In the same plane, the vertical exhaust velocity of the smoke's plume creates a positive convective mass flux, which is limited inside the recirculation zone behind the cube.
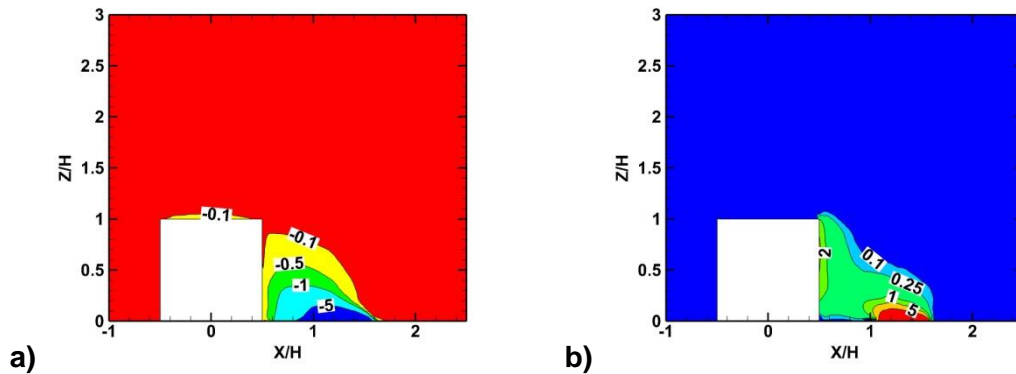
Figure 7-10 Non dimensional time averaged convective mass flux on the symmetry plane for the crude oil fire for a) the x-velocity component ($q_{x,\text{convective}}/q_0$) and b) the z-velocity component ($q_{z,\text{convective}}/q_0$)

As shown in Figure 7-11, the non-dimensional turbulence mass flux is significant in the wake zone and influences the smoke dispersion.

This amount of smoke is trapped inside the cavity due to recirculation of air. The negative velocity values inside the cavity zone in the x-direction transport the plume towards the leeward face of the cube for both cases.
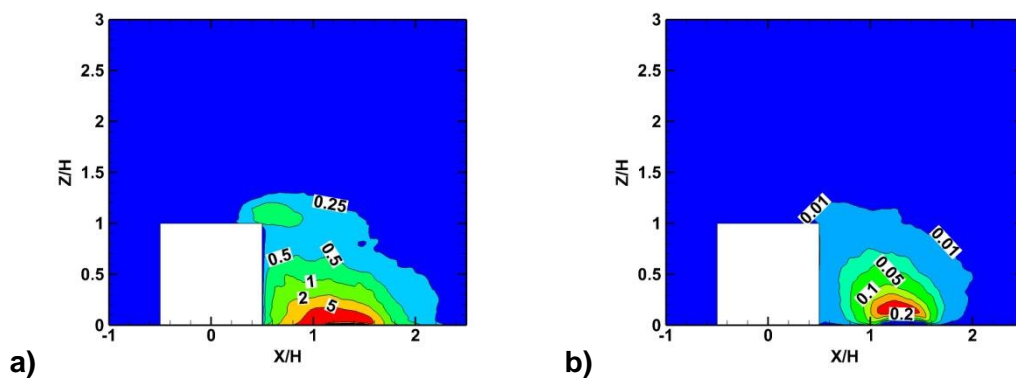
Figure 7-11 Non dimensional time average turbulent mass flux on the symmetry plane for the crude oil fire for a) the x fluctuation component ($q_{x,turbulent}/q_0$) and b) the z-velocity fluctuation component ($q_{z,turbulent}/q_0$).

7.5 Toxic zones

Risk zones cover accidents of heat flux and toxic substances in case of fire. A risk zone is a semi-spherical area which has as a center the point of the source emission and it extends to the limit where safety is valid. In order to define a risk zone, the smoke level concentration (mg/m^3) should be defined. Different zones can be defined [207]:

a. Zone I - Very Serious Consequences (LC50 region) where the possibility of death population is 50% due to inhalation of a toxic substance.

b. Zone II - Serious Consequences (LC1 region) where the possibility of death population is 1% due to inhalation of a toxic substance.

c. Zone III - Moderate Consequences (IDLH region) and reversible injuries following the inhalation of a toxic substance. The area out the Zone III is the safe area.

The values of the safety limits of the smoke pollutants are defined by the National Institute for Occupational Safety and Health (NIOSH) and for the LC1 is 25,000 mg/m^3, and for the IDLH is 2,500 mg/m^3.

Figure 7-12, Figure 7-13 and Figure 7-14 show the safety limit zones for the two accidents studied here 200 sec after the start of the accident. The red color defines the boundaries of LC1 zone, while the blue color indicates the boundaries of IDLH zone.

The iso-surfaces of LC1 and IDLH zones allow us to visualize the three-dimensional distribution of the hazardous released material after the accident start. In all cases, it is found that the hazardous material is transported by the buoyant plume and spreads towards the leeward face of the building. In both cases, the wake zone remains almost the same and the LC1 and IDLH toxic zones are limited within this zone. As the phenomenon evolves, the toxic zones still remain within the wake zone of the cube and small differences can be observed.

a)   b)
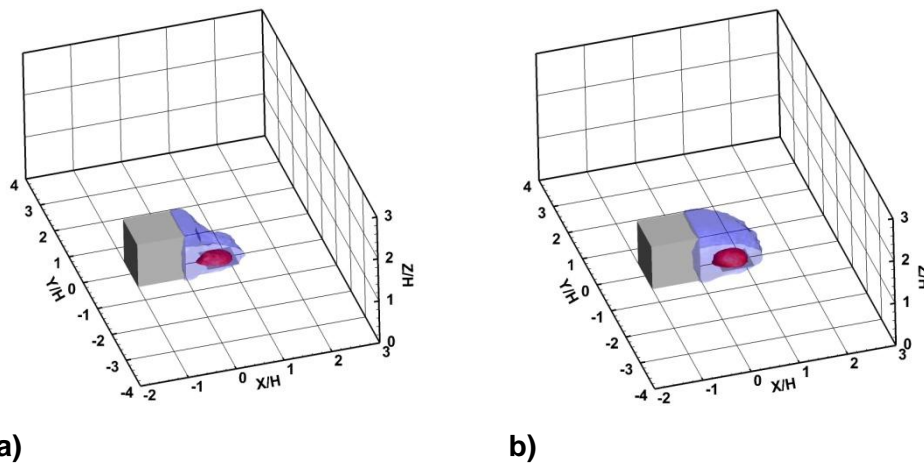
Figure 7-12 Iso-surfaces of the mean smoke concentration (mg / m^3) of the LC1 and IDLH zones for : a) Case 1, and b) Case 2 at t= 200 sec after the accident

Figure 7-13 illustrates the LC1 and IDLH zones on the symmetry plane for both accidental cases based on the mean smoke concentration. It is clear that after the fire accident the smoke is driven towards the leeward face of the cube and mainly is the IDLH zone that affects the surface of the cube. A large portion of the smoke plume is trapped inside the recirculation zone and both accident scenarios have almost the same toxic zone sizes. However, the dilution level inside the wake zone is not the same. In the diesel pool fire case with larger smoke production the IDLH zone covers all the wake zone area.

a)   b)
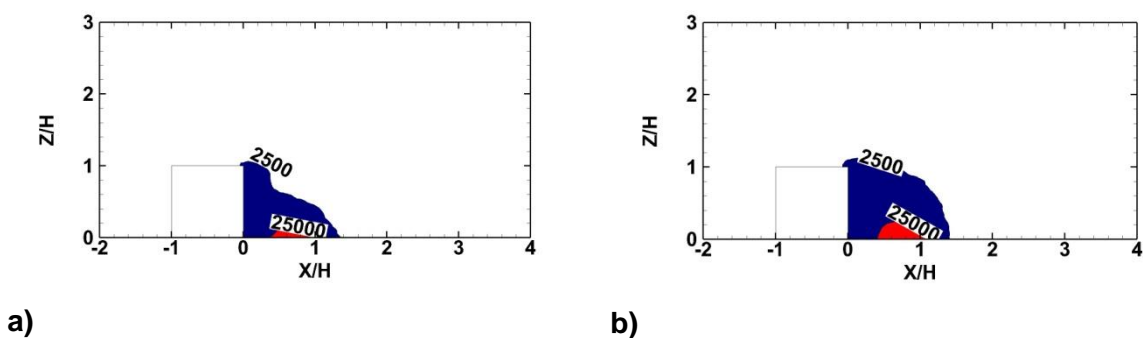
Figure 7-13 Iso-surface of smoke concentration (mg / m^3) of the LC1 and IDLH zones for: a) Case 1, and b) Case 2

Figure 7-14 illustrates the IDLH and LC1 zones at the Z=1m and 3m horizontal planes for Case 1 and 2. Case 1 shows an significant IDLH zone area inside the

cube's cavity zone, which is getting smaller at higher levels (Figure 7-14a,b). Case 2 shows a significant smoke concentration at the height Z/H=1 (Figure 7-14c) with both IDLH and LC1 zone areas limited within the cavity zone. At a higher level, Z/H=3, only IDLH zone appears to have almost the same extent (Figure 7-14d).

a)   b)

c)   d)
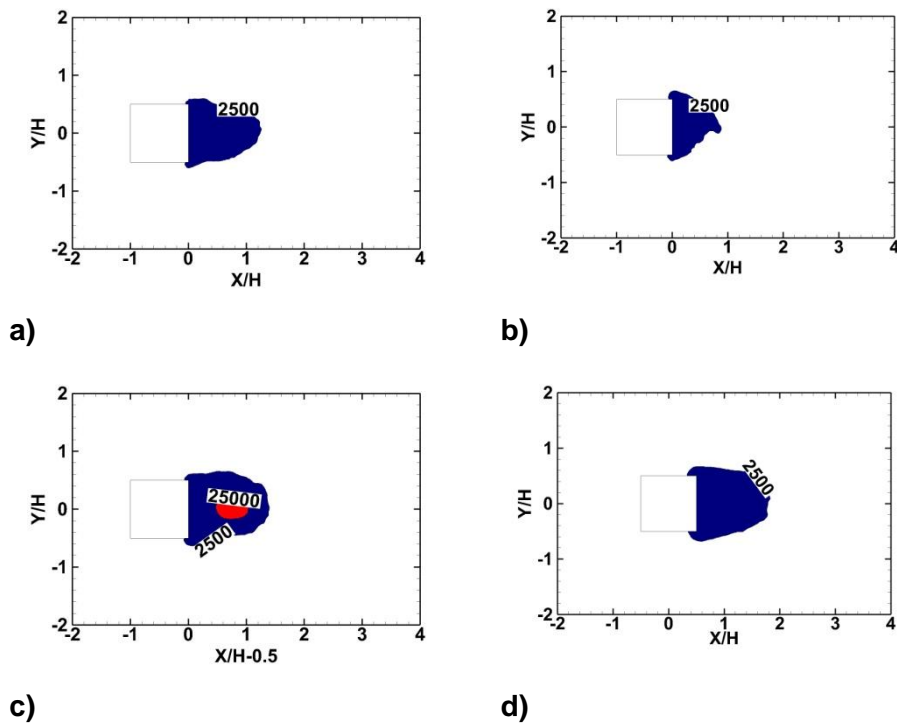
Figure 7-14 Iso-surface of the mean smoke concentration (mg/m^3) of the LC1 and IDLH zone for Case 1 on a) Z=1m plane and b) Z=3m plane and for Case 2 on c) the, Z=1m plane and d) Z=3m plane.

7.6 Simplified Risk Map generation for an isolated building

Managing the risks of the smoke dispersion after a fire accident is crucial for the fire fighting mitigation plan. The visualization of these risks could be illustrated with graphic representations such as charts, maps, visual metaphors and diagrams, making the firefighting decision to better react with the risk's accident management [208]. Horwitz, et al. [209] in their study mentioned that the understanding of risk is defined by the risk visualization. A risk map is an essential tool for the visualization of the risk characteristics over a given area. It defines the combination of the hazards and the vulnerabilities over an area and

offers a representation of all the possible risks. It includes details which can define the best strategy for effective mitigation plans [210, 211].

Different researchers study the developed hazard models for a specific region based on the physiographic or environmental factors, specially for wild fire models with Geographic Information System (GIS) methods [212-214]. The combination of multi-criteria methods with GIS systems could result in the production of fire risk maps [215]. These risk maps could be the guide for strategically driven decisions [216].

A multi-criteria risk map is composed from different layers of data. An example of a risk map defining the toxic zones after a fire accident in an urban environment is shown in Figure 7-15. The different layers which are composing this risk map are defined from the following layers: (1) the GIS Urban Geometry layer: Collection of satellite images and urban geometrical characteristics, (2)the Wind flow distribution: the wind flow distribution inside the urban environment calculated with CFD methods, (3) the Temperature distribution Layer: The temperature layer calculated with CFD methods, (4) the Smoke dispersion Layer: The smoke dispersion is calculated with Lagrangian models, (5) the Toxic Zones Layer: The toxic zones layers are defined with the limits of the smoke concentration.
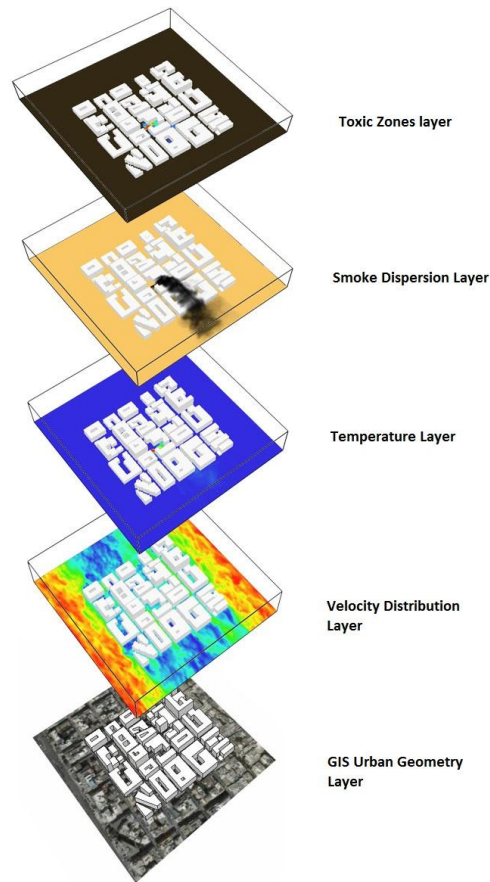
Figure 7-15 Different Layers composing a fire's smoke risk map

Berkowicz, et al. [217] illustrated the Geometry of the recirculation zone inside a street canyon and concluded that the scheme of the recirculation zone forms a trapezoidal cross section. Similar flow patterns are illustrated for the Enugu city street configurations at Akubue [218] research work.

As illustrated in Figure 7-16, the area around the cube is shown in a form of a grid, with cells of H/2 size, indicating the level of importance in encountering the risk of the toxic smoke after a possible fire accident. The point of accident initiation is defined by the red circle, which is located in the wake zone of the cube, marked with yellow. The sides of the cube covered by a flow recirculation (marked with green) demonstrate that special attention is required during intervention. The results of the wind spatial patterns could define the areas that are affected the wind smoke distribution spatial grid pattern layers.
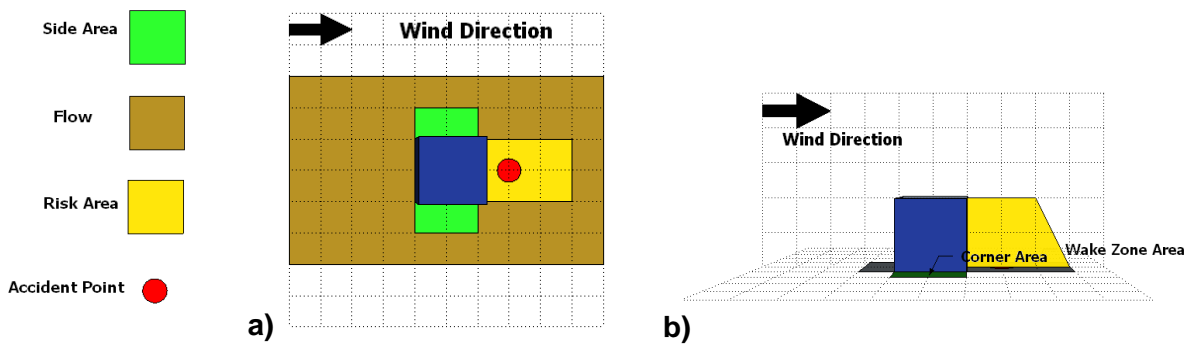
Figure 7-16 Risk Map Generation

7.7 Conclusion

This study examines numerically using the LES method the wind flow and pollutant dispersion around a cube for two different pool fire cases initiated in the cavity behind the cube. The obtained results for the wind flow behavior around a cube are compared against the SILSOE's cube experimental data [14, 15]. The fire pollutant dispersion around the cube is compared well with Tominaga, et al. [16] wind tunnel experiments. It is found that strong buoyancy forces (Richardson number greater of 2) and the turbulent mixing processes determine the boundaries of the toxic zones. The dispersion of the smoke concentration of the diesel pool fire shows important differences compared to the crude oil pool fire. In a Diesel pool fire, local concentrations could reach as much as five times higher values than the crude oil fires.

The size of the wake zone does not change for both the pool fires studied. In the crude oil pool fire, the recirculation zone is slightly longer ($X_b = 1.31$) than that of the diesel pool fire ($X_b = 1.285$). The recirculation zone traps a large portion of the smoke plume in both accidental scenarios, so the maximum extent of the toxic zones is almost the same. However, the dilution inside the wake area is not the same, because the diesel pool fire generates more smoke which covers the entire cavity zone area. As a consequence, the IDLH zone covers almost the entire cavity zone with a small area covered by the LC1 zone.

The mechanism of mass transport of the smoke inside the cavity zone is mainly due to the convective mean mass flux and the turbulence mass flux. The

convective mass flux on the symmetry plane is almost the same for both the accident cases. However, as it is expected, the diesel pool fire accident gives higher concentration levels inside the wake zone compared to the crude oil fire. This is due to that the diesel pool fire generates a higher quantity of smoke than the crude oil fire. The quantity of the smoke is trapped inside the boundaries of the cavity zone by the convective flow of the x and z velocity components.

Large-scale turbulent motion is generated which controls the diffusion of mass and momentum. The mixing of fuel and air is controlled by this relatively slow turbulent mixing process rather than the fast chemical kinetics. The important conclusion that comes out from this study is that defines the toxic zones in order to deal with the fire accident intervention. Even though the fire accidents are presenting different total heat rate releases, the impact of the toxic zones are similar and the intervention method and technique is similar for the studied atmospheric conditions.

CHAPTER 8. Diesel pool fire incident inside an urban street canyon

This chapter focuses on the numerical study of a diesel pool fire accident inside a street canyon using the Large-eddy Simulation method.

The results of this numerical study are compared fairly well against experimental data. Cases with different inflow wind speeds are studied and the risk zones are defined for different wind approaching scenarios. The results show that part of the fire pollutants exits the canyon, while another part is trapped into the canyon due to the local air recirculation. The buoyancy effect due to the fire accident and the inertial effect of the wind flow define the pollutant's dispersion. When the wind velocity at the street canyon height exceeds a critical value, the fire pollutants are recirculated and trapped inside the street canyon. This dispersion is analysed based on the flow characteristics in the street canyon.

8.1 Introduction

The flow inside a street canyon, which is the smallest urban unit, and the pollutant fire dispersion are studied with a Large-eddy Simulation method.

An accident with a fire inside a street canyon could be characterized as a bottom heated case and the flow patterns are complicated. Several RANS k-epsilon model studies examine the flow inside a street canyon with a bottom heating [86, 87]. But few research report a fire inside a street canyon [88, 89].

A small number of analyses focus on the fire study inside a street canyon using the FDS code [89, 92, 93]. Other studies focus on codes comparisons inside a street canyon [80]. A pool fire accident could be a possible urban accident and several studies for a pool fire accident in an open space exist [6, 9, 95-99].

This chapter uses the FDS code in order to analyse this type of flow and define the toxic zones in a street canyon accident.

8.2 Computational domain

8.2.1 Flow field description

The present computational field is shown in Figure 8-1, where H is the height of the building's height and W is the width of the street canyon. The distance between the two buildings is kept constant at H/W=1. The building's height is considered to be 40m.

The diesel pool fire is pool located at the middle of the street canyon with a 3m diameter. The present simulations are validated against the Baik, et al. [62] experimental results that were conducted in an open field environment in a fully turbulent flow with Reynolds's number equals to Re= 20×10^{6}, based on the height H of the cube, a value that is also kept in our simulations.
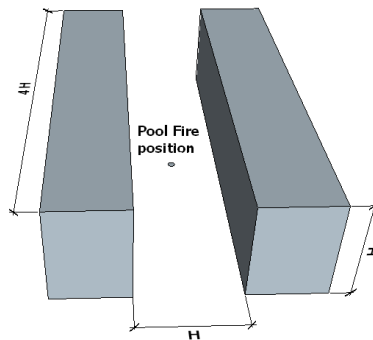
Figure 8-1 Computational domain

The flow field inside the street canyon is characterised by different vortices as it is shown in Figure 5-18. The mean flow detached on the top of the leeward building forming the top vortices. A horseshoe vortex is formed at the base of the leeward building and it is extended to the windward building. Side vortices are formed at the two sides of the leeward building. These vortices are entering inside the street canyon and influence the flow characteristics inside the canyon. A primary vortex is formed inside the canyon and is the main reason for the smoke products dispersion. Finally, a wake vortex is formed behind the windward canyon. The Canyon vortex brings the fire products toward the leeward buildings and then upward to the roof level. The smoke products

pollutants may either be ventilated from the street canyon and escape at the roof level of the buildings or re-circulates inside the street canyon.

8.2.2 Boundary conditions

Appropriate inlet conditions are applied [72]. The perpendicular velocity distribution at the inlet boundary condition is defined as:

$$U_0 = U_{ref} \left(\frac{z}{z_{ref}} \right)^{0.299} \tag{8-1}$$

where z_{ref} = 40m is the reference value at the street canyon building and U_{ref} is the velocity at this height. The top and the other three sides are set as open boundaries.

The behaviour of a 3m diesel pool fire is experimentally studied in the Chatris, et al. [97] experiment. The diesel's characteristics are: the density (at 15 ^{o}C) 820-860 kg/m^3, the boiling point is 250-370 ^{o}C and the kinetic viscosity (at 40 ^{o}C) is 2.0 - 4.5 mm^2/s. The mass loss $\dot{m}''$ and the total heat release rate $\dot{q}$(HRR) are calculated by the equations (7-1) and (7-2) [198] :

According to the experimental results the mass burning rate of the diesel pool fire is about 0.045 kg/sec m^2. Flame temperature varies between 40 ^{o}C and 1200 ^{o}C, while the total heat release rate $\dot{q}$ (HRR) is 13.5 MW. The diesel oil is composed of 75% saturated hydrocarbons and 25% aromatic hydrocarbons. Walton, et al. [200] assumed that the smoke yield varies between 15% and 20% for the diesel oil. A smoke yield average 17.5% is used [6].

This diesel pool fire experiment was numerically studied by Vasanth, et al. [219] by using a 2D model and applying four different RANS models. The pool fire release is simulated by a mass inlet from a circular source. A power law equation is applied for the inlet velocity which caused a tilt to the fire. The standard k-epsilon model has as maximum exhaust velocity equal to 17.83 m/sec and maximum exhaust temperature equal to 1746 K.

8.2.3 Numerical details

An explicit predictor-corrector finite difference scheme is applied, which is second order accurate in space and time. The Poisson equation for modified pressure is solved in every time step by a direct FFT-based solver. The flow variables are updated in time using an explicit second-order Runge-Kutta scheme. The convective terms are upwind-biased differences in the predictor step and downwind biased differences in the corrector step. The thermal and material diffusion terms are pure central differences, with no upwind or downwind bias, thus they are differenced the same way in both the predictor and corrector steps. FDS uses a structured staggered grid with the immersed boundary method (IBM) for the treatment of the flow obstruction [220].

8.2.4 Mesh type

The mesh plays an important role for the code accuracy. The characteristic grid size is defined from the equation [221] :

$$D^* = \left(\frac{Q}{\rho_\infty c_p T_\infty \sqrt{g}} \right)^{2/5} \tag{8-2}$$

where, c_p is the specific heat, T_∞ is the ambient air temperature, ρ_∞ is the ambient air density, g is the gravity and Q is the heat rate release, and the grid size is set as D^*=0.273 m, applied uniformly in the computational domain. The total number of cells in the simulations is up to 5,125,000 and the flow of air and fire dispersion last for 200 s.

8.2.5 Grid Resolution

The grid sensitivity is examined with the grid convergence index (GCI) as escribed is section 7.2.6. A coarse grid consistent of 3,416,660 cells, a medium grid of 5,125,000 cells and a fine grid of 7,684,500 cells are compare. The refined factor between the grids is r=1.5. The grid sensitivity is examined in the middle position of the street canyon where the pool fire accident is taken place. The GCI values are tested for the U_x/U_{ref} distribution.
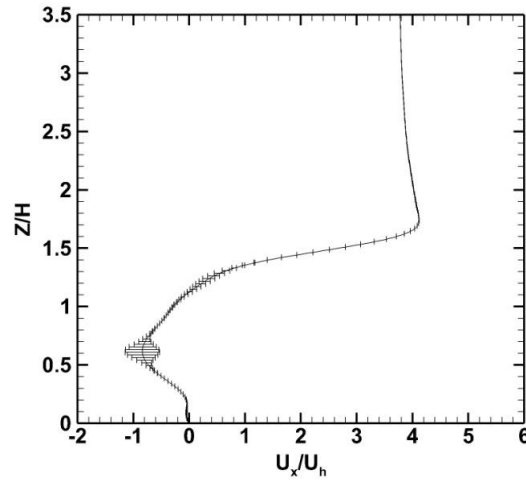
Figure 8-2 The non-dimensional U_x mean velocities for the medium grid to the fine grid with the GCI error bars between the fine and medium grid.

The GCI values between the coarse and the medium grid are for the U_x/U_∞ is 2.84%, for the U_z/U_∞ is 1.23% and for the U_y/U_∞ is 1.89%. Comparing to the GCI values between the medium and the fine grid it is found that for the U_x/U_∞ is 0.54%, for the U_z/U_∞ is 0.89% and for the U_y/U_∞ is 0.75%. The differences between the medium and the fine grid are smaller and adequate for the numerical results. Finally, the medium grid is selected for further study.

8.2.6 Flow field results and Validation

Large-eddy Simulations (LES) are performed by the FDS code for a diesel pool fire accident inside a street canyon. Results from the present model are compared against the experimental data of Baik, et al. [62] in terms of velocity distribution as are shown in Figure 8-3a and b for the velocity distributions at the positions X/H=0.15 and 0.75, respectively. The agreement between the numerical and experimental results is fairly good.
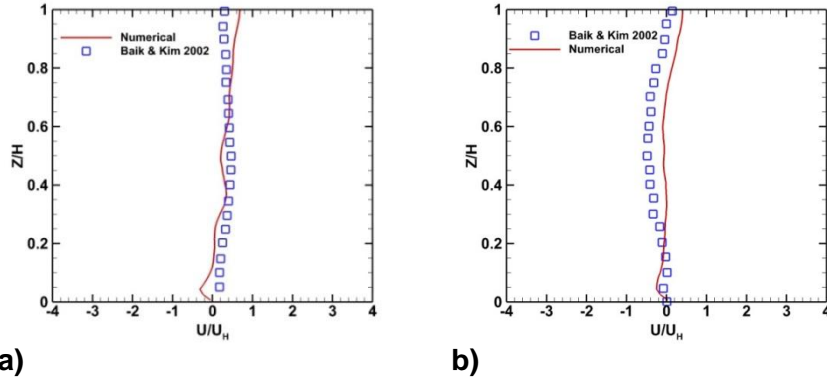
Figure 8-3 Mean velocity normalized by U_{ref} **the locations a) X/H=0.15 and b) and X/H=0.75**

In order to investigate the toxicity and the safety limits of the fire incident inside the street canyon, the smoke's products dispersion inside the street canyon is studied. A power-law velocity profile is applied in the inlet for three different velocity magnitudes at the reference height which is the 10m above the earth. So, Case 1 has U_r=2.5 m/sec, Case 2 has 5 m/sec and Case 3 has 7.5 m/sec at 10 meters height. The power-law velocity profile yields inflow wind speeds of 3.78 m/sec, 7.56 m/sec and 11.35 m/sec at the building's roof level, respectively.

8.3 Buoyancy forces

In case of a fire accident at the middle point of a street canyon, the buoyancy forces play an important role for the smoke distribution due to the thermal upward moving. On the other hand, the wind flow, with the inertial forces acts against the buoyancy forces and trap the fire pollutants inside the street canyon. The velocity profile of the incoming wind is crucial for the smoke pollutant distribution. The Richardson number describes the ratio of the thermal buoyancy forces to the wind convection forces at the street canyon's rooftop. The diesel pool fire presents a Richardson number with value 1.41 for the Case 1, a value 0.356 for Case 2 and a value 0.126 for Case 3. The elevated Richardson number for Case 1 shows that, the buoyancy forces are important and the mixing between the smokes products and the air is minimized. The

143

Richardson number for Case 2 and 3, shows that the buoyancy forces are not so important and that the smoke plume is trapped inside the street canyon.

8.4 Flow characteristics

Figure 8-4 shows the streamlines of the non-dimensional velocity distribution for Case 1, Case 2 and Case 3. Important differences exist between the three cases. This is due to the interaction of the buoyancy and inertial forces inside and outside the street canyon.

Case 1 presents a movement of the flow towards the leeward building (Figure 8-4a). Case 2 presents a movement of the flow towards the windward building and an important recirculation zone between the windward building and the middle point of the canyon. This influences the flow and traps an important quantity of the smoke inside the canyon (Figure 8-4b). Finally, Case 3 presents a similar flow at the upper limit of the canyon's height but it also presents a secondary recirculation zone at the low level corner of the windward building (Figure 8-4c) which produces an important mixing of the smoke products. Comparing the streamlines of the three cases with the streamlines of a canyon without a fire inside, it is evident that the main canyon vortex is displaced from the centre of the canyon into the upper part of the canyon. As a result the canyon vortex does not play an important role for the smoke mixing but for the trap of the smoke inside the canyon.

a)   b)   c)
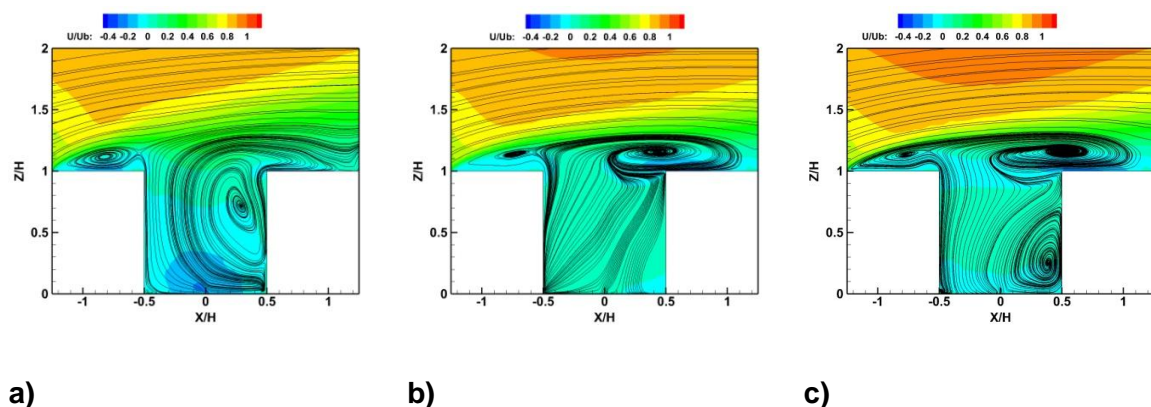
Figure 8-4 Mean x-velocity normalized by U_{ref} at the symmetry locations for a) Case 1, b) Case 2 and c) Case 3.

In order to detect the vortical flow structure, the Q criteria is simulated. Figure 8-5 shows the three-dimension view of the Q criteria at the constant value of 0.1 $1/sec^2$ for Cases 1, 2 and 3. The positive values of Q criteria show the vertical flow structures. All cases present a horseshoe vortex at the bottom area of the leeward building. As the incoming velocity is higher, the horseshoe vortex presents a higher extension towards the steam-wise flow. The presented vortices in the wake of the canyon are similar for all the cases. Important vortex structures are generated inside the street canyon which is similar for all the different cases. The local shear layer between the cavity zone and the incoming air creates a significant local shear layer at the roof of the building's canyon. As shown on Figure 8-5a and Figure 8-5b, the created vortices are similar for Cases 1 and 2, but differ from those of Figure 8-5c.

a)   b)   c)
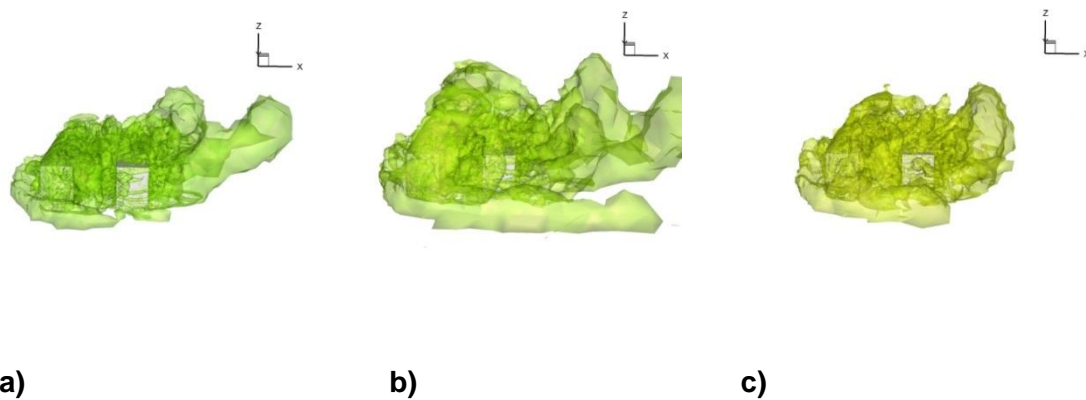
Figure 8-5 Isosurface of the Q-criterion at a constant value 1 for a) Case 1, b) Case 2 and c) Case 3

8.5 Hazardous dispersion

The fire source is in the centre of a street canyon and produces large fluctuations and non-uniform distributions in the exhaust gases source concentrations. The thermal plume produces important buoyancy forces. But it is the wind inertia forces at the canyon's height that finally defines the smoke's distribution inside the street canyon due to the complex flow that it produces. The size and the position of the fire, combined with the important buoyancy forces define the smoke distribution inside the canyon.

The mechanism of the smoke dispersion inside the street canyon is defined by the convective mass flux and the turbulent mass flux. The convective mass flux for the diesel pool for the x and z direction is shown in Figure 8-6 and the turbulent mass flux is shown in Figure 8-7 for Cases 1,2 and 3 at the symmetry plane. The mean molecular mass flux is neglected. The pool fire accident presents high smoke concentration levels inside the street canyon area, due to the fact that the smoke is trapped between the buildings inside a recirculation movement.

For Case 1, the time average convective mass flux in x direction, $q_{x, convective}=<\tilde{u}_x><\tilde{c}>$, presents a movement of the convective flux towards the leeward building and elevated values around the fire source (Figure 8-6a). On contrary Case 2 presents a movement of the time average convective flux towards the windward building (Figure 8-6b). Finally, Case 3 shows that the time average convective mass flux is almost homogenous in the entire field inside the canyon (Figure 8-6c).

The vertical exhaust of the smoke plume creates positive values for the time average convective mass flux in z direction, $q_{z, convective}=<\tilde{u}_z><\tilde{c}>$ for all cases. Depending on the velocity at the canyon's height the mean convective mass flux changes direction. As shown in Figure 8-6 d,f , Cases 1 and 3 present a movement of the mean convective mass flux direction towards the leeward building and for Case 2 towards the windward building (Figure 8-6 e). Only Case 1 presents convective mass flux that comes out of the canyon's height.

a)   b)   c)
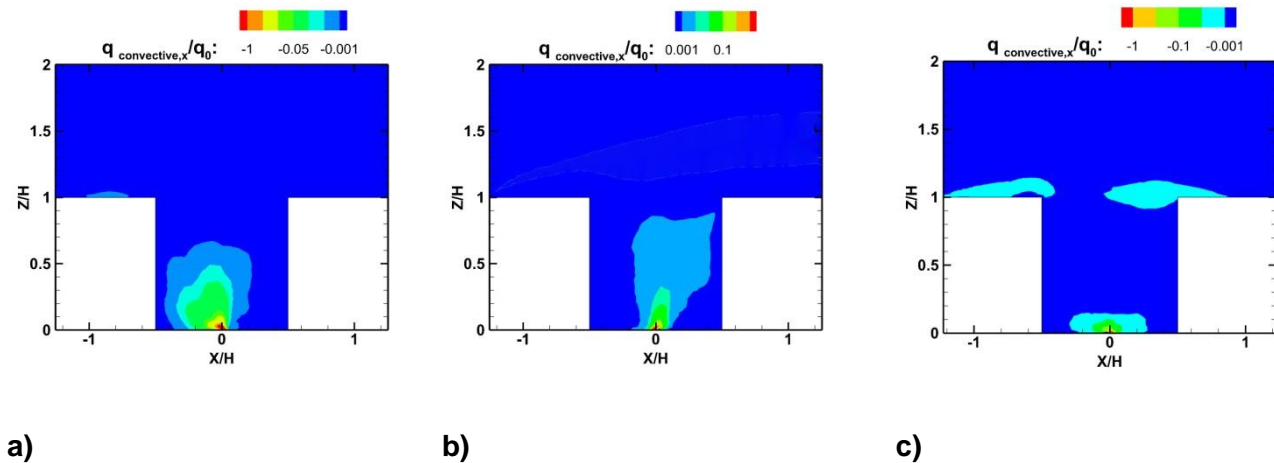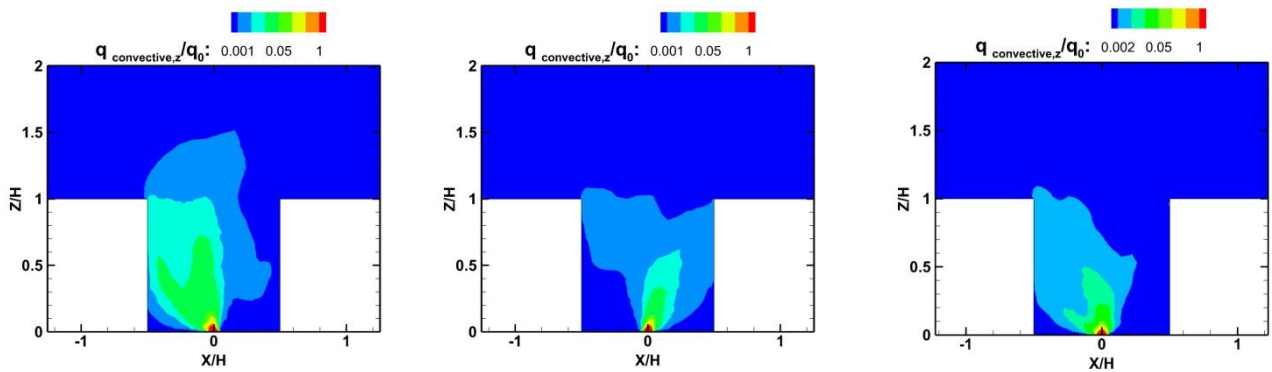
d)   e)   f)

Figure 8-6 Time average non-dimensional convective mean mass flux of the smoke release at the symmetry plane for the X velocity component for a) Case 1, b) Case 2 and c) Case 3 and the and the Z velocity component for d) Case 1, e) Case 2 and f) Case 3.

The time average turbulence concentration flux in x direction, $q_{x,\,turbulent} = <\widetilde{u_x'}\widetilde{c'}>$ for Case 1 (Figure 8-7a) presents a movement towards the leeward building of the canyon. For Case 2 (Figure 8-7b), it presents a movement towards the windward building of the canyon, and for Case 3 it presents an homogenous distribution in the canyon's cavity (Figure 8-7c). As shown in Figure 8-7d,e,f the time average turbulence concentration flux in the z direction $q_{z,\,turbulent} = <\widetilde{u_z'}\widetilde{c'}>$ is similar respectively and diffuses the smoke plume in the vertical and lateral direction.

a)   b)   c)

d)   e)   f)
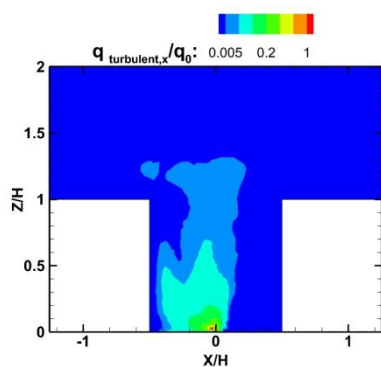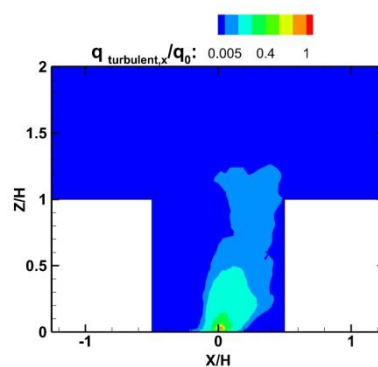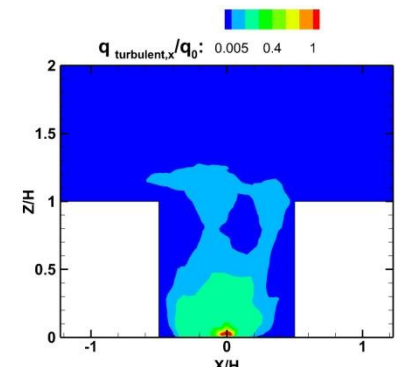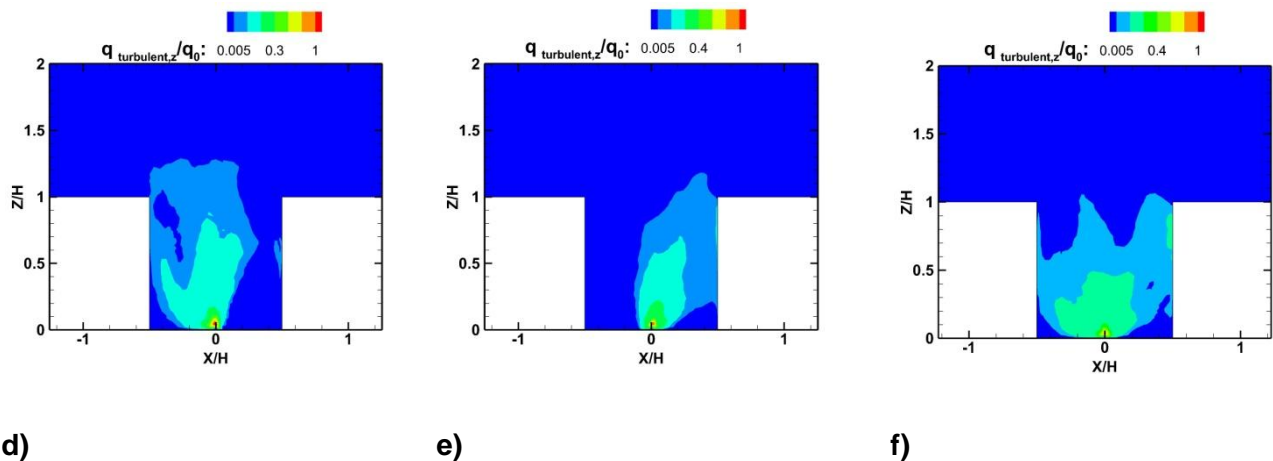
Figure 8-7 Time average non-dimensional turbulence mass flux of the smoke release at the symmetry plane for the X velocity component for a) Case 1, b) Case 2 and c) Case 3 and the and the Z velocity component for d) Case 1, d) Case 2 and f) Case 3.

In Figure 8-6 and Figure 8-7 present a balance between the convective and the turbulence concentration fluxes is observed. The turbulence concentration fluxes are higher than the convective ones. The convection action defines the plume movement towards the leeward or windward building.

8.5.1 Smoke dispersion

The three different smoke plume patterns after 200 sec are presented in Figure 8-8 for the three different inlet profiles. In Case 1, the smoke plume is driven to the leeward building and then arises and reaches at the top of the street canyon as is shown in Figure 8-8a. In Case 2, the smoke in driven leeward the building, then arises at the top of the street canyon and part of the smoke is released outside the canyon and part of the smoke is recirculated inside the canyon as is shown in Figure 8-8b. Finally in Case 3, Figure 8-8c, the smoke is driven leeward the building, rises up to the street canyon and recirculates back into the canyon as Figure 8-8b shows.

148
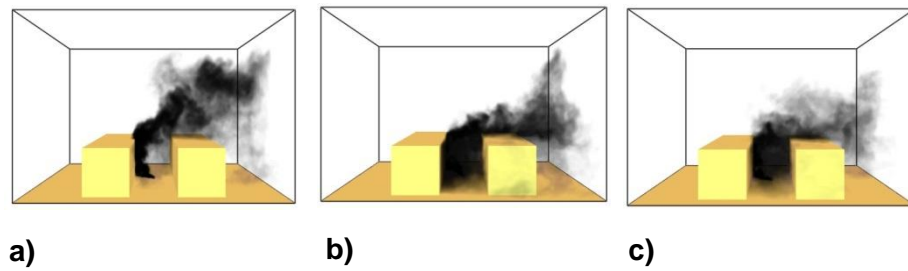
Figure 8-8 Dispersion for fire products for different wind velocities at the building's height a) Case 1 with $U_r = 2.5 \dfrac{m}{\sec}$ **, b) Case 2 with** $U_r = 5 \dfrac{m}{\sec}$ **and c) Case 3 with** $U_r = 7.5 \dfrac{m}{\sec}$ **.**

The vortex inside the street canyon [222, 223] as shown in Figure 5-18 is responsible for the channelling of the smoke products along the street canyon. As it is shown to Figure 8-8, the smoke disperses towards the leeward face and the windward sides of the street canyon's buildings depending on the perpendicular velocity of the wind. This is in a good agreement with the literature [224].

8.5.2 Safety limits

In order to define measures for the firefighting, it is crucial to define the safety limits inside the street canyon. The safety limits for the fire pollutants (smoke, CO and SO_2 etc) are already defined in section 7.5.

As shown on Figure 8-9a, b and c and Figure 8-10a, b and c, in the early beginning of the fire accident the smoke plume rises and most of the smoke passes outside the canyon for all the three different cases. The IDLH area is limited in a small area around the fire location and at the façade of the leeward building. At all the cases, the buoyancy driven inertia forces in the vertical direction are relatively greater than the wind inertia forces. After 70s from the fire incidence, Case 1 (Figure 8-9d and Figure 8-10d) presents a similar IDLH zone with the 30s. In Case 2 (Figure 8-9e) and in Case 3 (Figure 8-9f) the windward building is included in the iso-surface zone and a wider distribution of

the IDLH zone inside the street canyon (Figure 8-10e and f) is found. The iso-surface of the IDLH zone for Case 3 is more tilt than the Case 2.

After 100s of the fire incidence, in Case 1 and in Figure 8-9g and Figure 8-10g, the IDLH zone is still around the fire incidence and we observe low affection inside the rest of the street canyon area. For higher wind velocities the smoke is re-entrained back into the street canyon. As a result, in Case 2 and Case 3 an increase of the IDLH zone inside the street canyon is observed. In Case 2 the IDLH zone covers part of the street canyon area when in contrast in Case 3, the IDLH zone covers almost all the street canyon area. After 200s from fire incidence, in Case 1 the IDLH zone is quite similar to the previous snapshots (Figure 8-9j and Figure 8-10j). In Case 2 (Figure 8-9k and Figure 8-10k) and in Case 3 (Figure 8-9l and Figure 8-10l) similar IDLH zone distributions are observed. Thus, the IDLH zone covers most of the street canyon.

Case 1 , 2.5 m/sec   **Case 2, 5 m/sec**   **Case 3, 7.5 m/sec**

a)   b)   c)

d)   e)   f)

g)   h)   i)

j)   k)   l)
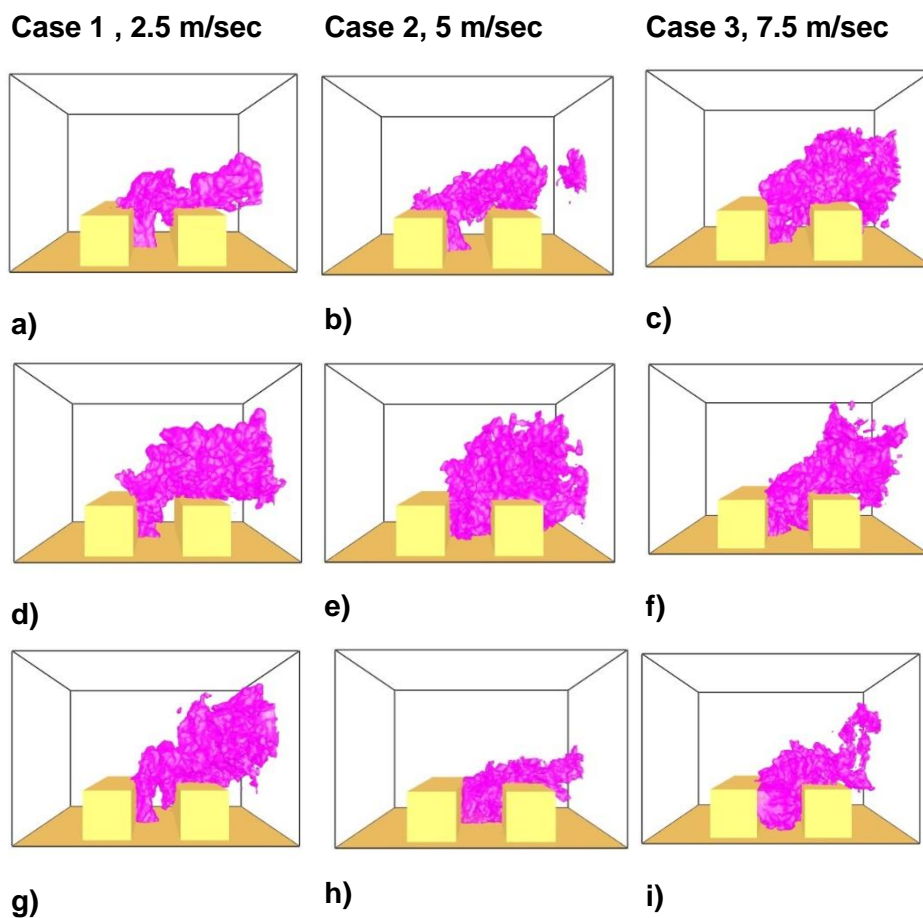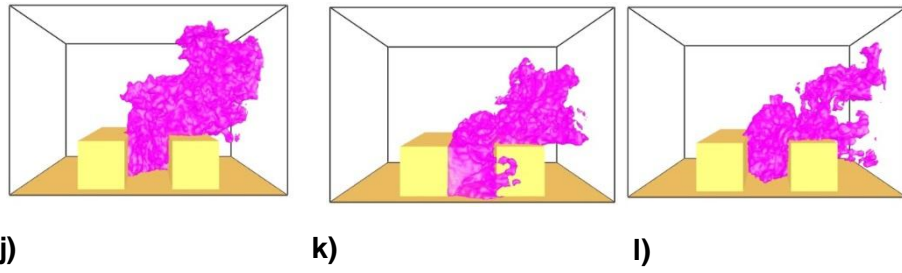
Figure 8-9 The iso-surface of the IDLH zone after 30 sec of the fire incidence a) for Case 1,b) for Case 2, c) for Case 3, after 70 sec of the fire incidence d) for Case 1, e) for Case 2, f) for Case 3, after 100 sec of the fire incidence g) for Case 1, h) for Case 2, i) for Case 3, after 200 sec of the fire incidence j) for Case 1, k) for Case 2, l) for Case 3.

Case 1 , 2.5 m/sec   Case 2, 5 m/sec   Case 3, 7.5 m/sec

a)   b)   c)

d)   e)   f)

g)   h)   i)

| j) | k) | l) |
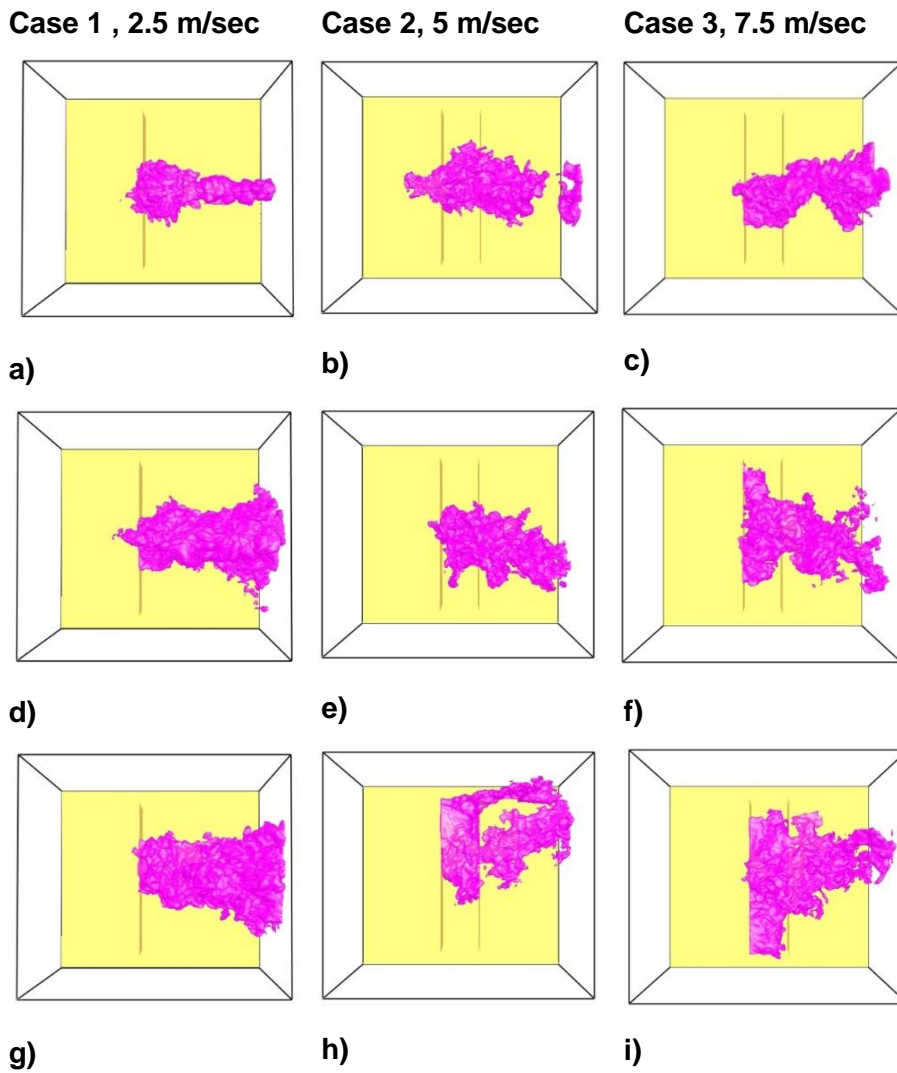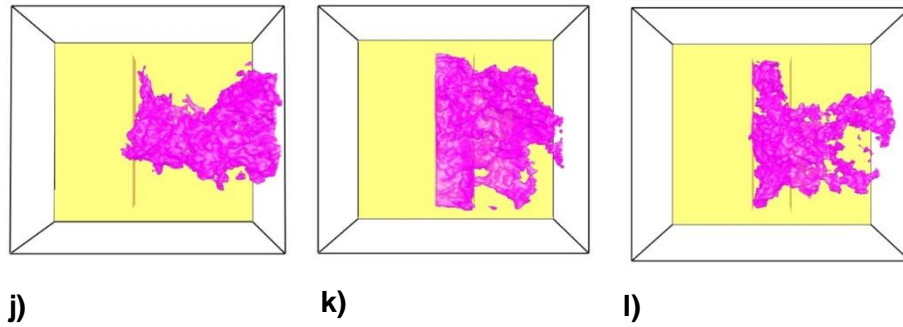
Figure 8-10 The iso-surface of the IDLH zone after 30 sec of the fire incidence a) for Case 1,b) for Case 2, c) for Case 3, after 70 sec of the fire incidence d) for Case 1, e) for Case 2, f) for Case 3, after 100 sec of the fire incidence g) for Case 1, h) for Case 2, i) for Case 3, after 200 sec of the fire incidence j) for Case 1, k) for Case 2, l) for Case 3.

8.5.3 Risk Map generation for a street canyon

The risk zones for a fire accident inside a street canyon for these different wind speeds magnitudes are shown in Figure 8-11. The identification of the sensitive areas around and in the street canyon are shown in a form of a grid (with cells of size 0.15 H) indicating the level of importance in encountering the risk of the toxic smoke after a possible fire accident. The point of accident initiation is defined by the red circle, the risk area is marked with yellow. The sides of the cube covered by a flow recirculation (marked with green) and the wake zone behind the canyon (marked with cyan) demonstrate that special attention is required during intervention. The wind is induced perpendicular to the street canyon. The risk zones for the low (Figure 8-11a), the medium (Figure 8-11b) and the high velocities (Figure 8-11c) are defined in Figure 8-11. For all the cases, the risk zone mainly remains inside the street canyon and part of the smoke is escaping from the canyon. The smoke distribution above the canyon depends on the approaching velocity magnitude. Higher velocities change the tilt of the risk zone towards the roof of the windward building.
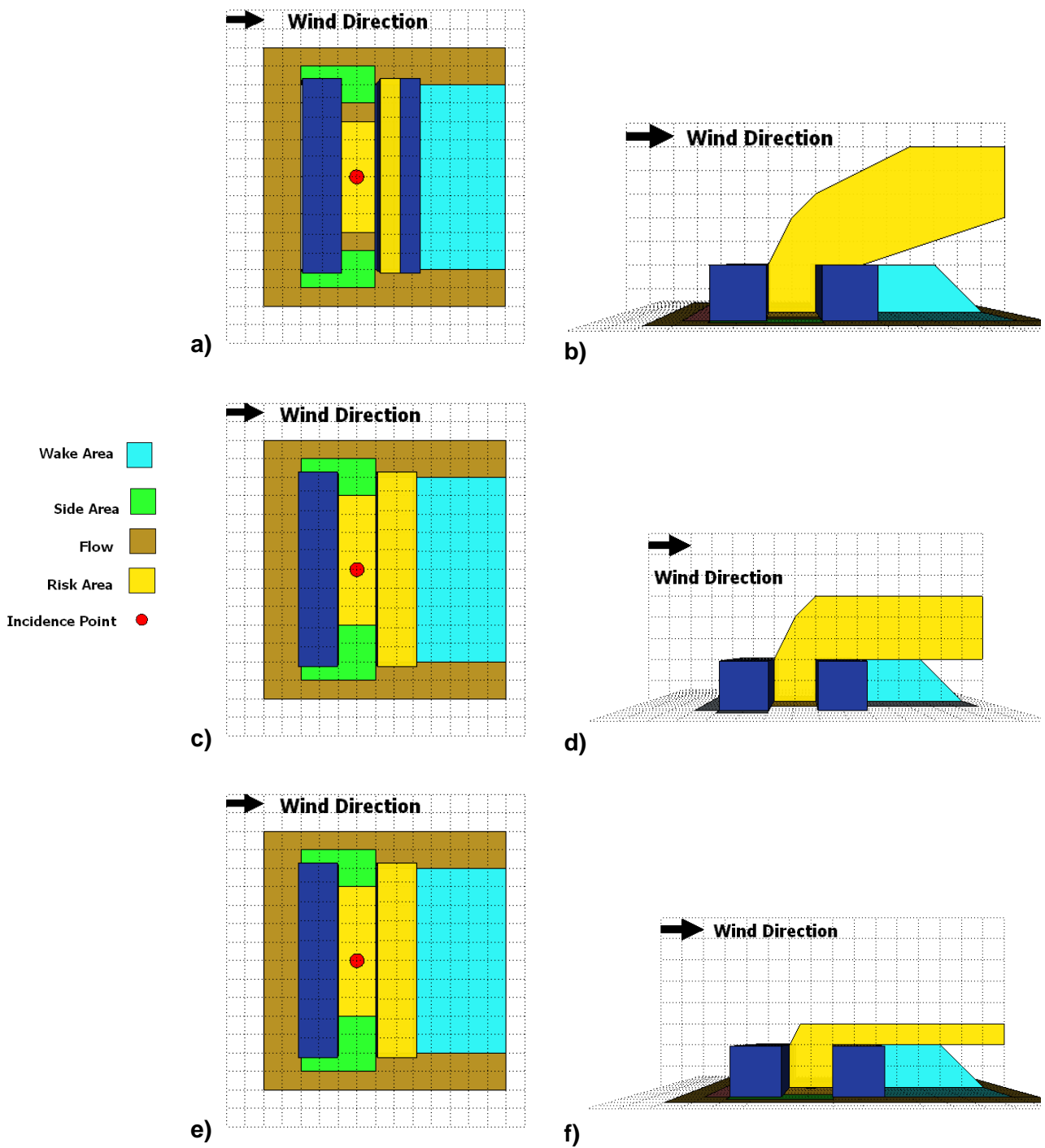
Figure 8-11 Flow areas and Risk zones of a fire accident in a street canyon with a) a low, b)a medium and c) a high velocity profile approach

8.5.4 Conclusion

This study investigates how a perpendicular approaching wind affects the IDLH zone inside a street canyon after a diesel pool fire incident. Based on the IDHL

iso-surfaces, we observe that the danger area inside the street canyon is smaller for small wind velocities and potentially at a lower risk for the public. At low velocities the buoyancy inertia forces release the smoke pollutant outside the street canyon area and the IDHL zone is limited to a small area around the pool fire. At higher velocities the smoke re-circulate and enter back into the street canyon. This is due to the dominant wind inertia forces. High velocities create an IDHL zone that covers most of the street canyon area and are highly risky for the public safety.

The buoyancy forces play an important role for the smoke distribution due to the thermal upward moving. On contrary the wind flow, with the inertial forces acts against the buoyancy forces and trap the fire pollutants inside the street canyon. The velocity profile of the incoming wind is crucial for the smoke distribution. An elevated Richardson number shows that, the buoyancy forces are important and the mixing between the smokes products and the air is minimized. A medium or lower Richardson number shows that the buoyancy forces are not so important and that the smoke plume is trapped inside the street canyon.

Comparing the streamlines of the three cases with the streamlines of a canyon without a fire inside, it is evident that the main canyon vortex is displaced from the centre of the canyon into the upper part of the canyon. As a result the canyon vortex does not play an important role for the smoke mixing but for the trap of the smoke inside the canyon.

CHAPTER 9.   Computational assessment of the hazardous release dispersion from a diesel pool fire in a complex building's area

This chapter focus on the study of a fire accident into a building's array topology which is similar to an urban geometry. A diesel pool fire accident was studied with a Large Eddy Simulation model based on the Fire Dynamics Simulation model. This model was successfully compared against the nine cubes of the SILSOE's field experiments. The model's results were used for the determination of the immediately dangerous to life or health smoke zones of the accident. It was found that the urban geometry defined the hazardous gasses dispersion, thus increasing the toxic mass concentration around the buildings.

9.1 Introduction

An urban environment is an assembly of buildings, parks, commercial and industrial areas, public buildings and infrastructure such as roads, railways, and airports. The human activity inside the city life could cause serious accidents with hazardous release accident. The air flow distribution and the turbulent diffusion phenomena at the complex environment of a city could result in an unpredictable evolution of an urban accident. This complexity could constitute an impediment to the proper intervention and the accident's management. It is therefore important to understand the urban structure and its form, in order to prevent serious toxic release accidents. The main units of an urban environment are the urban building blocks and define the flow distribution inside the city's environment.

The current study presents appropriate computational techniques for the prediction of a toxic release in an urban environment after a fire accident. It also presents a qualitative and a quantitative analysis for different urban geometries in order to predict the immediately dangerous to life or health (IDLH) smoke zones.

9.1.1 Flow field description

A simplified urban domain model of nine cubes in different rectangular staggered arrays is studied as is shown in Figure 9-1 . This cube's arrangement is similar to the SILSOE cube arrays research site [225, 226]. In Figure 9-1 a, the D2 cube is the SILSOE cubical building. The surface pressure of the SILSOE cube is experimentally measured with pressure taps so the present numerical model is successively validated against these measurements as it is discussed in the next Section. Three different cubes arrangements and the smoke fire dispersion from different diesel pool fire locations are considered as it is shown in Figure 9-1 . Each column array is marked with a unique letter. All cubes are of a H=6m height and they are shifted in lines and columns of 6m distance. For Case 1, the pool fire is placed between the D1 and D2 cubes that are in a distance 3H and C1 and E1 cubes that are in distance H. For Case 2, the pool fire is placed between B2 and B3 cubes that are in distance H and A2 and C2 cubes that are in distance 3H. And finally, for Case 3, the pool fire is placed between A and B columns. The wind flow direction in each Case is also shown in Figure 9-1 . The smoke concentration level is studied along A, B, C, and D lines. All the lines are placed at an H distance from the center of the diesel pool fire.

The computational domain is extended at X=20H, Y=20H, and Z=8H in the streamwise, the perpendicular and the height direction. For each case, the diesel pool fire is set at the center of the domain as shown in Figure 1 at X=Y=Z=0.
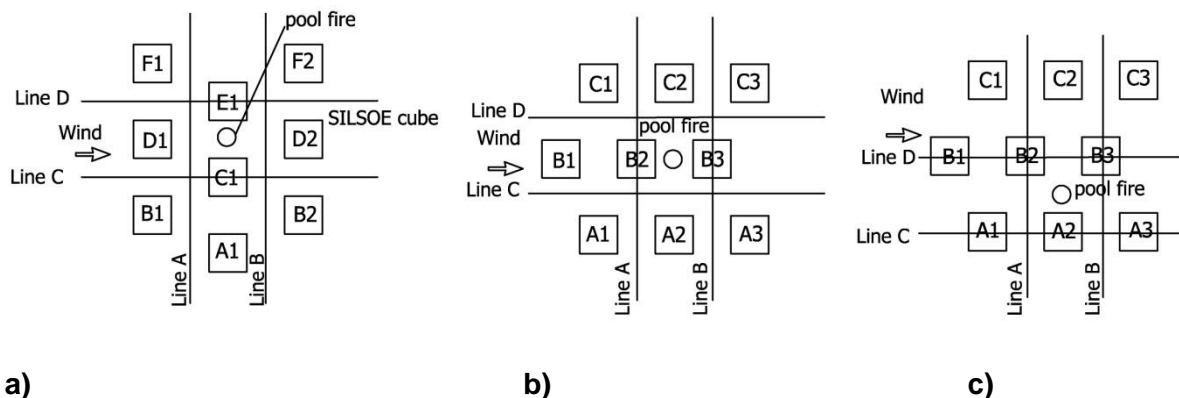
Figure 9-1 Model city buildings arrangement (marked squares), diesel pool fire location (circle) and wind direction (arrow) for a) Case 1 where the Silsoe cube is also indicated, b) Case 2, and c) Case 3.

9.1.2 Numerical details and Validation

An explicit predictor-corrector finite difference scheme is applied, which is second order accurate in space and time. The Poisson equation for modified pressure is solved in every time step by a direct FFT-based solver. The flow variables are updated in time using an explicit second-order Runge-Kutta scheme. The convective terms are upwind-biased differences in the predictor step and downwind biased differences in the corrector step. The thermal and material diffusion terms are pure central differences, with no upwind or downwind bias, thus they are differenced the same way in both the predictor and corrector steps. FDS uses a structured staggered grid with the immersed boundary method (IBM) for the treatment of the flow obstruction [220].

The computational mesh is important for the accuracy of the numerical model. The grid spacing is defined from the equation (8-2) [221]. The grid size is set as D^*=0.273m applied uniformly in the computational domain. The total number of cells in the simulations is kept up to 5,200,000 and the duration of the simulation lasts for 250s.

During the calculation, the time step is adjusted so that the CFL <1 condition to be satisfied. The averaging of fluid flow and transport quantities are recorded between 100s, where the fire dispersion starts, and 250s. The initial transient at

157

100 sec is adequate for the flow field to become stationary. Concentration averaging become at 250sec when smoke plume was fully developed.

Results from the present simulations are compared successively against experimental data [225, 226] for the pressure coefficient, C_p.
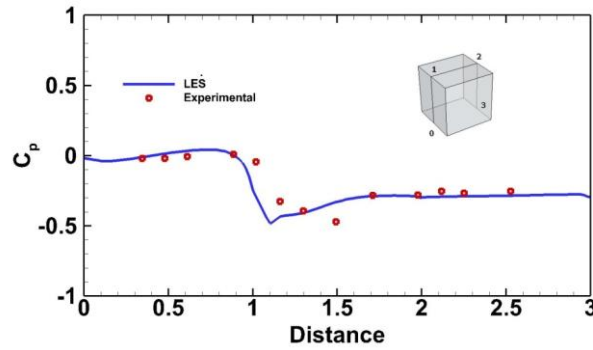
Figure 9-2 Pressure coefficient around the SILSOE Cube situated in the building array of Case 1, with "-" are the present results and with "o" are the measurements from the King, et al. [225] experiments.

9.1.3 Boundary Conditions

Appropriate inlet conditions of the Silsoe research site experiment are applied [194]. The velocity distribution at the inlet is defined as:

$$U(z) = \frac{u_*}{\kappa} \ln\left(\frac{z+z_o}{z_o}\right),$$
(9-1)

$$u_* = \frac{\kappa \, U_{ref}}{\ln\left(\frac{z_{ref}}{z_o}\right)}$$
(9-2)

where κ=0.4 is the von Karman's constant, $z_{ref} = H$ is the reference height, z_o=0.01m is the ground roughness height [202], the undisturbed approach of the flow velocity at the cube's height is Uref = 10.08 m/sec.

The lateral boundary conditions are set as periodic. An open boundary where the fluid is allowed exit from the computational domain is applied at the outflow condition. At the outflow boundary, the standard zero-gradient condition is

applied. The floor of the domain and the cube's wall are modelled with a log-law velocity profile.

9.1.4 Diesel Pool fire

A fire is a reaction of a hydrocarbon fuel with oxygen that produces carbon dioxide and water vapour. Most of the times the air is inefficient and this has as result the production of multiple combustion products. In order to limit the computational time a simplified approach to the chemistry is applied involving six gas species (Fuel, CO_2, CO, H_2O, O_2, N_2) and soot particles. The air, the fuel, and the fire products are referred to as 'lumped species'. Fuel and products species are explicitly computed. The lumped species approach is the accordance with the mass transport equations.

The diesel pool fire incident has a D=3m diameter with a total heat release rate q̇ (HRR) 13.5 MW. and the same characteristics as the fire inside the street canyon which is described in section 8.2.2. The smoke yield is defined as 17.5%.The risk zones are defined by the toxic limits which are described in section 8.5.2.

9.2 Results and discussion

9.2.1 Flow field results

Large-eddy Simulations are performed by the FDS code for a diesel pool fire incident inside the array of cubes. The mean flow in the staggered cubes array is very complicated as it is characterized by different vortices as shown in the streamlines of Figure 9-3. It is detached on the roof top of the buildings and forms vortices simultaneously with the side vortices that are also formed at the buildings. These vortices enter inside the street intersections and influence the flow characteristics inside the cubes' rows and columns. Important helicoid vortices are formed behind the buildings of the first column which are responsible for the fire's products dispersion. This phenomenon is decreasing in the second column of the array, and finally, wake vortices are formed behind the last column of the cubes.
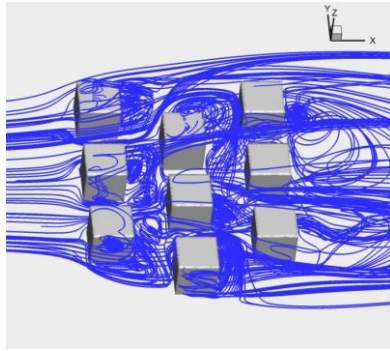
Figure 9-3 Prospective streamline plot of the mean flow in the array of cubes of Case 1.

In Case 1, the cube lines are staggered perpendicular of the wind direction which means that the flow is no longer symmetrical. As shown in Figure 9-4a for the streamlines at the plane Z = 1m, the asymmetry has an important effect to the flow distribution. Two recirculations behind the leeward face of the D1 cube and a small one at the lateral face appear. The streamlines diverge between the C1 and E1 cubes, just at the pool fire accident location. A smaller lateral recirculation appears at the lateral face of the C1 cube. In contrast, Case 2 leads to a more symmetrical flow. As shown in Figure 9-4b, similar mirror recirculations appear at the fire symmetry axis, Y=0, while the streamlines at the fire position reverse towards the Cube B2. Finally, the streamlines of Case 3 are presented in Figure 4c. It is found that the pool fire location isn't affected by the cube's recirculation zone. The buoyancy forces are so strong that an important asymmetry is found and a major horizontal recirculation zone is formed inside the street canyon.

Figure 9-5a, b and c present the time-average streamlines for the fire symmetry plane at Y= 0 m for the Cases 1, 2 and 3, respectively. From this figure, it is shown that for all the cases, the buoyancy-driven forces due to the fire are relatively stronger in the vertical direction than the wind inertia forces. This phenomenon leads the smoke dispersion patterns outside the cube's array.
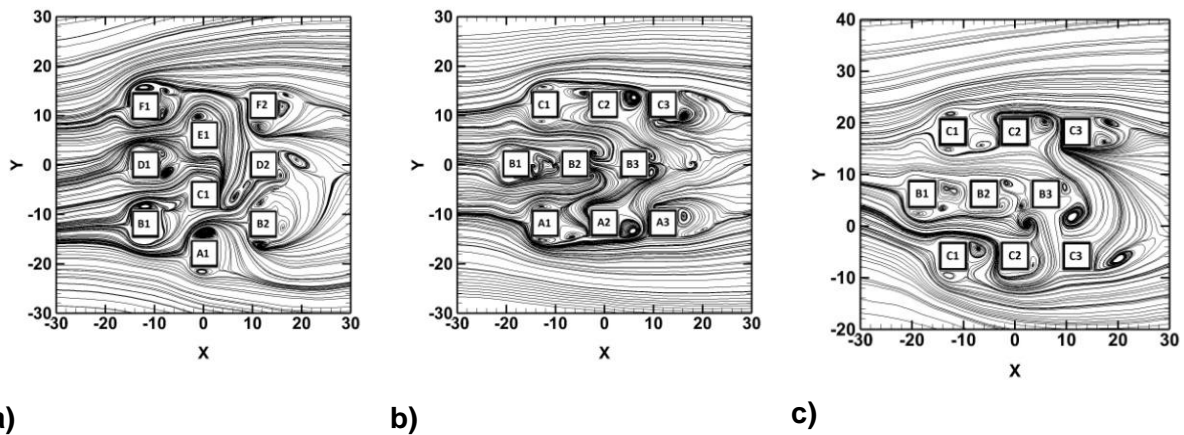
Figure 9-4 Time-averaged streamlines of the horizontal plane Z=1m for a) Case 1, b) Case 2 and Case 3.
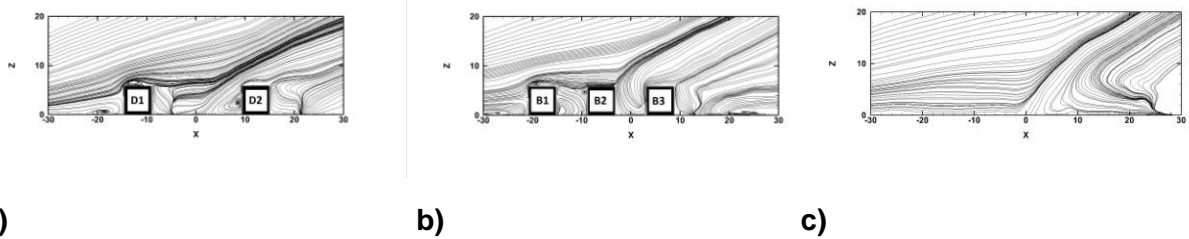
Figure 9-5 Time-averaged streamlines at the symmetry plane Y=0 m for a)Case 1, b) Case 2, and c) Case 3.

Figure 9-6 shows the smoke dispersion snapshots of the diesel pool fire after 200 sec of the incidence for the three studied cases. The general observation is that the smoke plume is driven by the buoyancy and wind, and reaches the top of the cube's arrays. Due to the importance of the buoyancy forces, the smoke is moved outside the arrays and only a small part of it recirculates between the cubes.
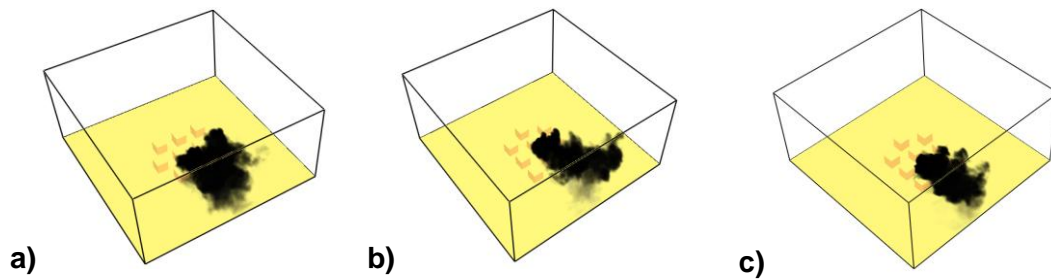
Figure 9-6 Snapshots of the dispersion of smoke after 200 sec of the incidence for a) Case 1, b) Case 2, and c) Case 3.

The identification of vortices and coherent structures could be made with the iso-surfaces of the Q-criterion. In Figure 9-7 the Q=0.1 level is selected to better visualize the turbulent structures for the three different cases. It can be seen that the horseshoe vortex is formed on the leeward face of all the cubes that are in the direction of the induced wind. Hairpin vortices are formed for all array of cubes of Case 1, while for Case 2 and 3, hairpin vortices are formed only for the first line of the array cubes which face the incoming wind. The pool fire source for Case 1 and 2 is located in the wake zone of D1 and B2 cubes, respectively. The flow inside these wake zones forms a strong mixing and turbulence generation region. As shown in Figure 9-7 a fire accident produces important coherent structures that exceed the cubes array height.
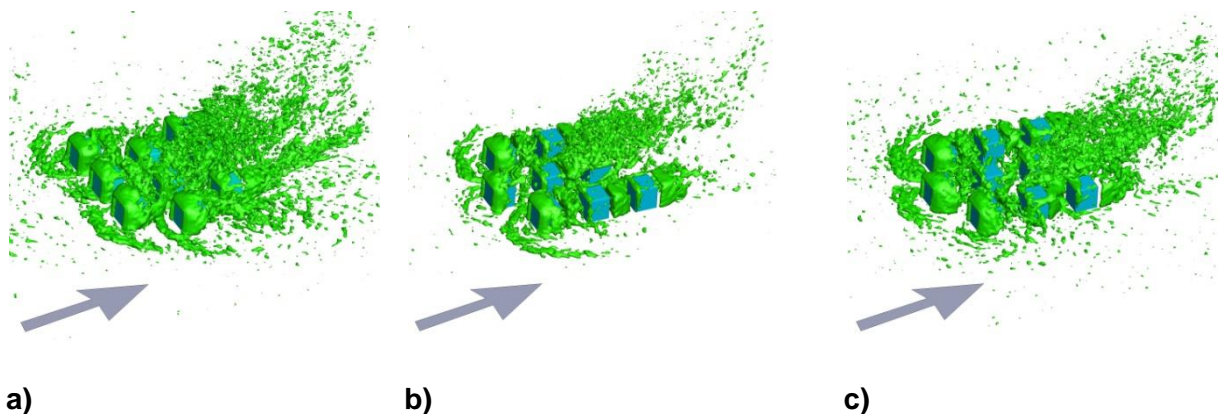
Figure 9-7 Snapshots of the Q criteria for a) Case 1, b) Case 2, and c) Case 3.

9.2.2 Smoke Concentration

Figure 9-8, Figure 9-9 and Figure 9-10 show the average smoke concentration along A, B, C and D lines for Case 1, Case 2 and Case 3, respectively. As shown in Figure 9-8a the smoke concentration leeward the fire position (A line) is negligible.

As shown from the streamlines on Figure 9-8e the smoke is channelled along line B. Additionally, an important recirculation zone is created leeward of the C1 cube which traps the smoke. In this region, the smoke concentration has the highest limits. It is also important to report that the smoke concentration has higher values at the Z=3m level (Figure 9-8b). Along line C (Figure 9-8c) the smoke concentration is more important than this of line D (Figure 9-8d).
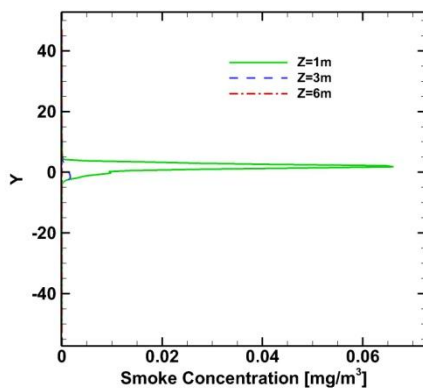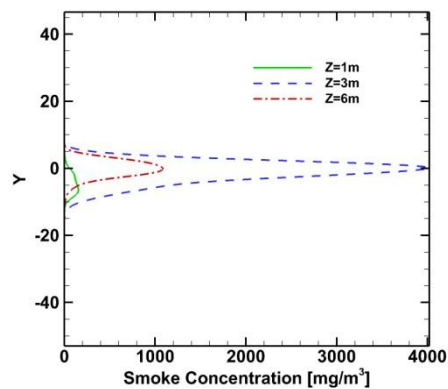
a)   b)
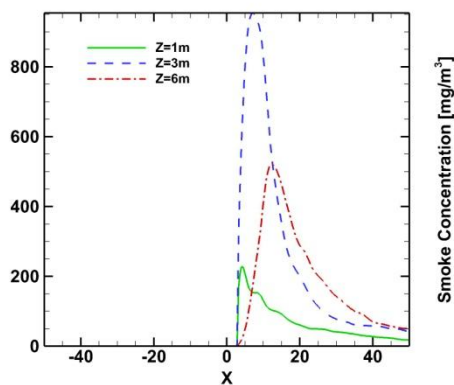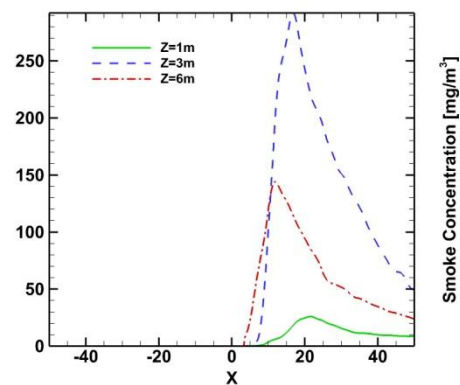
c)   d)
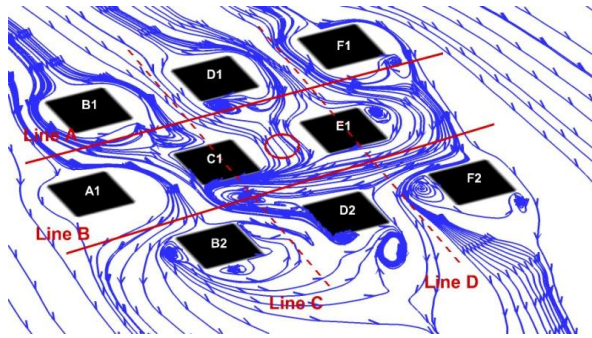
e)

Figure 9-8 Smoke average concentration distribution along a) line A, b) line B, c) line C, d) line D for Case 1 and e) the streamlines that define it.

Figure 9-9a shows that the smoke concentration at the windward line A of the fire position is minimum, but presents slightly higher values than in Case 1. Figure 9-9b shows the maximum values of smoke concentration are presented at the lateral sides of the B3 cube. As shown in Figure 9-9c and Figure 9-9d, the smoke concentration distribution is quite similar for both C and D lines. This is due to the symmetry of the flow and the pool's fire position.

a)   b)

164
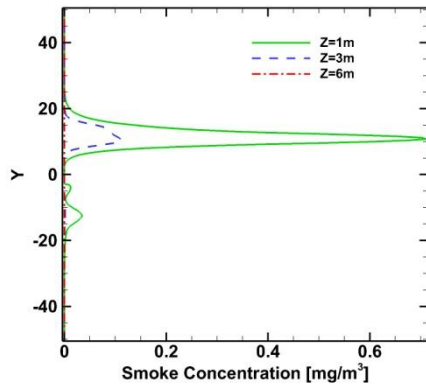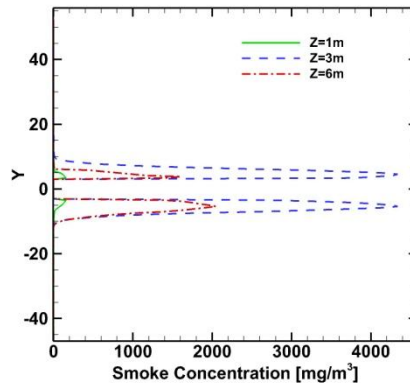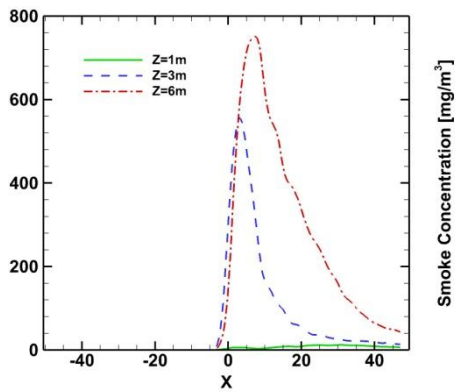
(c)
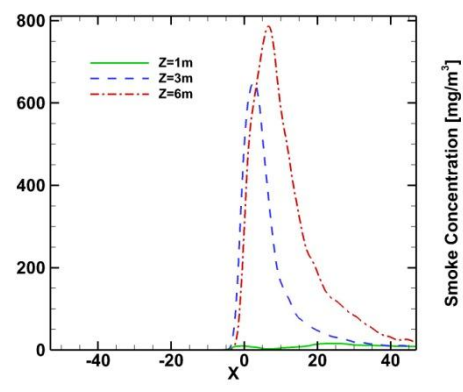
(d)
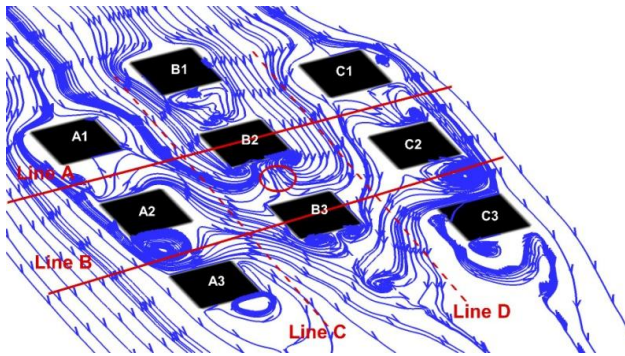
e)

Figure 9-9 Smoke average concentration distribution along a) A line, b) B line, c) C line, d) D line for Case 2 and e) the streamlines that define it.

Finally, in Figure 9-10a the smoke concentration at the leeward line A of the fire position is also minimum. Along line B (Figure 9-10b) the smoke concentration distribution is at its maximum level at 3m height. Along lines C and D the smoke concentration is changing with complex variations due to complex flow phenomena caused by the cubes' blockage. In Figure 9-10c the smoke concentration between A1 and A2 presents the highest values at the Z=3m height. Between A2 and A3 cubes, the highest values of concentration are at the Z=6m height. In Figure 9-10d the smoke concentration between B1 and B2 cubes is maximum at Z=1m height. Between B2 and B3 cubes, the maximum level is at Z=6m height.
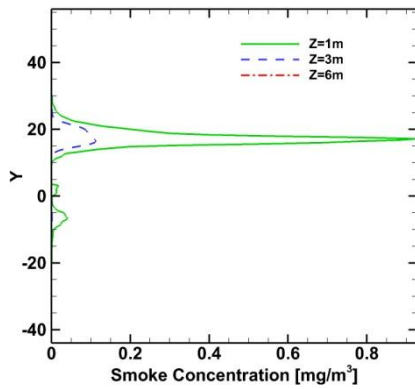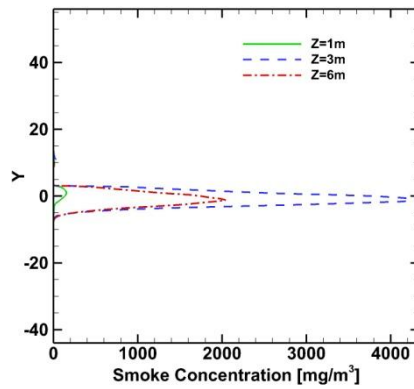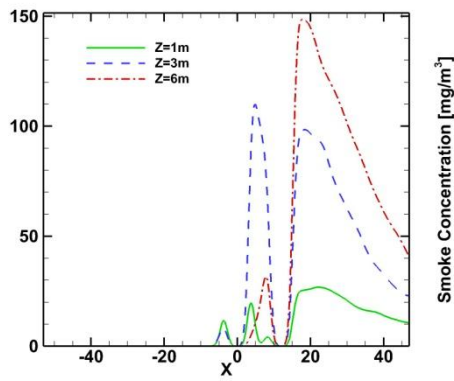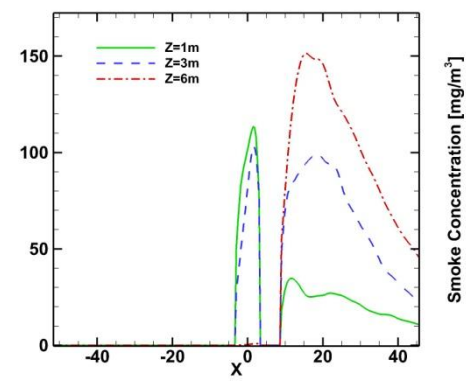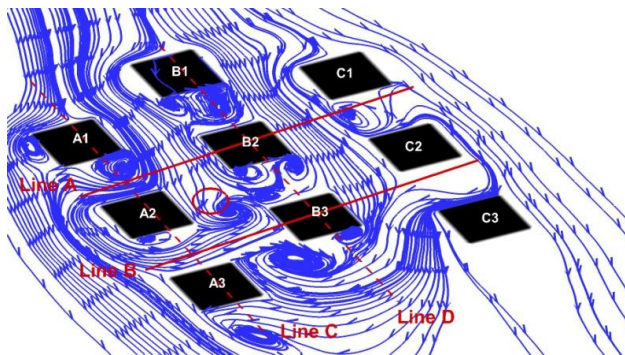
Figure 9-10 Smoke average concentration distribution along a) line A, b) line B, c) line C, d) D line for Case 3 and e) the streamlines that define it.

9.2.3 Safety limits

For fire-fighting measures, it is important to define the safety limits between the urban building blocks. The definition of the toxic limits is presented into 7.5 Toxic zones chapter.

Figure 9-11 and Figure 9-12 present the limits of the LC1 and IDLH zones for the three different cases after 200 seconds at the fire's symmetry plane and at a horizontal plane placed Z=1 m above the ground. The LC1 zone is indicated with the red colour and the IDLH zone with the green color. Outside the IDLH zone, the area is safe. As shown in Figure 9-11 and Figure 9-12 the smoke plume rises and most of the smoke passes outside the level of the arrays cube for all the three different cases.

As it is shown in Figure 9-11a and Figure 9-12a the IDLH smoke zone disperses towards the D2 cube. This means that all the cube's façade openings of this side should be closed and protected in a street fire case. Most of the smoke products exit the street canyon before reaching the D2 cube. A wider distribution of the IDLH zone is presented between the C1 and E1 cubes. The non-symmetrical geometry has as effect the wider distribution of the IDLH zone between the cubes. According to Figure 9-11b and Figure 9-12b, the IDLH smoke zone disperses towards the leeward facade of the B2 cube. This means that all the cube's façade openings at this side should be closed and protected in a street fire case. Finally, Figure 9-11c and Figure 9-12c present the IDLH smoke zone from a fire accident that isn't placed in a cube's recirculation zone. The tilt of the IDLH smoke zone escaping the cube's arrays height is similar for all the cases.
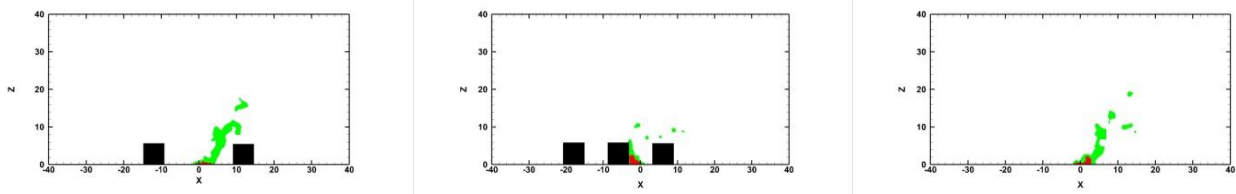
a)   b)   c)

Figure 9-11 The LC1 and IDLH zones at the fire's symmetry for a) Case 1, b) Case 2 and c) Case 3 after 200 sec of the fire incidence.
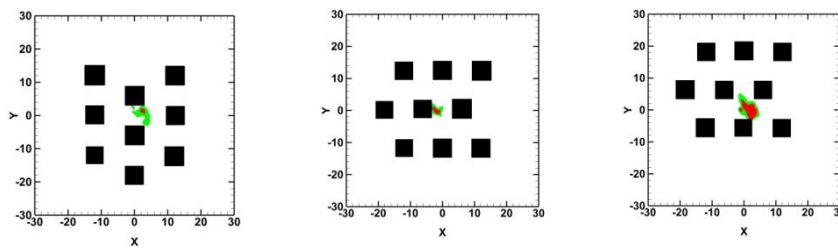
a)   b)   c)

Figure 9-12 The LC1 and IDLH zones for a horizontal plane at Z=1m above the ground for a) Case 1, b) Case 2 and c) Case 3, after 200 sec of the fire incidence.

Table 9-1 defines the zone limits of the LC1 and IDLH zones for all the studied cases and for the Fire's symmetry plane and a Horizontal Plane at Z=1m above the ground. Case 2 presents the most extended area of the LC1 zone (4.2m) at the Horizontal plane Z=1m. Both Case 1 (1.35m) and Case 3 (1.8m) are presenting a similar LC1 zone extension. At the same plane, Case 3 presents the most extended area of the IDLH zone (5.83m) and Case 1 (4.2m) comes after. At the fire's symmetry plane, Case 3 presents the higher limits for both LC1 (2.5m) and IDLH (23.32m) zones. Concerning the LC1 zone, Case 1 presents the smallest radius extension of the 0.6m radius and Case 2 presents a 1.96m radius extension. Finally, Case 1 presents an important IDLH radius extension which is 18.5m and Case 2 presents a 10.4m extension.

Table 9-1 LC1 and IDLH radius for Case 1,2 and 3.

	Case 1	Case 1 (Radius)	Case 2 (Radius)	Case 3 (Radius)
LC1 zone	Horizontal Plane Z=1m	1.35m	4.2m	1.8m
IDLH zone	Horizontal Plane Z=1m	4.2m	2.46m	5.83m
LC1 zone	Fire's symmetry plane	0.6m	1.96m	2.5m
IDLH zone	Fire's symmetry plane	18.5m	10.4 m	23.32m

9.3 Risk map generation for a complex building's area

The risk zones for a fire accident inside a staggered array of cubes at different accidental cases is shown in Figure 9-13. The identification of the sensitive areas around and in the street canyon are shown in a form of a grid (with cells of size 0.5 H) indicating the level of importance in encountering the risk of the toxic smoke after a possible fire accident. The point of accident initiation is defined by the red circle, the risk area is marked with yellow. The sides of the cube covered by a flow recirculation (marked with green), the wake zone behind the canyon (marked with cyan) and with the channeling effect (marked with tile color) demonstrate that special attention is required during intervention. The smoke distribution depends on the geometrical arrangement and the position of the fire. A simplified risk map is generated for the fire accidents between the staggered array of cubes. Case 2 and Case 3 present a symmetrical Risk map with the axis of symmetry at the pool's fire location. The areas of risk, the wake areas and the sides area are easily predicted and defined. As shown in Figure 9-13c, Case 1 presents a complex risk map with important channelling effects.
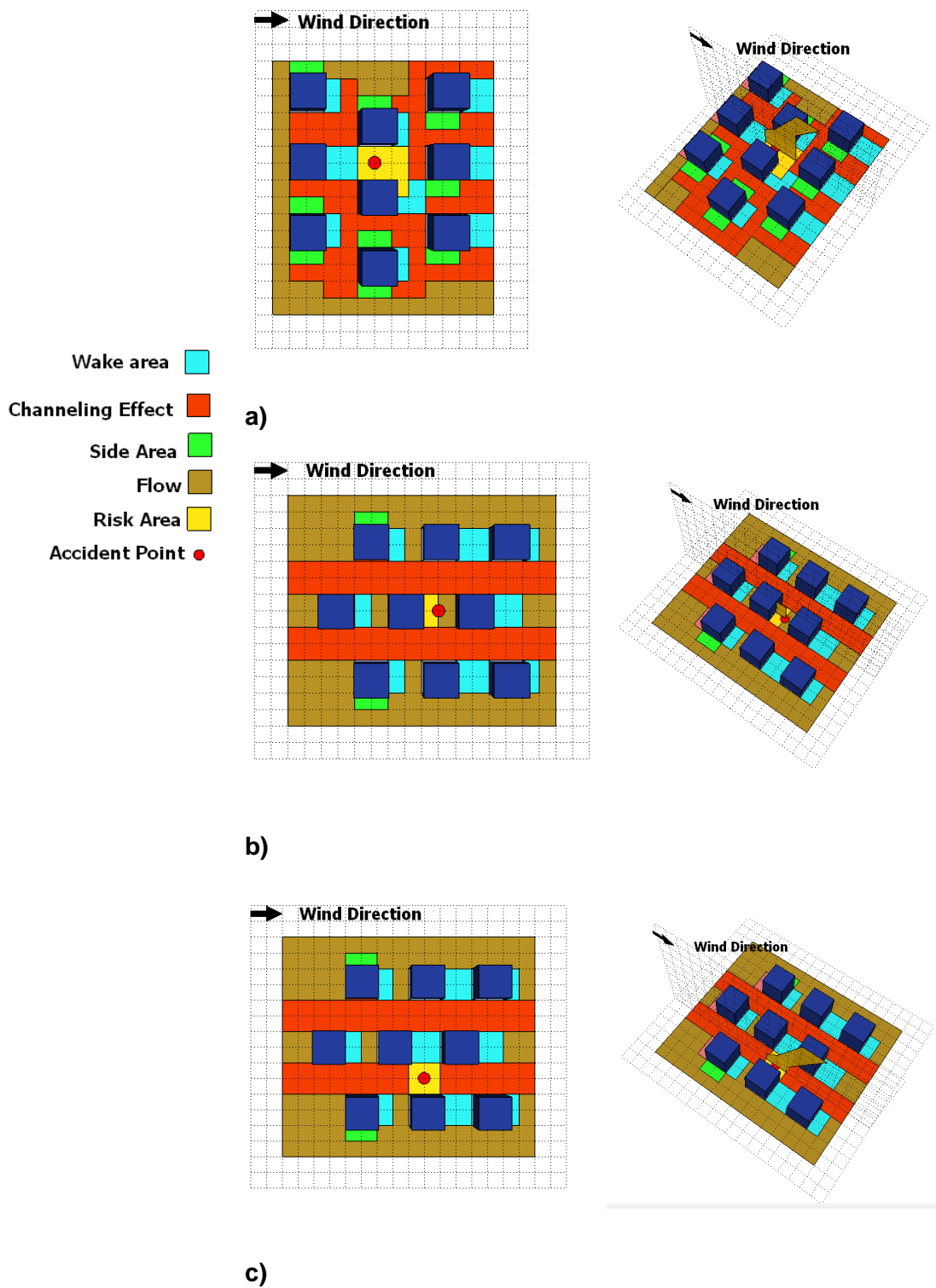
Figure 9-13 Flow areas and Risk zones of different positions fire accident in staggered array arrangement for a) Case 1, b) Case 2 and c) Case 3.

9.4 Conclusion

This study investigates how a diesel pool fire incident affects the wind flow in a staggered array of cubes. The different urban geometry determinates the wind distribution and the smoke dispersion. Several predictions for the smoke dispersion and the fire accident position could be made for an urban area. It also defines the IDLH smoke zones for an incident occurring in a complex urban morphology and proposes the measurements for a quick response estimating the immediate intervention. The limits of the IDLH zones with contour graphs give practical visual information for the danger zones and the definition of the intervention zones.

For a small distance between buildings and a perpendicular wind applied, a fire accident will direct the smoke towards the windward building. In a symmetrical geometry of urban blocks, the smoke after a fire accident will be also symmetrically dispersed. If the fire is between two buildings with a long distance the smoke will be driven towards the leeward building. Complex geometries without any axis of symmetry could lead to unpredictable flows due to the fact that the wind may prefer to follow a specific path that could not be predicted with pre-planned actions. Finally, if the fire is placed in a road and the wind is parallel during the accident, the smoke follows the wind direction but it is disturbed from the building's lateral recirculations.

The LC1 and IDLH zone limits were calculated for all the cases. Street canyon, such as Case 2, with small street width to building's height ratio, presents the highest LC1 limits for the horizontal planes at 1 m height from the ground level. A pool fire that is placed in a well-ventilated position and there is no trap for the smoke pollutant presents an important extension of the IDLH zone along the wind direction. Different wind velocities should be studied in order to define the possibility of the smoke re-entering back into the array's cubes.

CHAPTER 10.   Conclusions

This chapter collects all the work conducted in the current research and highlights the basic conclusions in order to propose a deeper comprehension of the dispersion of smoke released in an urban environment after an accident of fire.

The main objective of this study is to understand and define the flow behavior and the dispersion of the smoke releases in the urban environment after a fire accident. Wind tunnel and Computational Fluid Dynamics methods are used. The thesis has the 'Paper Style' thesis format and it is constituted by 10 chapters. The Chapter "Conclusions" is divided in two parts: a) the conclusions for each chapter and the overall conclusions and b) the suggested work for further study and the value of this work for the mitigation and the management of urban accidents.

10.1 Chapter Conclusions

After the conducted numerical and experimental research, the following conclusions can be drawn.

Chapter 5 concluded that the study of the flow field around urban geometries is necessary in order to define the smoke dispersion. The mean velocities and the Reynolds stresses determine the flow field. The experimental and numerical studies conducted helped to define the computational settings of the boundary conditions and also the areas with important turbulence and recirculation. It is important also to define the Reynolds stresses before the examination of any accidental scenario in order to define the momentum fluxes. The wind tunnel experiments defined the flow inlet characteristics, the building's roof reattachment in relation to the height of the boundary layer and finally the turbulence flow around the buildings. The pressure distribution around the tested wind tunnel models was examined and compared with other researchers' experimental data. One of the limitations of the wind tunnel experiments compared to real field experiments is the lack of the low-frequency turbulence fluctuations, resulting in lower longitudinal and transverse turbulence intensities.

This means that the large scales of turbulence are not captured [169]. This limitation also influences the pressure coefficient distribution (Cp) around the scaled buildings.

LES experiments were also conducted and helped defining the patterns of the flow around the different scales of urban geometries and the eddies, the recirculation zones and the increase of the wind around these geometries. In essence, chapter 5 offers an introduction regarding smoke dispersion around these typical urban geometries after a smoke release accident.

Chapter 6 concluded that the RANS k-epsilon models underestimate the flow characteristics around the cubical geometries, which affects the pollutant dispersion around these geometries.

In the current research a 3D geometry with three different turbulence models is compared: the standard k-epsilon model with standard wall functions (St-ke-WF), the Standard k-epsilon with the Kato-Launder model (St-ke-KL) and the Standard k-epsilon with low Reynolds model (St-ke-low-Re). The output of this research concluded that different approaches of the wall functions present small differences to the flow characteristics such as the separation length, the reattachment point at the building's roof and the pollutant concentration distribution

At the cube's roof the St-ke-KL model predicts a long separation zone and does not present a reattachment point on the top of the cube's roof. The St-ke-WF and the St-ke-low-Re models predict a smaller recirculation zone and a reattachment point at a position which is situated before the cube's centre. This estimation led to high concentrations windward of the release vent which is not confirmed from the experimental data. The long recirculation length behind the building is due to the underestimation of the turbulence kinetic energy (G_k term). The concentration level decreases as the flow passes through the cube's edges. At the edge point of the cube an important underestimation of the dimensional concentration appears for all the k-epsilon models compared to Meroney's experimental data. The standard k-epsilon Kato Launder model presents results that are in a better agreement with the Meroney's experimental

data and shows a more diffusive main core than the other k-epsilon models. The St-ke-WF and St-ke-low-Re models have similar dimensional concentration lengths to the Gaussian model of Huber and Snyder. The Gaussian models fail to predict the downwind shift of the dimensional concentration in the building's cavity zone. On the other hand, RANS models are in better agreement with the experimental data. Comparing different lateral isopleths planes behind the cube, St-ke-WF is in a better agreement with the experimental data compare to the other k-epsilon models near the wake cube. In contrast, moving away behind the cube, the St-ke-low-Re is in a better agreement with the experimental data. The St-ke-WF and St-ke-low-Re failed to accurately predict the central roof hazardous material release. St-ke-KL has a better approach and could be an option for this kind of problems. On the contrary, St-ke-KL overpredicts the hazardous zone compared to the other two models that are in a better agreement with the experimental data. In order to define the hazardous release dispersion for safety approaches, it is important to define the advantages and disadvantages of each model. Even though the RANS models is a realistic option for the hazardous risk map due to computational time economy, differences on the flow dispersion appear.

Chapter 7 concluded that different kind of accidental fires behind a cube presents little changes of the wake zone length.

Two different pool fire cases, a crude oil and a diesel pool fire, located at the cavity of the cube, are examined with an LES model. The diesel pool fire presents dispersion of the smoke concentration with important differences compared to a crude oil pool fire. In a diesel pool fire, the local concentrations are higher than in the crude oil fires. The size of the wake zone has little changes for both pool fire events. In the crude oil pool fire the recirculation zone is slightly longer than in the diesel's pool fire length. The recirculation zone traps a large portion of the smoke plume and both accidental scenarios present similar limits to the maximum extension of the toxic zones. The dilution inside the wake area is not the same. The diesel pool fire has larger smoke production

and covers all of the cavity zone area. As a consequence, the IDLH zone covers also the cavity zone and a small area of LC1 zone appears.

The mechanism of the smoke's mass transportation inside the cavity zone is caused by the convective mass flux and the turbulence mass flux. The convective mass flux at the symmetry plane is similar for both accidental cases. As it is expected, the diesel pool fire accident presents higher concentration levels inside the wake zone compared to the crude oil fire. This is due to the fact that the diesel pool fire releases a higher quantity of smoke than the crude oil fire. The quantity of the smoke is trapped inside the limits of the cavity zone for the convective flow of the x and z velocity components.

Chapter 8 concluded that the approaching wind affects the toxic zones for a street canyon accident after a diesel pool fire accident. It is observed that the danger area inside the street canyon is smaller for small wind velocities and potentially at a lower risk for the public. At low velocities the buoyancy inertia forces release the smoke outside the street canyon area and the toxic zone is limited to a small area around the pool fire. At higher velocities the smoke re-circulate and enters back into the street canyon. This is due to the dominant wind inertia forces. High velocities create a toxic zone that covers most of the street canyon area and are highly risky for the public safety. The main canyon vortex is displaced from the centre of the canyon into the upper part of the canyon. As a result the canyon vortex does not play an important role for the smoke mixing but for the trap of the smoke inside the canyon.

Chapter 9 investigates how a diesel pool fire accident affects the wind flow in a staggered array of cubes. The different urban geometry determinates the wind distribution and the smoke dispersion. This study also defines the toxic smoke zones for an accident occurring in a complex urban morphology and proposes measurements for a quick response estimating an immediate intervention.

If the fire is located to a complex geometry without any axis of symmetry, it could lead to unpredictable flows and smoke dispersion, due to the fact that the wind may prefer to follow a specific path that could not be predicted with pre-planned calculations. In a symmetrical geometry of urban blocks, the smoke

produced after a fire accident will also be symmetrically dispersed. If the buildings are situated in a long distance, the smoke will be driven towards the leeward building. On the contrary, if these is a small distance between them the smoke will be directed towards the windward building (after a fire accident).

Finally, if the fire is placed in a road and the wind is parallel during the accident, the smoke follows the wind direction but it is disturbed from the building's lateral recirculation's. In the current research, the toxic zone limits were also defined. Street canyon, with a symmetrical geometry and small street width to building's height ratio, presents the highest toxic limits at the lower ground level. A pool fire that is placed in a well-ventilated position and there is no trap for the smoke pollutant presents an important extension of the toxic zone along the wind direction.

10.2 Overall Conclusion

Due to the fact that all the chapters are independent, they all contribute to the overall goal of the thesis which is the study of the smoke dispersion after a fire accident in different scales of urban geometries. The study is based on numerical and wind tunnel experiments. The chapters are testing different numerical models which are validated with wind tunnel experiments and experimental data from other researches. Structured, unstructured and immersed boundary method for the treatment of the flow obstruction are tested with the Fluent and FDS code for RANS and LES models.

It is found that general guidelines for the smoke dispersion after a fire accident could be defined and toxic zones can be generated. The better understanding of the smoke dispersion is important for the generation of simplified risk maps which are an efficient tool for the fire-fighting events.

10.3 Future work

Different wind velocities should be studied in order to define all possible scenarios of the smoke dispersion in the basic urban units. Figure 3-1, Figure 3-2 and Figure 3-3 show some of the typical accidental scenarios for a fire accident in an isolated building, in a street canyon and in a staggered arrays of

cubes for different wind angled oblique and different accident positions. Some of these cases were performed in order to generate a risk map for a fire-fighting actions. All of the cases studies described in Figures 3-1, 3-2 and 3-3 should be studied in order to define the hazardous zones and compose risk maps around these basic units of urban geometry.

Another important work that should be done is to examine complex models of real urban cases, validate them with wind tunnel experiments, define the hazardous zones and compose risk maps. The results from different urban case studies should be synthesized and give as deliverable a methodology for the creation of a general risk map that will be based on the basic units of urban geometries studies.

REFERENCES

1. Schnepp, R., I.A.o.F. Chiefs, and N.F.P. Association, *Hazardous Materials Awareness and Operations*. 2009: Jones & Bartlett Learning.
2. Covello, V.T. and W. Merkhoher, *Risk Assessment Methods: Approaches for Assessing Health and Environmental Risks*. 1993: Springer.
3. Bank, T.W., *Urban Risk Assessments: An Approach for Understanding Disaster and Climate Risk in Cities*. 2012: World Bank Publications.
4. ERM, *Emergency Risk Management: Applications Guide*. 2000: Australia. Emergency Management Australia.
5. Holmes, N.S. and L. Morawska, *A review of dispersion modelling and its application to the dispersion of particles: An overview of different dispersion models available.* Atmospheric Environment, 2006. **40**(30): p. 5902-5928.
6. Argyropoulos, C.D., G.M. Sideris, M.N. Christolis, Z. Nivolianitou, and N.C. Markatos, *Modelling pollutants dispersion and plume rise from large hydrocarbon tank fires in neutrally stratified atmosphere.* Atmospheric Environment, 2010. **44**(6): p. 803-813.
7. Gayev, Y.A., J.C.R. Hunt, and N.A.T.O.P.D. Division, *Flow and Transport Processes with Complex Obstructions: Applications to Cities, Vegetative Canopies and Industry*. 2007: Springer.
8. Markatos, N.C., *Dynamic computer modeling of environmental systems for decision making, risk assessment and design.* Asia-Pacific Journal of Chemical Engineering, 2012. **7**(2): p. 182-205.
9. Argyropoulos, C.D., M.N. Christolis, Z. Nivolianitou, and N.C. Markatos, *A hazards assessment methodology for large liquid hydrocarbon fuel tanks.* Journal of Loss Prevention in the Process Industries, 2012. **25**(2): p. 329-335.
10. Communities, G.B.D.f., L. Government, C. Fire, and R. Adviser, *Fire and Rescue Service operational guidance - incidents in tunnels and underground structures*. 2012: Stationery Office.
11. *COST ES1006 - Background and Justification Document, COST Action ES1006,May 2012.*
12. Office, G.B.H., *The Release of Chemical, Biological, Radiological Or Nuclear (CBRN) Substances Or Material: Guidance for Local Authorities*. 2003: Home Office.
13. Dickson, E.B., Judy L. Hoornweg, Daniel Asmita, Tiwari, *Urban Risk Assessments*. Urban Risk Assessments. 2012.
14. Richards, P.J. and R.P. Hoxey, *Flow reattachment on the roof of a 6m cube.* Journal of Wind Engineering and Industrial Aerodynamics, 2006. **94**(2): p. 77-99.
15. Richards, P.J. and R.P. Hoxey, *Pressures on a cubic building—Part 1: Full-scale results.* Journal of Wind Engineering and Industrial Aerodynamics, 2012. **102**: p. 72-86.

16. Tominaga, Y. and T. Stathopoulos, *CFD simulations of near-field pollutant dispersion with different plume buoyancies.* Building and Environment, 2018. **131**: p. 128-139.

17. Richards, P.J. and R.P. Hoxey, *Wind loads on the roof of a 6m cube.* Journal of Wind Engineering and Industrial Aerodynamics, 2008. **96**(6): p. 984-993.

18. Castro, I.P. and A.G. Robins, *The flow around a surface-mounted cube in uniform and turbulent streams.* Journal of Fluid Mechanics, 1977. **79**(2): p. 307-335.

19. Lim, H.C., I.P. Castro, and R.P. Hoxey, *Bluff bodies in deep turbulent boundary layers: Reynolds-number issues.* Journal of Fluid Mechanics, 2007. **571**: p. 97-118.

20. Martinuzzi, R. and C. Tropea, *The Flow Around Surface-Mounted, Prismatic Obstacles Placed in a Fully Developed Channel Flow (Data Bank Contribution).* Journal of Fluids Engineering, 1993. **115**(1): p. 85-92.

21. Larousse, A., R. Martinuzzi, and C. Tropea, *Flow Around Surface-Mounted, Three-Dimensional Obstacles*, in *Turbulent Shear Flows 8: Selected Papers from the Eighth International Symposium on Turbulent Shear Flows, Munich, Germany, September 9 – 11, 1991*, F. Durst, et al., Editors. 1993, Springer Berlin Heidelberg: Berlin, Heidelberg. p. 127-139.

22. Hussein, H.J. and R.J. Martinuzzi, *Energy balance for turbulent flow around a surface mounted cube placed in a channel.* Physics of Fluids, 1996. **8**(3): p. 764-780.

23. Shirzadi, M., P.A. Mirzaei, and M. Naghashzadegan, *Improvement of k-epsilon turbulence model for CFD simulation of atmospheric boundary layer around a high-rise building using stochastic optimization and Monte Carlo Sampling technique.* Journal of Wind Engineering and Industrial Aerodynamics, 2017. **171**: p. 366-379.

24. Luo, Y., H. Liu, H. Xue, and K. Lin, *Large-eddy simulation evaluation of wind loads on a high-rise building based on the multiscale synthetic eddy method.* Advances in Structural Engineering. **0**(0): p. 1369433218794258.

25. Elshaer, A., H. Aboshosha, G. Bitsuamlak, A. El Damatty, and A. Dagnew, *LES evaluation of wind-induced responses for an isolated and a surrounded tall building.* Engineering Structures, 2016. **115**: p. 179-195.

26. van Hooff, T., B. Blocken, and Y. Tominaga, *On the accuracy of CFD simulations of cross-ventilation flows for a generic isolated building: Comparison of RANS, LES and experiments.* Building and Environment, 2017. **114**: p. 148-165.

27. Rodi, W., *Comparison of LES and RANS calculations of the flow around bluff bodies.* Journal of Wind Engineering and Industrial Aerodynamics, 1997. **69**: p. 55-75.

28. Richards, P. and S. Norris, *LES modelling of unsteady flow around the Silsoe cube.* Journal of Wind Engineering and Industrial Aerodynamics, 2015. **144**(Supplement C): p. 70-78.

29. Lim, H.C., T.G. Thomas, and I.P. Castro, *Flow around a cube in a turbulent boundary layer: LES and experiment.* Journal of Wind Engineering and Industrial Aerodynamics, 2009. **97**(2): p. 96-109.

30. Breuer, M., D. Lakehal, and W. Rodi, *Flow around a Surface Mounted Cubical Obstacle: Comparison of Les and Rans-Results*, in *Computation of Three-Dimensional Complex Flows: Proceedings of the IMACS-COST Conference on Computational Fluid Dynamics Lausanne, September 13–15, 1995*, M. Deville, S. Gavrilakis, and I.L. Ryhming, Editors. 1996, Vieweg+Teubner Verlag: Wiesbaden. p. 22-30.

31. Drikakis, D. and W. Rider, *High-Resolution Methods for Incompressible and Low-Speed Flows.* 2010: Springer Berlin Heidelberg.

32. Drikakis, D., *Advances in turbulent flow computations using high-resolution methods.* Progress in Aerospace Sciences, 2003. **39**(6): p. 405-424.

33. Drikakis, D., M. Hahn, A. Mosedale, and B. Thornber, *Large eddy simulation using high-resolution and high-order methods.* Philosophical Transactions of the Royal Society A: Mathematical, Physical and Engineering Sciences, 2009. **367**(1899): p. 2985-2997.

34. Barakos, G. and D. Drikakis, *Investigation of Nonlinear Eddy-Viscosity Turbulence Models in Shock/Boundary-Layer Interaction.* AIAA Journal, 2000. **38**(3): p. 461-469.

35. Leschziner, M.A. and D. Drikakis, *Turbulence modelling and turbulent-flow computation in aeronautics.* The Aeronautical Journal (1968), 2016. **106**(1061): p. 349-384.

36. Lakehal, D. and W. Rodi, *Calculation of the flow past a surface-mounted cube with two-layer turbulence models.* Journal of Wind Engineering and Industrial Aerodynamics, 1997. **67–68**: p. 65-78.

37. Zhang, Y.Q., A.H. Huber, S.P.S. Arya, and W.H. Snyder, *Numerical simulation to determine the effects of incident wind shear and turbulence level on the flow around a building.* Journal of Wind Engineering and Industrial Aerodynamics, 1993. **46**: p. 129-134.

38. Mochida, A., Y. Tominaga, S. Murakami, R. Yoshie, T. Ishihara, and R. Ooka, *Comparison of various k-ε models and DSM to flow around a high rise building -report of AIJ cooperative project for CFD prediction of wind environment.* Wind & Structures, 2002. **5**(2-4): p. 227-244.

39. Yoshie, R., A. Mochida, Y. Tominaga, H. Kataoka, K. Harimoto, T. Nozu, and T. Shirasawa, *Cooperative project for CFD prediction of pedestrian wind environment in the Architectural Institute of Japan.* Journal of Wind Engineering and Industrial Aerodynamics, 2007. **95**(9–11): p. 1551-1578.

40. Li, W.-W. and R.N. Meroney, *Gas dispersion near a cubical model building. Part I. Mean concentration measurements.* Journal of Wind Engineering and Industrial Aerodynamics, 1983. **12**(1): p. 15-33.

41. Thompson, R.S. and D.J. Lombardi, *Dispersion of Roof-top Emissions from Isolated Buildings: A Wind Tunnel Study.* Environmental Sciences Research Laboratory, 1977.

42. Robins, A.G. and I.P. Castro, *A wind tunnel investigation of plume dispersion in the vicinity of a surface mounted Cube—I. The flow field.* Atmospheric Environment (1967), 1977. **11**(4): p. 291-297.

43. Thompson, R.S., *Building amplification factors for sources near buildings: A wind-tunnel study.* Atmospheric Environment. Part A. General Topics, 1993. **27**(15): p. 2313-2325.

44. Higson, H.L., R.F. Griffiths, C.D. Jones, and D.J. Hall, *Flow and dispersion around an isolated building.* Atmospheric Environment, 1996. **30**(16): p. 2859-2870.

45. Mavroidis, I., R.F. Griffiths, and D.J. Hall, *Field and wind tunnel investigations of plume dispersion around single surface obstacles.* Atmospheric Environment, 2003. **37**(21): p. 2903-2918.

46. Delaunay, D., D. Lakehal, C. Barré, and C. Sacré, *Numerical and wind tunnel simulation of gas dispersion around a rectangular building.* Journal of Wind Engineering and Industrial Aerodynamics, 1997. **67–68**(0): p. 721-732.

47. Rossi, R., D.A. Philips, and G. Iaccarino, *A numerical study of scalar dispersion downstream of a wall-mounted cube using direct simulations and algebraic flux models.* International Journal of Heat and Fluid Flow, 2010. **31**(5): p. 805-819.

48. Tominaga, Y. and T. Stathopoulos, *Numerical simulation of dispersion around an isolated cubic building: Comparison of various types of k-ε models.* Atmospheric Environment, 2009. **43**(20): p. 3200-3210.

49. Tominaga, Y. and T. Stathopoulos, *Turbulent Schmidt numbers for CFD analysis with various types of flowfield.* Atmospheric Environment, 2007. **41**(37): p. 8091-8099.

50. Meroney, R.N., B.M. Leitl, S. Rafailidis, and M. Schatzmann, *Wind-tunnel and numerical modeling of flow and dispersion about several building shapes.* Journal of Wind Engineering and Industrial Aerodynamics, 1999. **81**(1–3): p. 333-345.

51. Zhang, Y.Q., S.P. Arya, and W.H. Snyder, *A comparison of numerical and physical modeling of stable atmospheric flow and dispersion around a cubical building.* Atmospheric Environment, 1996. **30**(8): p. 1327-1345.

52. Ogawa, Y. and S. Oikawa, *A field investigation of the flow and diffusion around a model cube.* Atmospheric Environment (1967), 1982. **16**(2): p. 207-222.

53. Jones, C.D. and R.F. Griffiths, *Full-scale experiments on dispersion around an isolated building using an ionized air tracer technique with very short averaging time.* Atmospheric Environment (1967), 1984. **18**(5): p. 903-916.

54. Mavroidis, I., R.F. Griffiths, C.D. Jones, and C.A. Biltoft, *Experimental investigation of the residence of contaminants in the wake of an obstacle under different stability conditions.* Atmospheric Environment, 1999. **33**(6): p. 939-949.

55. Olvera, H.A., A.R. Choudhuri, and W.-W. Li, *Effects of plume buoyancy and momentum on the near-wake flow structure and dispersion behind an idealized building.* Journal of Wind Engineering and Industrial Aerodynamics, 2008. **96**(2): p. 209-228.

56. Olvera, H.A. and A.R. Choudhuri, *Numerical simulation of hydrogen dispersion in the vicinity of a cubical building in stable stratified*

atmospheres. International Journal of Hydrogen Energy, 2006. **31**(15): p. 2356-2369.

57. Vardoulakis, S., B.E.A. Fisher, K. Pericleous, and N. Gonzalez-Flesca, *Modelling air quality in street canyons: a review.* Atmospheric Environment, 2003. **37**(2): p. 155-182.

58. Oke, T.R., *Street design and urban canopy layer climate.* Energy and Buildings, 1988. **11**(1–3): p. 103-113.

59. Kastner-Klein, P. and E.J. Plate, *Wind-tunnel study of concentration fields in street canyons.* Atmospheric Environment, 1999. **33**(24): p. 3973-3979.

60. Salizzoni, P., M. Marro, L. Soulhac, N. Grosjean, and R.J. Perkins, *Turbulent Transfer Between Street Canyons and the Overlying Atmospheric Boundary Layer.* Boundary-Layer Meteorology, 2011. **141**(3): p. 393-414.

61. Baik, J.-J., R.-S. Park, H.-Y. Chun, and J.-J. Kim, *A Laboratory Model of Urban Street-Canyon Flows.* Journal of Applied Meteorology, 2000. **39**(9): p. 1592-1600.

62. Baik, J.-J. and J.-J. Kim, *On the escape of pollutants from urban street canyons.* Atmospheric Environment, 2002. **36**(3): p. 527-536.

63. DePaul, F.T. and C.M. Sheih, *Measurements of wind velocities in a street canyon.* Atmospheric Environment (1967), 1986. **20**(3): p. 455-459.

64. Eliasson, I., B. Offerle, C.S.B. Grimmond, and S. Lindqvist, *Wind fields and turbulence statistics in an urban street canyon.* Atmospheric Environment, 2006. **40**(1): p. 1-16.

65. Inagaki, A. and M. Kanda, *Turbulent flow similarity over an array of cubes in near-neutrally stratified atmospheric flow.* Journal of Fluid Mechanics, 2008. **615**: p. 101-120.

66. Johnson, W.B., W.F. Dabberdt, F.L. Ludwig, and R.J. Allen, *Field study for initial evaluation of an urban diffusion model for carbon monoxide. Comprehensive report.* 1971.

67. Dabberdt, W.F., F.L. Ludwig, and W.B. Johnson, *Validation and applications of an urban diffusion model for vehicular pollutants.* Atmospheric Environment (1967), 1973. **7**(6): p. 603-618.

68. Davidson, M.J., K.R. Mylne, C.D. Jones, J.C. Phillips, R.J. Perkins, J.C.H. Fung, and J.C.R. Hunt, *Plume dispersion through large groups of obstacles—A field investigation.* Atmospheric Environment, 1995. **29**(22): p. 3245-3256.

69. Stathopoulos, T. and R. Storms, *Wind environmental conditions in passages between buildings.* Journal of Wind Engineering and Industrial Aerodynamics, 1986. **24**(1): p. 19-31.

70. Jeong, S.J. and M.J. Andrews, *Application of the k–ε turbulence model to the high Reynolds number skimming flow field of an urban street canyon.* Atmospheric Environment, 2002. **36**(7): p. 1137-1145.

71. Baik, J.-J. and J.-J. Kim, *A Numerical Study of Flow and Pollutant Dispersion Characteristics in Urban Street Canyons.* Journal of applied Meteorology, 1998. **98**.

72.	Kim, J.-J. and J.-J. Baik, *Effects of inflow turbulence intensity on flow and pollutant dispersion in an urban street canyon.* Journal of Wind Engineering and Industrial Aerodynamics, 2003. **91**(3): p. 309-329.

73.	Hunter, L.J., G.T. Johnson, and I.D. Watson, *An investigation of three-dimensional characteristics of flow regimes within the urban canyon.* Atmospheric Environment. Part B. Urban Atmosphere, 1992. **26**(4): p. 425-432.

74.	Johnson, W.B., F.L. Ludwig, W.F. Dabberdt, and R.J. Allen, *An Urban Diffusion Simulation Model For Carbon Monoxide.* Journal of the Air Pollution Control Association, 1973. **23**(6): p. 490-498.

75.	Liu, C.-H. and C.C.C. Wong, *On the pollutant removal, dispersion, and entrainment over two-dimensional idealized street canyons.* Atmospheric Research, 2014. **135-136**: p. 128-142.

76.	Liu, C.-H. and M. C. Barth, *Large-Eddy Simulation of Flow and Scalar Transport in a Modeled Street Canyon.* Vol. 41. 2002. 660-673.

77.	Chu, A.K.M., R.C.W. Kwok, and K.N. Yu, *Study of pollution dispersion in urban areas using Computational Fluid Dynamics (CFD) and Geographic Information System (GIS).* Environmental Modelling & Software, 2005. **20**(3): p. 273-277.

78.	Blocken, B., J. Carmeliet, and T. Stathopoulos, *CFD evaluation of wind speed conditions in passages between parallel buildings—effect of wall-function roughness modifications for the atmospheric boundary layer flow.* Journal of Wind Engineering and Industrial Aerodynamics, 2007. **95**(9): p. 941-962.

79.	Stathopoulos, T., *Design and fabrication of a wind tunnel for building aerodynamics.* Journal of Wind Engineering and Industrial Aerodynamics, 1984. **16**(2–3): p. 361-376.

80.	Chang, C.-H. and R.N. Meroney, *Concentration and flow distributions in urban street canyons: wind tunnel and computational data.* Journal of Wind Engineering and Industrial Aerodynamics, 2003. **91**(9): p. 1141-1154.

81.	Chan, A.T., E.S.P. So, and S.C. Samad, *Strategic guidelines for street canyon geometry to achieve sustainable street air quality.* Atmospheric Environment, 2001. **35**(32): p. 5681-5691.

82.	Galani A., N.P., Venetsanos A., Bartzis J., Neville S., *Prediction and study of pollutant dispersion in a street canyon in London using computational fluid dynamics techniques.* Global NEST Journal, 2009. **Vol 11**(No 4): p. pp 434-439.

83.	Garcia Sagrado, A.P., J. van Beeck, P. Rambaud, and D. Olivari, *Numerical and experimental modelling of pollutant dispersion in a street canyon.* Journal of Wind Engineering and Industrial Aerodynamics, 2002. **90**(4–5): p. 321-339.

84.	Nazridoust, K. and G. Ahmadi, *Airflow and pollutant transport in street canyons.* Journal of Wind Engineering and Industrial Aerodynamics, 2006. **94**(6): p. 491-522.

85.	Ayata, T., *Investigation of building height and roof effect on the air velocity and pressure distribution around the detached houses in Turkey.* Applied Thermal Engineering, 2009. **29**(8–9): p. 1752-1758.

86.   Baik, J.-J., Y.-S. Kang, and J.-J. Kim, *Modeling reactive pollutant dispersion in an urban street canyon.* Atmospheric Environment, 2007. **41**(5): p. 934-949.

87.   Kim, J.-J. and J.-J. Baik, *Urban street-canyon flows with bottom heating.* Atmospheric Environment, 2001. **35**(20): p. 3395-3404.

88.   Hu, L., X. Zhang, W. Zhu, Z. Ning, and F. Tang, *A global relation of fire smoke re-circulation behaviour in urban street canyons.* Journal of Civil Engineering and Management, 2015. **21**(4): p. 459-469.

89.   Zhang, X., L. Hu, F. Tang, and Q. Wang, *Large Eddy Simulation of Fire Smoke Re-circulation in Urban Street Canyons of Different Aspect Ratios.* Procedia Engineering, 2013. **62**: p. 1007-1014.

90.   Hu, L.H., R. Huo, and D. Yang, *Large eddy simulation of fire-induced buoyancy driven plume dispersion in an urban street canyon under perpendicular wind flow.* Journal of Hazardous Materials, 2009. **166**(1): p. 394-406.

91.   Li, X.-X., R.E. Britter, L.K. Norford, T.-Y. Koh, and D. Entekhabi, *Flow and Pollutant Transport in Urban Street Canyons of Different Aspect Ratios with Ground Heating: Large-Eddy Simulation.* Boundary-Layer Meteorology, 2012. **142**(2): p. 289-304.

92.   Pesic, D.J., M.D. Blagojevic, and N.V. Zivkovic, *Simulation of wind-driven dispersion of fire pollutants in a street canyon using FDS.* Environmental Science and Pollution Research, 2014. **21**(2): p. 1270-1284.

93.   Hu, L.H., Y. Xu, W. Zhu, L. Wu, F. Tang, and K.H. Lu, *Large eddy simulation of pollutant gas dispersion with buoyancy ejected from building into an urban street canyon.* Journal of Hazardous Materials, 2011. **192**(3): p. 940-948.

94.   Pesic, D.J., D.N. Zigar, I. Anghel, and S.M. Glisovic, *Large Eddy Simulation of wind flow impact on fire-induced indoor and outdoor air pollution in an idealized street canyon.* Journal of Wind Engineering and Industrial Aerodynamics, 2016. **155**: p. 89-99.

95.   Sudheer, S., L. Kumar, B.S. Manjunath, A. Pasi, G. Meenakshi, and S.V. Prabhu, *Fire safety distances for open pool fires.* Infrared Physics & Technology, 2013. **61**(Supplement C): p. 265-273.

96.   Vasanth, S., S.M. Tauseef, T. Abbasi, and S.A. Abbasi, *Multiple pool fires: Occurrence, simulation, modeling and management.* Journal of Loss Prevention in the Process Industries, 2014. **29**(Supplement C): p. 103-121.

97.   Chatris, J.M., J. Quintela, J. Folch, E. Planas, J. Arnaldos, and J. Casal, *Experimental study of burning rate in hydrocarbon pool fires.* Combustion and Flame, 2001. **126**(1): p. 1373-1383.

98.   Jiang, P. and S.-x. Lu, *Pool Fire Mass Burning Rate and Flame Tilt Angle under Crosswind in Open Space.* Procedia Engineering, 2016. **135**: p. 261-274.

99.   Markatos, N.C., C. Christolis, and C. Argyropoulos, *Mathematical modeling of toxic pollutants dispersion from large tank fires and assessment of acute effects for fire fighters.* International Journal of Heat and Mass Transfer, 2009. **52**(17): p. 4021-4030.

100. Wood, C.R., S.J. Arnold, A.A. Balogun, J.F. Barlow, S.E. Belcher, R.E. Britter, H. Cheng, A. Dobre, J.J.N. Lingard, D. Martin, M.K. Neophytou, F.K. Petersson, A.G. Robins, D.E. Shallcross, R.J. Smalley, J.E. Tate, A.S. Tomlin, and I.R. White, *Dispersion Experiments in Central London: The 2007 DAPPLE project.* Bulletin of the American Meteorological Society, 2009. **90**(7): p. 955-970.
101. Dobre, A., S.J. Arnold, R. Smalley, J.W.D. Boddy, J. Barlow, A. Tomlin, and S.E. Belcher, *Flow field measurements in the proximity of an urban intersection in London, UK.* Vol. 39. 2005. 4647-4657.
102. Jerry Allwine, K. and J. E. Flaherty, *Urban Dispersion Program MSG05 Field Study: Summary of Tracer and Meteorological Measurements.* 2018.
103. García-Sánchez, C., G. Van Tendeloo, and C. Gorlé, *Quantifying inflow uncertainties in RANS simulations of urban pollutant dispersion.* Atmospheric Environment, 2017. **161**: p. 263-273.
104. Markatos, N.C., M.R. Malin, and G. Cox, *Mathematical modelling of buoyancy-induced smoke flow in enclosures.* International Journal of Heat and Mass Transfer, 1982. **25**(1): p. 63-75.
105. Stavrakakis, G.M. and N.C. Markatos, *Simulation of airflow in one- and two-room enclosures containing a fire source.* International Journal of Heat and Mass Transfer, 2009. **52**(11): p. 2690-2703.
106. Ricci, A., M. Burlando, A. Freda, and M.P. Repetto, *Wind tunnel measurements of the urban boundary layer development over a historical district in Italy.* Building and Environment, 2017. **111**: p. 192-206.
107. Coceal, O., E.V. Goulart, S. Branford, T. Glyn Thomas, and S.E. Belcher, *Flow structure and near-field dispersion in arrays of building-like obstacles.* Journal of Wind Engineering and Industrial Aerodynamics, 2014. **125**: p. 52-68.
108. Ramponi, R., B. Blocken, L.B. de Coo, and W.D. Janssen, *CFD simulation of outdoor ventilation of generic urban configurations with different urban densities and equal and unequal street widths.* Building and Environment, 2015. **92**: p. 152-166.
109. Soulhac, L., V. Garbero, P. Salizzoni, P. Mejean, and R.J. Perkins, *Flow and dispersion in street intersections.* Atmospheric Environment, 2009. **43**(18): p. 2981-2996.
110. Hoydysh, W.G. and W.F. Dabberdt, *Concentration fields at urban intersections: fluid modeling studies.* Atmospheric Environment, 1994. **28**(11): p. 1849-1860.
111. Dabberdt, W., W. Hoydysh, M. Schorling, F. Yang, and O. Holynskyj, *Dispersion modeling at urban intersections.* Science of The Total Environment, 1995. **169**(1): p. 93-102.
112. Heath, T., S.G. Smith, and B. Lim, *Tall Buildings and the Urban Skyline:The Effect of Visual Complexity on Preferences.* Environment and Behavior, 2000. **32**(4): p. 541-556.
113. Aristodemou, E., L.M. Boganegra, L. Mottet, D. Pavlidis, A. Constantinou, C. Pain, A. Robins, and H. ApSimon, *How tall buildings affect turbulent air flows and dispersion of pollution within a neighbourhood.* Environmental Pollution, 2018. **233**: p. 782-796.

114. Xing, Y. and P. Brimblecombe, *Dispersion of traffic derived air pollutants into urban parks.* Science of The Total Environment, 2018. **622-623**: p. 576-583.

115. Davidson, M.J., W.H. Snyder, R.E. Lawson Jr, and J.C.R. Hunt, *Wind tunnel simulations of plume dispersion through groups of obstacles.* Atmospheric Environment, 1996. **30**(22): p. 3715-3731.

116. Ahmad Zaki, S., A. Hagishima, and J. Tanimoto, *Experimental study of wind-induced ventilation in urban building of cube arrays with various layouts.* Journal of Wind Engineering and Industrial Aerodynamics, 2012. **103**: p. 31-40.

117. Grimmond, C.S.B. and T.R. Oke, *Aerodynamic Properties of Urban Areas Derived from Analysis of Surface Form.* Journal of Applied Meteorology, 1999. **38**(9): p. 1262-1292.

118. Cheng, H., P. Hayden, A.G. Robins, and I.P. Castro, *Flow over cube arrays of different packing densities.* Journal of Wind Engineering and Industrial Aerodynamics, 2007. **95**(8): p. 715-740.

119. Mavroidis, I. and R.F. Griffiths, *Local characteristics of atmospheric dispersion within building arrays.* Atmospheric Environment, 2001. **35**(16): p. 2941-2954.

120. Shen, Z., B. Wang, G. Cui, and Z. Zhang, *Flow pattern and pollutant dispersion over three dimensional building arrays.* Atmospheric Environment, 2015. **116**: p. 202-215.

121. Vasilopoulos, K., M. Mentzos, I.E. Sarris, and P. Tsoutsanis, *Computational Assessment of the Hazardous Release Dispersion from a Diesel Pool Fire in a Complex Building's Area.* Computation, 2018. **6**(4): p. 65.

122. Antoniadis, A.F., P. Tsoutsanis, and D. Drikakis, *Assessment of high-order finite volume methods on unstructured meshes for RANS solutions of aeronautical configurations.* Computers & Fluids, 2017. **146**: p. 86-104.

123. Rasheed, A.R., D.; Narayanan, C.; Lakehal, D. , *On the effects of complex urban geometries on mesoscale modelling. .* In Proceedings of the 7th International Conference on Urban Climate, Yokohama, Japan, , 2009.

124. Casey, M., T. Wintergerste, T. European Research Community on Flow, and Combustion, *ERCOFTAC Best Practice Guidelines: ERCOFTAC Special Interest Group on "quality and Trust in Industrial CFD".* 2000: ERCOFTAC.

125. Hooff, T. and B. Blocken, *Coupled urban wind flow and indoor natural ventilation modelling on a high-resolution grid: A case study for the Amsterdam ArenA stadium.* Environmental Modelling & Software, 2010. **25**(1): p. 51-65.

126. Gargallo-Peiró, A., A. Folch, and X. Roca, *Representing Urban Geometries for Unstructured Mesh Generation.* Procedia Engineering, 2016. **163**(Supplement C): p. 175-185.

127. Pontiggia, M., G. Landucci, V. Busini, M. Derudi, M. Alba, M. Scaioni, S. Bonvicini, V. Cozzani, and R. Rota, *CFD model simulation of LPG*

dispersion in urban areas. Atmospheric Environment, 2011. **45**(24): p. 3913-3923.

128. Schatzmann, M. and B. Leitl, *Issues with validation of urban flow and dispersion CFD models.* Journal of Wind Engineering and Industrial Aerodynamics, 2011. **99**(4): p. 169-186.

129. Pontiggia, M., M. Derudi, M. Alba, M. Scaioni, and R. Rota, *Hazardous gas releases in urban areas: Assessment of consequences through CFD modelling.* Journal of Hazardous Materials, 2010. **176**(1–3): p. 589-596.

130. Mowrer, F., *Driving Forces for Smoke Movement and Management.* Fire Technology, 2009. **45**: p. 147-162.

131. Węgrzyński, W. and T. Lipecki, *Wind and Fire Coupled Modelling—Part I: Literature Review.* Fire Technology, 2018. **54**(5): p. 1405-1442.

132. Anderson, H.E., *Fire spread and flame shape.* Fire Technology, 1968. **4**(1): p. 51-58.

133. Weise, D. and G. Biging, *Effects of wind velocity and slope on flame properties.* Canadian Journal of Forest Research-revue Canadienne De Recherche Forestiere - CAN J FOREST RES, 1996. **26**: p. 1849-1858.

134. Evans, D., G. Mulholland, D. Gross, H. Baum, and W. Walton, *Burning, smoke production, and smoke dispersion from oil-spill combustion.* 1989.

135. McGrattan, K.B., H.R. Baum, and R.G. Rehm, *Numerical simulation of smoke plumes from large oil fires.* Atmospheric Environment, 1996. **30**(24): p. 4125-4136.

136. Trelles, J., H. Baum, and K. McGrattan, *Smoke Dispersion from Multiple Fire Plumes.* Aiaa Journal - AIAA J, 1999. **37**: p. 1588-1601.

137. Marchant, E.W., *Effect of wind on smoke movement and smoke control systems.* Fire Safety Journal, 1984. **7**(1): p. 55-63.

138. Meroney, R., *Wind effects on atria fires.* Journal of Wind Engineering and Industrial Aerodynamics - J WIND ENG IND AERODYN, 2011. **99**.

139. Poreh, M. and S. Trebukov, *Wind effects on smoke motion in buildings.* Fire Safety Journal, 2000. **35**(3): p. 257-273.

140. Węgrzyński, W. and G. Krajewski, *Influence of wind on natural smoke and heat exhaust system performance in fire conditions.* Journal of Wind Engineering and Industrial Aerodynamics, 2017. **164**: p. 44-53.

141. Li, H., C. Fan, and J. Wang, *Effects of Wind and Adjacent High Rise on Natural Smoke Extraction in an Atrium with Pitched Roof.* APCBEE Procedia, 2014. **9**: p. 296-301.

142. Drysdale, D., *An Introduction to Fire Dynamics.* 2011: Wiley.

143. Kandola, B.S., *Effects of Atmospheric Wind on Flows Through Natural Convection Roof Vents.* Fire Technology, 1990. **Volume 26**(Issue 2): p. pp 106–120.

144. Panindre, P., N.S.S. Mousavi, and S. Kumar, *Positive Pressure Ventilation for fighting wind-driven high-rise fires: Simulation-based analysis and optimization.* Fire Safety Journal, 2017. **87**: p. 57-64.

145. Moosavi, L., N. Mahyuddin, N. Ab Ghafar, and M. Azzam Ismail, *Thermal performance of atria: An overview of natural ventilation effective designs.* Renewable and Sustainable Energy Reviews, 2014. **34**: p. 654-670.

146. Law, M., *A note on smoke plumes from fires in multi-level shopping malls.* Fire Safety Journal, 1986. **10**(3): p. 197-202.

147. Wojciech, W. and K. Grzegorz, *Combined Wind Engineering, Smoke Flow and Evacuation Analysis for a Design of a Natural Smoke and Heat Ventilation System.* Procedia Engineering, 2017. **172**: p. 1243-1251.
148. Fletcher, D.F., J.H. Kent, V.B. Apte, and A.R. Green, *Numerical simulations of smoke movement from a pool fire in a ventilated tunnel.* Fire Safety Journal, 1994. **23**(3): p. 305-325.
149. Wang, H.Y., *Numerical and theoretical evaluations of the propagation of smoke and fire in a full-scale tunnel.* Fire Safety Journal, 2012. **49**: p. 10-21.
150. Gannouni, S. and R. Ben Maad, *Numerical analysis of smoke dispersion against the wind in a tunnel fire.* Journal of Wind Engineering and Industrial Aerodynamics, 2016. **158**: p. 61-68.
151. Lee, Y.-P. and K.-C. Tsai, *Effect of vehicular blockage on critical ventilation velocity and tunnel fire behavior in longitudinally ventilated tunnels.* Fire Safety Journal, 2012. **53**: p. 35–42.
152. Weng, M.-c., X.-l. Lu, F. Liu, and C.-x. Du, *Study on the critical velocity in a sloping tunnel fire under longitudinal ventilation.* Applied Thermal Engineering, 2016. **94**: p. 422-434.
153. Carvel, R. and A. Beard, *The Handbook of Tunnel Fire Safety.* 2005.
154. Caton, S.E., R.S.P. Hakes, D.J. Gorham, A. Zhou, and M.J. Gollner, *Review of Pathways for Building Fire Spread in the Wildland Urban Interface Part I: Exposure Conditions.* Fire Technology, 2017. **53**(2): p. 429-473.
155. Hakes, R.S.P., S.E. Caton, D.J. Gorham, and M.J. Gollner, *A Review of Pathways for Building Fire Spread in the Wildland Urban Interface Part II: Response of Components and Systems and Mitigation Strategies in the United States.* Fire Technology, 2017. **53**(2): p. 475-515.
156. Scaperdas, A., Health, S.E. Staff, C.R. Hebden, G.B. Health, S. Executive, and W.A. Consultants, *Source Term Modelling of Releases Within Building Complexes.* 2003: HSE Books.
157. Dušica Pešić, R.K., Darko Zigar, Valentin Chochev, *The impact of wind inertial and fire buoyancy on air pollution in street canyon.* Working and Living Environmental Protection Vol. 11, No 2, 2014, pp. 65 - 74, Facta Univeritatis.
158. Magnusson, S., A. Dallman, D. Entekhabi, R. Britter, H. Fernando, and L. Norford, *On thermally forced flows in urban street canyons.* Environmental Fluid Mechanics, 2014. **14**: p. 1427-1441.
159. Conceicao, R., M. Melgao, H.G. Silva, K.A. Nicoll, R.G. Harrison, and A.H. Reis, *Transport of the smoke plume from Chiado's fire in Lisbon (Portugal) sensed by atmospheric electric field measurements.* Air Quality, Atmosphere & Health, 2015. **9**: p. 275-283.
160. Vasilopoulos, K., I.E. Sarris, and P. Tsoutsanis, *Assessment of air flow distribution and hazardous release dispersion around a single obstacle using Reynolds-averaged Navier-Stokes equations.* Heliyon, 2019. **5**(4): p. e01482.
161. Vasilopoulos, K., I.E. Sarris, I. Lekakis, and P. Tsoutsanis. *Diesel Pool Fire Incident Inside an Urban Street Canyon.* 2019. Singapore: Springer Singapore.

162. Vos, R. and S. Farokhi, *Introduction to Transonic Aerodynamics*. 2015: Springer Netherlands.

163. Pope, S.B., *Turbulent Flows*. 2000, Cambridge: Cambridge University Press.

164. Kato, M. and B. Launder, *The Modelling of Turbulent Flow Around Stationary and Vibrating Square Cylinders*. Vol. Proceeding 9th Symposium on Turbulent Shear Flows, Kyoto, . 1993.

165. Gorji, S., M. Seddighi, C. Ariyaratne, A.E. Vardy, T. O'Donoghue, D. Pokrajac, and S. He, *A comparative study of turbulence models in a transient channel flow.* Computers & Fluids, 2014. **89**: p. 111-123.

166. Launder, B.E. and D.B. Spalding, *Lectures in mathematical models of turbulence*. 1979: Academic Press.

167. Smagorinsky, J., *General Circulation Experiments with the Primitive Equations: I. The Basic Experiment.* Monthly Weather Review, 1963. **91**(3): p. 99-164.

168. Saathof, P.J., T. Stathopoulos, and M. Dobrescu, *Effects of model scale in estimating pollutant dispersion near buildings.* Journal of Wind Engineering and Industrial Aerodynamics, 1995. **54–55**: p. 549-559.

169. Richards, P.J., R.P. Hoxey, B.D. Connell, and D.P. Lander, *Wind-tunnel modelling of the Silsoe Cube.* Journal of Wind Engineering and Industrial Aerodynamics, 2007. **95**(9): p. 1384-1399.

170. Irwin, H.P.A.H., *The design of spires for wind simulation.* Journal of Wind Engineering and Industrial Aerodynamics, 1981. **7**(3): p. 361-366.

171. Lekakis, I., *Calibration and signal interpretation for single and multiple hot-wire/hot-film probes*. Vol. 7. 1999. 1313.

172. Hoxey, R.P., P. Richards, and J.L. Short, *A 6 m cube in an atmospheric boundary layer flow -Part 1. Full-scale and wind-tunnel results*. Vol. 5. 2002. 165-176.

173. Richards, P.J., R.P. Hoxey, and L.J. Short, *Wind pressures on a 6m cube.* Journal of Wind Engineering and Industrial Aerodynamics, 2001. **89**(14): p. 1553-1564.

174. Hearst, R.J., G. Gomit, and B. Ganapathisubramani, *Effect of turbulence on the wake of a wall-mounted cube.* Journal of Fluid Mechanics, 2016. **804**: p. 513-530.

175. Antoniou, J. and G. Bergeles, *Development of the Reattached Flow Behind Surface-Mounted Two-Dimensional Prisms.* Journal of Fluids Engineering, 1988. **110**(2): p. 127-133.

176. Yakhot, A., H. Liu, and N. Nikitin, *Turbulent flow around a wall-mounted cube: A direct numerical simulation.* International Journal of Heat and Fluid Flow, 2006. **27**(6): p. 994-1009.

177. Hunt, J.C.R.W., A. A.; Moin, P., *Eddies, streams, and convergence zones in turbulent flows.* Center for Turbulence Research Report CTR-S88:pp. 193-208, 1988.

178. Dogan, E., R.E. Hanson, and B. Ganapathisubramani, *Interactions of large-scale free-stream turbulence with turbulent boundary layers.* Journal of Fluid Mechanics, 2016. **802**: p. 79-107.

179. Sattari, P., J.A. Bourgeois, and R.J. Martinuzzi, *On the vortex dynamics in the wake of a finite surface-mounted square cylinder.* Experiments in Fluids, 2012. **52**(5): p. 1149-1167.
180. Schlatter, P., J. Malm, C. Mavriplis, and D.S. Henningson, *Direct numerical simulation of the flow around a wall-mounted square cylinder under various inflow conditions AU - Vinuesa, Ricardo.* Journal of Turbulence, 2015. **16**(6): p. 555-587.
181. Pancholy, P., K. Clemens, P. Geoghegan, M. Jermy, M. Moyers-Gonzalez, and P. Wilson, *Numerical Study of Flow and Pedestrian Level Wind Comfort Inside Uniform and Non-Uniform Street Canyons with Different Street Width to Building Height Aspect Ratios.* 2017.
182. Lombardi, D.J. and J.E. Cermak, *A Wind Tunnel Study of Gaseous Pollutants in City Street Canyons AU - Wedding, James B.* Journal of the Air Pollution Control Association, 1977. **27**(6): p. 557-566.
183. Gough, H., *Effects of meteorological conditions on building natural ventilation in idealised urban settings. PhD thesis, University of Reading. .* 2017.
184. Yu, K.T. and X. Yuan, *Introduction to Computational Mass Transfer: With Applications to Chemical Engineering.* 2016: Springer Singapore.
185. Golden, J., *Scale model techniques. M.S. thesis.* New York University, College of Engineering, 1961: p. 50.
186. Peterson, E.W. and J.P.H. Jr., *On the Use of Power Laws for Estimates of Wind Power Potential.* Journal of Applied Meteorology, 1978. **17**(3): p. 390-394.
187. Launder, B.E. and D.B. Spalding, *The numerical computation of turbulent flows.* Computer Methods in Applied Mechanics and Engineering, 1974. **3**(2): p. 269-289.
188. Oikawa, S. and Y. Meng, *A field study of diffusion around a model cube in a suburban area.* Boundary-Layer Meteorology, 1997. **84**(3): p. 399-410.
189. Theodorsen, T. *Mechanism of turbulence.* in *Proc. 2nd Midwestern Conference on Fluid Mechanics.* 1952.
190. Huber, A.H., *Determine Good Engineering Practice Stack Height, EPA 450/4-81-O03.* 1981.
191. Huber, A.H. and W.H. Snyder, *Wind tunnel investigation of the effects of a rectangular-shaped building on dispersion of effluents from short adjacent stacks.* Atmospheric Environment (1967), 1982. **16**(12): p. 2837-2848.
192. Gousseau, P., B. Blocken, and G.J.F. van Heijst, *CFD simulation of pollutant dispersion around isolated buildings: On the role of convective and turbulent mass fluxes in the prediction accuracy.* Journal of Hazardous Materials, 2011. **194**: p. 422-434.
193. Hoffmann, N. and N.C. Markatos, *Thermal radiation effects on fires in enclosures.* Applied Mathematical Modelling, 1988. **12**(2): p. 129-140.
194. Richards, P.J. and R.P. Hoxey, *Appropriate boundary conditions for computational wind engineering models using the k-ε turbulence model.* Journal of Wind Engineering and Industrial Aerodynamics, 1993. **46-47**(Supplement C): p. 145-153.

195. Richards, P.J. and S.E. Norris, *Appropriate boundary conditions for computational wind engineering models revisited.* Journal of Wind Engineering and Industrial Aerodynamics, 2011. **99**(4): p. 257-266.
196. Richards, P., A. Quinn, and S. Parker, *A 6 m cube in an atmospheric boundary layer flow -Part 2. Computational solutions.* Vol. 5. 2002. 177-192.
197. Franke, J., A. Hellsten, H. Schlünzen, and B.E. Carissimo, *Best practice guideline for the CFD simulation of flows in the urban environmentt.* COST Action 732, 2007.
198. Babrauskas, V., *Estimating large pool fire burning rates.* Fire Technology, 1983. **19**(4): p. 251-261.
199. Evans, D.D., G.W. Mulholland, H.R. Baum, W.D. Walton, and K.B. McGrattan, *In Situ Burning of Oil Spills.* Journal of Research of the National Institute of Standards and Technology, 2001. **106**(1): p. 231-278.
200. Walton, W.D., W.H. Twilley, A.D. Putorti, and R.R. Hiltabrand, *Smoke measurements using an advanced helicopter transported sampling package with radio telemetry.* In: Proceedings of the 18th Arctic and Marine Oilspill Program Technical Seminar. Environment Canada, Ottawa, Ontario, 1995: p. 1053-1074.
201. Stout, S. and Z. Wang, *Oil Spill Environmental Forensics Case Studies.* 2017: Elsevier Science.
202. Richards, P.J., R.P. Hoxey, and J.L. Short, *Spectral models for the neutral atmospheric surface layer.* Journal of Wind Engineering and Industrial Aerodynamics, 2000. **87**(2): p. 167-185.
203. Stathopoulos, T. and C.C. Baniotopoulos, *Wind Effects on Buildings and Design of Wind-Sensitive Structures.* 2007: Springer Vienna.
204. Roache, P.J., *Quantification of uncertainty in Computational Fluid Dynamics.* Annual Review of Fluid Mechanics, 1997. **29**(1): p. 123-160.
205. Chatzimichailidis, A.E., C.D. Argyropoulos, M.J. Assael, and K.E. Kakosimos, *Qualitative and Quantitative Investigation of Multiple Large Eddy Simulation Aspects for Pollutant Dispersion in Street Canyons Using OpenFOAM.* Atmosphere, 2019. **10**(1): p. 17.
206. Brzoska, M.A., D. Stock, and B. Lamb, *Determination of plume capture by the building wake.* Journal of Wind Engineering and Industrial Aerodynamics, 1997. **67-68**: p. 909-922.
207. Assael, M.J. and K.E. Kakosimos, *Fires, Explosions, and Toxic Gas Dispersions: Effects Calculation and Risk Analysis.* 2010: CRC Press.
208. Eppler, M., M. Aeschimann, M. Aeschimann@mindarea, and Ch, *A systematic framework for risk visualization in risk management and communication.* Risk Management, 2009. **11**.
209. Horwitz, R. and R. Koss, *Hedge Fund Risk Fundamentals: Solving the Risk Management and Transparency Challenge.* 2007: Wiley.
210. Carpignano, A., E. Golia, C. Di Mauro, S. Bouchon, and J.P. Nordvik, *A methodological approach for the definition of multi-risk maps at regional level: first application.* Journal of Risk Research, 2009. **12**(3-4): p. 513-534.

211. Roth, F., *Visualizing Risk: The Use of Graphical Elements in Risk Analysis and Communications.* CSS Risk and Resilience Reports, 2012.
212. Gai, C., W. Weng, and H. Yuan, *GIS-Based Forest Fire Risk Assessment and Mapping*. 2011. 1240-1244.
213. Chuvieco, E. and J. Salas, *Mapping the spatial distribution of forest fire danger using GIS.* International Journal of Geographical Information Systems, 1996. **10**(3): p. 333-345.
214. Dong, X., D. Li-min, S. Guo-fan, T. Lei, and W. Hui, *Forest fire risk zone mapping from satellite images and GIS for Baihe Forestry Bureau, Jilin, China.* Journal of Forestry Research, 2005. **16**(3): p. 169-174.
215. Abedi Gheshlaghi, H., *Using GIS to Develop a Model for Forest Fire Risk Mapping.* Journal of the Indian Society of Remote Sensing, 2019. **47**(7): p. 1173-1185.
216. Kavzoglu, T., E. Sahin, and I. Colkesen, *Landslide susceptibility mapping using GIS-based multi-criteria decision analysis, support vector machines, and logistic regression.* Landslides, 2013. **11**.
217. Berkowicz, R., O. Hertel, S. Larsen, N. Sørensen, and M. Nielsen, *Modelling traffic pollution in streets.* 1997.
218. Akubue, J., *Effects of Street Geometry on Airflow Regimes for Natural Ventilation in Three Different Street Configurations in Enugu City*. 2019.
219. Vasanth, S., S.M. Tauseef, T. Abbasi, and S.A. Abbasi, *Assessment of four turbulence models in simulation of large-scale pool fires in the presence of wind using computational fluid dynamics (CFD).* Journal of Loss Prevention in the Process Industries, 2013. **26**(6): p. 1071-1084.
220. Grigoriadis, D.G.E., I.E. Sarris, and S.C. Kassinos, *MHD flow past a circular cylinder using the immersed boundary method.* Computers & Fluids, 2010. **39**(2): p. 345-358.
221. McGrattan, K., H. Baum, R. Rehm, A. Hamins, G. Forney, J. Floyd, S. Hostikka, and K. Prasad, *Fire Dynamics Simulator (Version 5) Technical Reference Guide*. Vol. 1018. 2010.
222. Witri Muhammad Yazid, A., N.A. Che Sidik, S.M. Salim, and K. Saqr, *A review on the flow structure and pollutant dispersion in urban street canyons for urban planning strategies*. Vol. 90. 2014.
223. Soulhac, L., R.J. Perkins, and P. Salizzoni, *Flow in a Street Canyon for any External Wind Direction.* Boundary-Layer Meteorology, 2008. **126**(3): p. 365-388.
224. Pesic, D.J., M.D. Blagojevic, and S.M. Glisovic, *The model of air pollution generated by fire chemical accident in an urban street canyon.* Transportation Research Part D: Transport and Environment, 2011. **16**(4): p. 321-326.
225. King, M.-F., H.L. Gough, C. Halios, J.F. Barlow, A. Robertson, R. Hoxey, and C.J. Noakes, *Investigating the influence of neighbouring structures on natural ventilation potential of a full-scale cubical building using time-dependent CFD.* Journal of Wind Engineering and Industrial Aerodynamics, 2017. **169**: p. 265-279.
226. Gough, H., T. Sato, C. Halios, C.S.B. Grimmond, Z. Luo, J.F. Barlow, A. Robertson, R. Hoxey, and A. Quinn, *Effects of variability of local winds on cross ventilation for a simplified building within a full-scale asymmetric*

array: Overview of the Silsoe field campaign. Journal of Wind Engineering and Industrial Aerodynamics, 2018. **175**: p. 408-418.

Appendix A Wind tunnel experiments

A.1 Appendix Spires

In order to achieve an atmospheric boundary layer spires are used at the entrance of the wind tunnel's test section. A simple formula which is defined by Irwin [170] is used for the design of these spires. The shape of the spire is indicated in Figure_Apx 1- 1.

The mean velocity and the turbulence properties are defined after the spire position. The velocity inlet is described with a power law equation:

$$\frac{U(z)}{U_{ref}} = \left(\frac{z}{z_{ref}}\right)^{a}$$ **(Apx1-1)**

$U(z)$ is the mean velocity at elevation z, U_{ref} is the reference velocity at a reference height z_{ref}, and α = 0.1 is the power law exponential.
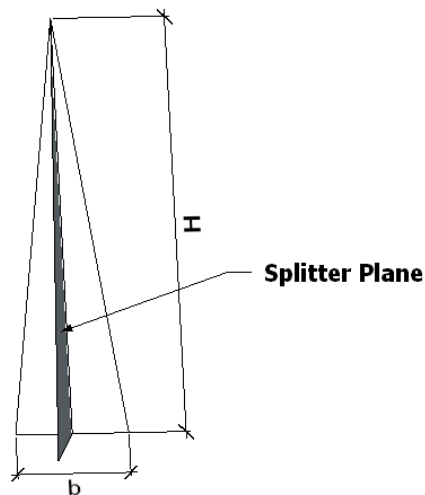
Figure_Apx 1- 1The spire's geometry.

After the definition of the atmospheric boundary layer δ and the power law α the height of the spire is defined as:

$$H = \frac{1.39\,\delta}{1 + \frac{\alpha}{2}}$$

(Apx1-2)

The base to height ratio is b/H is defined as

$$b/h = 0.5\left[0.5\psi\left(\frac{h}{\delta}\right)(1 + \psi)\right](1 + \frac{\alpha}{2})$$

(Apx1-3)

where

$$\psi = \beta\left(\left[\frac{2}{1 + 2\alpha}\right] + \beta - \left[1.13\alpha/(1 + \alpha)(1 + \frac{\alpha}{2})\right]\right)/(1 - \beta)^2$$

(Apx1-4)

and

$$\beta = \left(\frac{\delta}{h}\right)\alpha/(1 + \alpha)$$

(Apx1-5)

where h is the h of the building.

The distance between the central line of the spires is set as H/2. The base of the splitter plate is set as H/4.

A.2 Anemometer Calibration

The anemometer is calibrated with a pitot-static tube and the free-stream flow inside the wind tunnel. The calibration establishes an equation between the flow velocity and the output voltage. A fitting curve is defined by the measured volts and the mean velocity. A 4th order polynomial curve is defining the fitting curve. The polynomial coefficients are defined with the least-squares method sense.

The calibration was performed with the probe axis parallel to the flow direction. The effective cooling velocity is defined as:

$$Q = U_o\sqrt{cos^2\beta + k_b^2 sin^2\beta}$$

(Apx2-1)

In order to define the two velocity components from the X-wire signals the approach of Lekakis [171] is used. The effective cooling velocity for sensor 1 and 2 are defined as:

$$Q_1^2 = |V|^2 \left[cos^2(\psi_p - a_1) + k_1^2 sin^2(\psi_p - a_1) \right] \qquad \text{(Apx2-2)}$$

$$= |V|^2 \left[b_{11} cos^2 \psi_p + 2\, b_{21}\, cos\psi_p\, sin\, \psi_p + b_{31} sin^2 \psi_p \right]$$

$$Q_2^2 = |V|^2 \left[cos^2(a_2 - \psi_p) + k_2^2 sin^2(a_2 - \psi_p) \right] \qquad \text{(Apx2-3)}$$

$$= |V|^2 \left[b_{12} cos^2 \psi_p + 2\, b_{22}\, cos\psi_p\, sin\, \psi_p + b_{32} sin^2 \psi_p \right]$$

As shown in Figure_Apx 2-1 the Equations are solved for the velocity magnitude in the (x_p, y_p) and the angle ψ_p and the coefficient b are defined as:

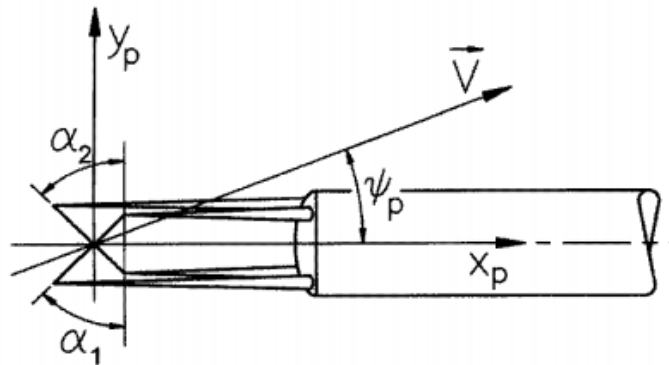$$b_{1i} = cos^2 a_i + k^2 sin^2 a_i \qquad \text{(Apx2-4)}$$

$$b_{2i} = 0.5(1 - k^2)\, sin 2a_i \qquad \text{(Apx2-5)}$$

$$b_{3i} = sin^2 a_i + k^2 cos^2 a_i \qquad \text{(Apx2-6)}$$

Where i=1, 2.With the definition of the ratio Q=$\left(\dfrac{Q_2}{Q_1}\right)^2$ the equations are limited to:

$$T_3 tan^2 \psi_p + 2T_2 tan\psi_p + T_1 = 0 \qquad \text{(Apx2-7)}$$

$$T_j = b_{j2} - A b_{j1}, j = 1,2,3 \qquad \text{(Apx2-8)}$$

Figure_Apx 2-1 X-probe plane definition [171]